UNIVERSITÀ degli STUDI di CATANIA | DIPARTIMENTO di FISICA e ASTRONOMIA

DOCTOR OF PHILOSOPHY IN PHYSICS
XXXI CYCLE

Giada Petringa

STUDY ON EFFICACY IMPROVEMENTS AND QUALITY OF THE PROTONTHERAPY TREATMENTS

PhD Thesis

Tutor:
Prof. S. Romano
Supervisors:
Dott. G.A.P. Cirrone
Dott. G. Cuttone

A.A. 2018/2019

Contents

Introduction

The urgent need for radical radiotherapy research to achieve improved tumour control in the context of reducing the risk of normal tissue toxicity and late-occurring sequelae, has driven in recent decades the fast-growing development of cancer treatment by accelerated beams of charged particles (hadrontherapy). This appears to be particularly true for protontherapy, which has emerged as the most-rapidly expanding hadrontherapy approach, totalling over 170,000 patients treated thus far worldwide. The primary motivation for investigation into this area was based on the physical properties of charged particles, which can deposit energy far more selectively than photons: thanks to the inverted depth-dose profile described by the Bragg curve.

However, one of the shortcomings of proton therapy resides in its limited capability to locally control radioresistant cancers. Heavier particles such as ^{12}C ions can overcome such radioresistance because they are densely ionizing. On the other hand, complications related to nuclear fragmentation from the primary beam, along with a still partial understanding of the consequences of the exposure of normal cells to high-LET radiation, and also considering the complexity and high costs associated with a ^{12}C treatment facility, fuelled research into exploring novel strategies with the aim to achieve alternative solutions for a localized increase of proton damage efficiency (RBE).

The research in protontherapy is being configured today a new era

where new objectives in term of quality treatment improvement are reached and new methodologies to increase the radiobiological effect are investigated. This thesis includes both these aspects. The first part of the work is dedicated to a new proposed approach based on a nuclear reaction triggered by clinical protons. I report the first experimental proof of the idea theoretically proposed by Do-Kun Y. et al. in [158], based on the use of the $p +^{11} B \rightarrow 3\alpha$ nuclear fusion reaction to enhance proton biological effectiveness exclusively in the tumour region through the generation of short-range high-LET alpha particles, thus being of potential clinical worth. The main results of this experiment are reported in Chapter 2. The remarkable observed effect has pushed on to starting a critical analytical study to reproduce the biological effect. I performed a set of analytical calculations as well as Monte Carlo simulations (Section 2.4) to reach this scope. Aroused particular interest also the study of prompt gammas emitted by the interaction of incident protons with boron target. This is a powerful technique to quantifying the absorbed boron by a tumor and monitoring online the treatments bringing out the RBE map on the treated region (Section 2.5). The work in this field has been presented in [116] [110] [112] [113] [122] leading different publications [39] [120] [119]. I won the Young Investigator Award of the European Radiation Research Society (ERRS) for the interesting studies on protontherapy enhancement field. The results reached on PBCT lead to a new INFN funded project called NEPTUNE (Nuclear process-driven Enhancement of Proton Therapy UNravEled). The main intent of this new project will be to consolidated and explain the promising results on PBCT and investigate a new reaction $p +^{19} F \rightarrow \alpha +^{16} O$, which also generates secondary particles potentially able to lead a local enhancement of proton effectiveness. During its three years the NEPTUNE project will study different aspects of these researches: from modelling (using analytical and Monte

Carlo approaches), to microdosimetry and radiobiology.
As abovementioned another important item in the protontherapy research consist of investigations about the improvements in the treatments quality. In this thesis, Monte Carlo approach has been evaluated as a new promising strategy for the calculation of the main parameters of interest in medical physics and radiobiological applications. A systematic study to identify the best algorithm for the Linear Energy Transfer (LET) calculation has been performed (Chapter 5). This resulted in a new proposed algorithm and its application for the radiobiological effect estimation (Chapter 6). The LET is, in fact, the main physical quantity that describe the radiation quality and the mechanism of released energy by ionizing particles. This is of particular importance for the prediction of radiobiological effects as a function of the radiation used in clinical environment. The work done has also included a new method for the Relative Biological Effectiveness (RBE) estimation (Chapter 6). The main results are reported in [123] [121] [115] [117].
A work on the proton therapy improvement cannot neglect a precise beam characterization as well as the optimisation of its transport parameters. Accordingly, a specific task included in this thesis was focused on the improvement of the INFN (Istituto Nazionale di Fisica Nucleare) multidisciplinary facilities: LNS (Laboratori Nazionali del Sud) and TIFPA (Trento Institute for Fundamentals Physics Applications). The main intent has been to increase the beam quality and the techniques for its monitoring. For these reasons the Monte Carlo simulations of the three beamline of interest have been optimized: CATANA (INFN-LNS); Zero Degree Experimental room (INFN-LNS) and the Multidisciplinary beamline of the TIFPA-INFN. Systematics studies to realize a scattering system for high energy proton and light ions beams (^{12}C, ^{4}He, ^{16}O) as a well as a passive system for the beam energy modu-

lation (Chapter 4) have been performed. In the end, a new detector for the online dose profiler acquisition has been developed and characterized for its future installation in the abovementioned facilities (Chapter 7). The work carried out on the beam quality improvement has been realized in strictly connection with the MOVE-IT (MOdelling and Verification for Ion beam Treatment planning), INFN project. The main aim of Move-it (2017-2019) was, in fact, to achieve a synergy among different expertise (i.e. detectors development, algorithms to optimize the treatment planning systems, radiobiological experience with in-vivo and in-vitro experiments) to further refine and optimize the current treatment planning systems for proton beams. These studies have resulted in [114] [111] [146] [26].

Chapter 1

Protontherapy: state of the art

1.1 The advent of protons in cancer therapy

Cancer therapy is a multi-modality approach including surgery, chemotherapy, radiotherapy and immunotherapy. Conventional radiotherapy is typically administered using external energetic photon (5-20 MeV) or electron beams. The first medical application of ionizing radiation, using x-rays, occurred in 1895 [128] [127]. In the following decades, radiation therapy became one of the main treatment options in oncology [58] [79]. Over the past years, in fact, many improvements have been made in order to optimize the treatments. Technical advances have been aimed mainly to reduce the dose to the healthy tissue while maintaining prescribed doses to the tumor target [93] [90]. Computerized treatment planning and advanced imaging techniques have influenced the beam delivery precision [125] [84]. The advantages of proton radiation therapy, compared with conventional photon radiation therapy, were outlined for the first time by Wilson in 1964 [153]. He proposed the idea of utilizing the finite range of the Bragg peak of proton beams for treating targets deep within healthy tissue and was the first that describe the potential of proton beams for medical purposes. Nowadays, proton therapy represents an established alternative to photon radio-

therapy for the treatment of specific types of cancer. According to the latest updates of the Particle Therapy Co-Operative Group (PTCOG) [61], more than 80 hadrontherapy centers are currently in operation and this number is going to increase in the next years, as reported in Figure 1.1.

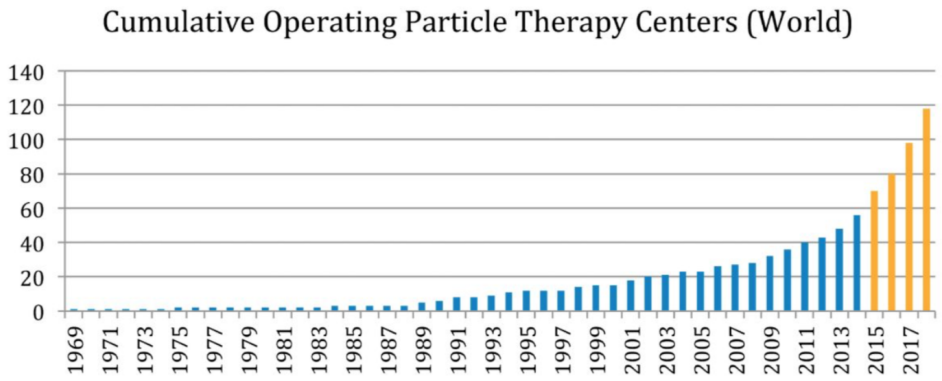

Figure 1.1: Number of worldwide hadron therapy centers as a function of the years. Last four years trend in yellow

Besides the advantages offered by the peculiar inverted depth-dose profile, protons also show an enhanced biological effectiveness in cell killing. This is related to the increased *Linear Energy Transfer* (LET) compared to X-rays when protons are close to the Bragg peak [46]. High-LET value are associated with a localized energy deposition resulting in the induction of enhanced, unrepairable biological damage. Consequently, charged particles are often defined as densely ionizing radiation, in contrast to photons being considered sparsely ionizing radiation.

1.1.1 The rationale for using protons in radiotherapy

Since the beginning of clinical radiation therapy, one of the main goal of radiotherapy was to restrict the irradiated volume to the site and shape of the target volume [40] [45]. The strongest argument to consider protons for radiation therapy is the fact that, thanks to their sharp dose profile, entering in the matter (Bragg Peak),they are suited to irradiate a tumor at any depth of the body with a minimum dose to the surrounding healthy tissues.

1.2 Physical Properties

Photons of short wavelengths (X- or γ rays) interact to the medium througth stochastic events, such as inelastic or Compton scattering, photoelectric processes and pair production [133]. Due to the statistical nature of these absorption processes as well as the strong deflection during the interactions with medium atoms, a photon beam reveals an initial build-up, followed by a region of exponentially decreasing dose (see Figure 1.2).

In classical mechanics, the transfer of kinetic energy is inversely proportional to the square of the velocity ($dE/dx \sim 1/\nu^2$). Due to their low mass, accelerated electrons reach rapidly high velocities close to the speed of light (at energies > 1 MeV). As the electron velocity approaches the speed of light c, the energy loss per unit length become independent of the energy ($dE/dx \sim 1/c^2$). As a consequence, relativistic electrons deposit a constant energy dose per unit length. In water with its density similar to tissue, this dose corresponds to approx 2 MeV/cm [91]. The low mass renders electrons subject to strong lateral scattering. Bremsstrahlung photons which are produced by stopping process of the electrons in the target nuclei, cause the low intensity tail

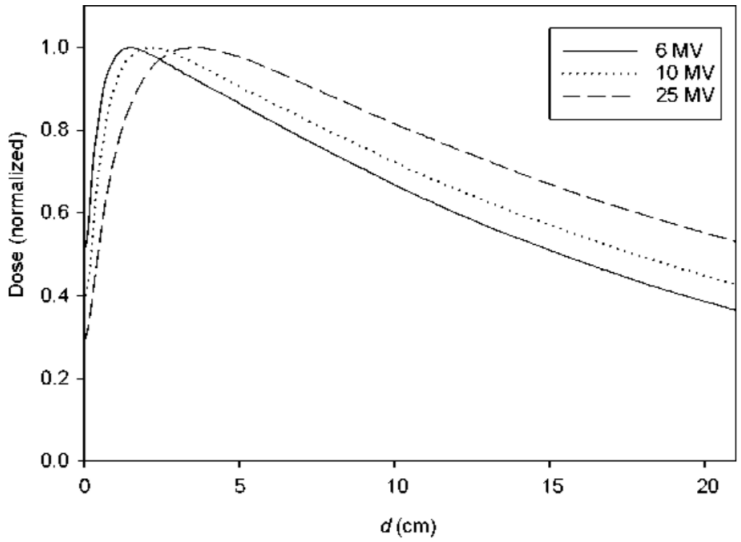

Figure 1.2: Depth dose distributions of incident photons in water with different energy

at the end of the depth-dose curve. For protons and all heavier ions, the absorption curve in matter shows a slow initial increase with penetration depth and a rise and fall towards the end of the particle's range [75]. Because of their much higher mass ions the lateral scattering is significantly less than electrons, as shown in Figure 1.3

Accelerated atomic nuclei of the therapeutically relevant kinetic energy interact predominantly via Coulomb forces with the target electrons of the traversed matter. This leads to excitation and ionization of atoms along the track of the travelling particle. Quantitatively, the energy loss per unit path length, also called *Stopping Power* is described by the Beth formula [18] [21]:

$$\frac{dE}{dx} \sim K n_0 (Z_{eff})^2 / \beta^2 [ln((2m_e c^2 \beta^2 / I(1-\beta^2)) - \beta)] \qquad (1.1)$$

where K is a constant n_0 the electron density of the target material, Z_{eff} the effective charge of the projectile ions, β the velocity of the

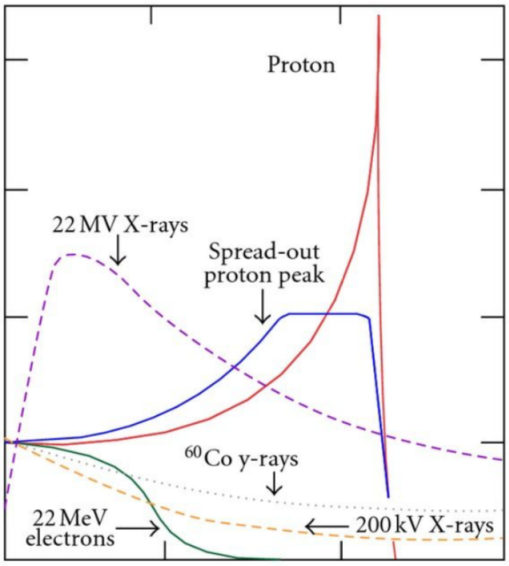

Figure 1.3: Bragg peak and Spread-Out Bragg Peak (SOBP) for a proton beam in comparison with photon and electron dose distributions

projectile in units of speed of light ($\beta = \nu/c$). I the mean ionization energy of the target atoms, and m_e the rest mass of the electron. For low particle velocity ($\nu << c$ and $\beta << 1$) the Bethe formula can be reduced to:

$$\frac{dE}{dx} \sim K n_0 (Z_{eff})^2/\nu^2 [ln((2m_e c^2/I)] \tag{1.2}$$

Under these conditions, the stopping power varies mainly with Z_{eff}^2/ν^2. With decreasing speed, dE/dx should increase. Most ion particles travel the same distance in a monoenergetic beam. But not all are involved in the same number of collisions. Their range is, therefore, somewhat different. This phenomenon is called straggling. In tissues, the difference is of the order of 1% of the mean range for protons [59]. For heavier ions, range straggling varies approximately inversely to the square-root of the particle mass. The transverse spread of an infinitely narrow

proton beam amounts to approximately 5% of its initial range. Just as for range straggling, the angular deflection from the incident beam direction by multiple scattering decrease with increasing charge and mass.

1.3 Biophysical Propertie

1.3.1 Stopping Power and Linear Energy Transfer

The linear energy transfer or LET is a measure for the energy deposited by an ionizing particle travelling through matter [159]. It's close to the stopping power concept but with some conceptual discrepancies: while the stopping power can be seen as a material property (depending on electron density) describing the energy absorbed by matter, LET expresses the loss of particle energy [83]. If all secondary electron energies are considered, LET, numerically is equal to the Stopping Power. The LET, generally expressed in keV/μm is the major parameter to discern qualitatively the biological effect of different kinds of radiations. The LET is widely used to characterized ion-induced damage even if has been shown that is not a good parameter to describe the full spectrum of biological radiation effects. The limitations of LET become particularly evident when ions of different atomic number are compared. In particular for LET values greater than 100 keV/μm, different biological responses can be observed for particles with the same LET, as shown in Figure 1.4.

This is due to the different mechanisms of energy depositions. Ions of the same velocity produce tracks of secondary electrons with the same kinetic energy but the dose density within the track, i.e. the number of secondary electrons produced, is different [82]. Today the LET is one of the most studied parameters in the field of hadrontherapy. It's strictly linked to the biological damage and some aspects of the

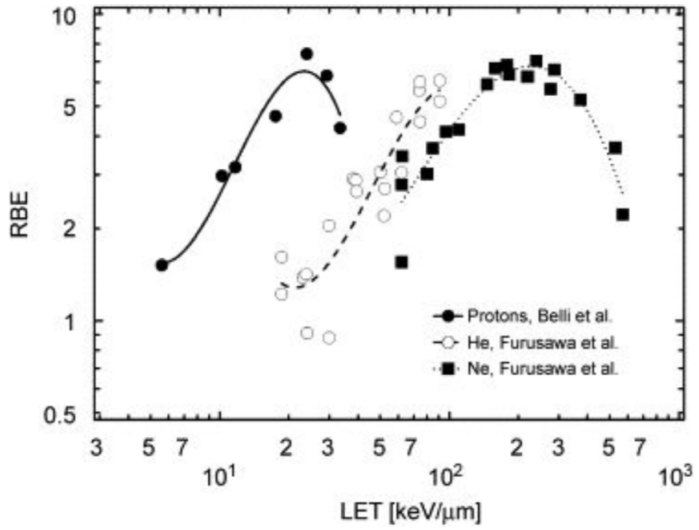

Figure 1.4: Relative Biological effectiveness (RBE) of ion beams as a function of Linear Energy Transfer (LET) with the same cell line.

energy deposition in a real mixed radiation field are investigated by using micro/nano dosimeter detectors and new algorithms. All of these aspects will be discussed in detail in the Chapter 5.

1.3.2 Relative Biological Effectiveness

Prior to the clinical use of accelerated ions, their biological effects were studied in several experimental test. In the 1950s, the Uppsala cyclotron was intensively used to study such biological effects [89]. The main aim of these experiments was to determine the ion biological effectiveness in comparison to the effect of a reference radiation (mostly 250 kV x-rays), i.e. the so-called Relative Biological Effectiveness (or RBE) [5]. Early studies revealed an RBE close to one for protons meaning that the proton dose required to produce a given effect was comparable to the equivalent dose from photons. More refined studies however, indicated that low-energy ($<$ 1MeV) and very high-energy ($>$1 GeV)

protons can reach an RBE-value of 2 or more, depending on radiobiological endpoint studied. An elevated biological effectiveness in the Bragg peak region has clearly been demonstrated for ions heavier than helium [60].

1.4 Clinical implication

Today proton therapy is a well-established treatment option for many tumor types and sites. Advantages when using protons in favour of photons have been shown in terms of Tumor Control Probability (TCP) and/or Normal Tissue Complication Probability (NTCP). Various dosimetric studies clearly demonstrate superior normal tissue sparing with protons. It is well recognized that protons are extremely valuable to treat tumors close to critical structures [140] [77]. In the pediatric patient population, the impact of the decreased total absorbed energy in the patient with protons is most significant. One example is the treatment of medulloblastoma, a malignant tumor in the medulla and that extends in the cerebellum [77] [28] [151]. Treatment with photon radiation therapy invariably causes a significant dose to heart, lung and abdominal tissue as well as the organ at risk in the cranium, something that can be largely avoided using protons as shown in the Figure 1.5.

These facts have boosted proton therapy in particular for pediatric patients. Although the dose distributions achievable with protons are superior to those achievable with photons, it is debatable whether the advantages of proton therapy are clinically significant for all treatment sites. Nowadays there is an ongoing discussion about the clinical trials that show a significant advantage in outcome by using protons.

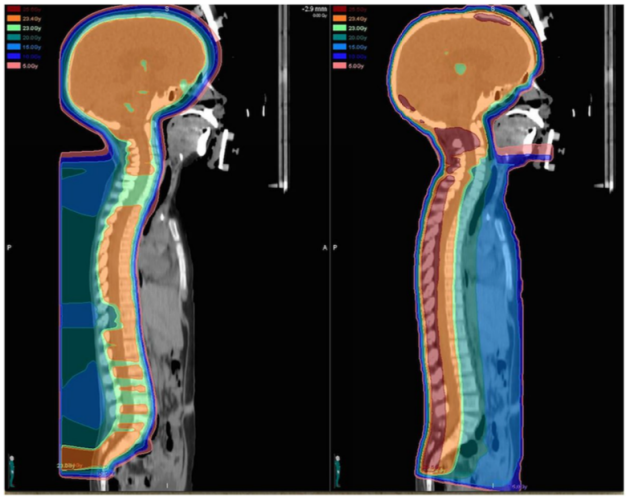

Figure 1.5: Dose distributions for a proton (left) and photon (right) craniospinal plan prescribed to 23.4 Gy (relative biological equivalents) are illustrated for comparison. The proton craniospinal plan provides considerable sparing of normal tissues anterior to the spinal canal and delivers a significantly reduced total integral dose to the patient. Number of worldwide hadron therapy centers as a function of the years. In yellow is reported the trend registered in the last four years

1.5 New Ions for radiotherapy treatments

Protons are the charged particles most largely used in clinical practice and for which the largest clinical experience has been acquired. Remarkably, this is somehow in contrast with the improved physical properties offered by heavier ions [142]. This contradiction is due to the fact that the biological effectiveness of other ions is still affected by large uncertainties, which do not fulfil clinical constraints [144]. An intense discussion has once again arisen in the literature in recent years concerning the possibility of optimizing the clinical potential of charged particle therapy by extending the spectrum of therapeutic ions beyond protons and carbon ions [138] [85]. Currently, innovative treatment-planning

allowing a simultaneous optimization of different particle beams are investigated as well as new techniques to characterize the ion beams from the point of view of the physical and biological characteristics with a level of accuracy high enough to allow their clinical use [138]. Up to now, many studies were directed to improve the description of helium and oxygen beams for clinical use on the basis of experimental data and transport code (Monte Carlo and analytical). As well-known, the strong advantage offered by the physics of charged particles is the increasing LET in the Bragg peak, which allows high RBE to be obtained corresponding to the tumor. However, the LET variation along the depth-dose profile of different ions deserves an accurate discussion. It has been shown that the portion of the depth-dose curve where high-LET is released is strongly influenced by the particle type. From this point of view, while light particles like proton and Helium produce high-LET only on the distal part of the Bragg curve, in the case of carbon ions the high-LET region and therefore in healthy tissues, as shown in Figure 1.6. Thus, intermediate ions from lithium to beryllium might represent a valid compromise [144].

The very high LET radiations are interesting for its effectiveness in killing hypoxic cells that are normally radioresistant. The Oxygen Enhancement Ratio (OER), defined as the ratio of doses under hypoxia to normoxic conditions needed to obtain the same biological effect, becomes close to one only at LET values that are accessible for ions heavier than carbon [73] [126]. From this point of view, Oxygen and Neon ions might be a promising tool. However, due to their increased charge, such heavy ions release a comparably high LET along the peak, thus increasing the risk of normal tissue damage. This statement has suggested to combining light and heavy ion modalities inside a treatment plan, i.e. by forwarding high-LET ^{16}O ions only to the hypoxic parts of the target, while covering the rest with lighter particles (p, ^{4}He). In

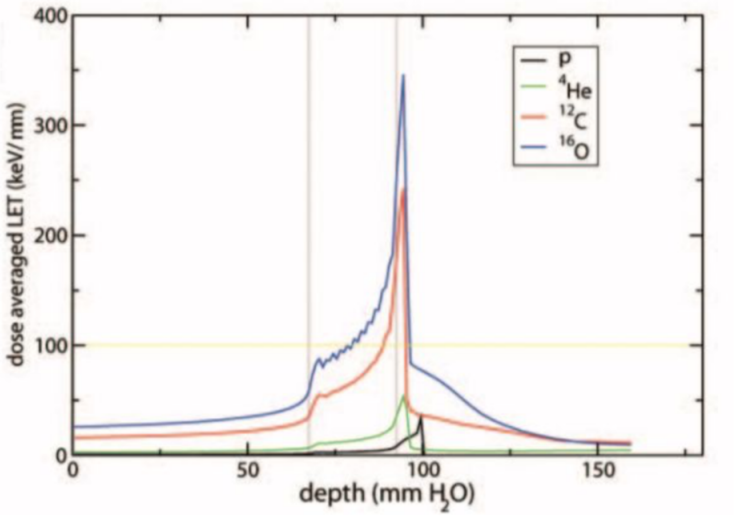

Figure 1.6: Profiles of dose-averaged linear energy transfer for the irradiation of an extended target of 2.5 X 2.5 X 2.5 cm^3 centered at 8 cm depth in water, with a field optimized on a uniform physical dose (2Gy) [144]

the current version of GSI (Helmholtz Centre for Heavy Ion Research) in-house treatment planning system TRiP98 (TReatment planning for Particles, 1998 edition) the possibility to activate several ion modalities inside a single plan has been recently inserted [1] [84]. Figure 1.7 represents the first tests of plans optimized for a uniform target survival level of 10%. In that case, three cases were analysed: single-ion optimizations with opposite ^4He or ^{16}O fields, and quadruple-field optimization with two pairs of opposite fields (^{16}O + ^{16}O and ^4He + ^4He) [138].

There are ongoing studies of ^{16}O beams, investigating also the radiobiological properties of ions, but the complete description of the beam still needs dedicated research, accounting for all the different effects [144]. This is the reason because there was a particular emphasis in new methodologies to optimize the uniformity of ions beam (especially ^{16}O and ^4He) on this thesis work. In particular, in Chapter 4 reports

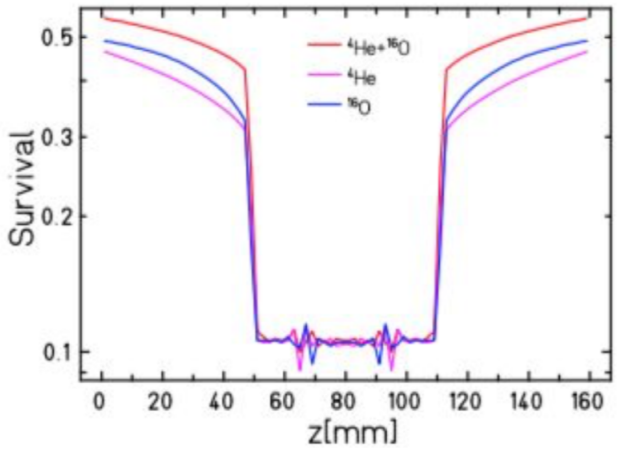

Figure 1.7: Survival distribution for single-ion optimizations with opposite ^4He or ^{16}O fields, and quadruple-field optimization with two pairs of opposite fields (^{16}O + ^{16}O and ^4He + ^4He) [138].

the study and results obtained in the design and realisation of a new scattering system and passive modulation system for future in-vitro and in-vivo studies by using light ions beams.

1.6 New techniques for biological effectiveness enhancement

In the last decades, research efforts in the field of conventional radiotherapy have reduced the dosimetric gap between photons and protons in terms of tumour conformation [33] [84] [86] [132] [134]. Nevertheless, significant accomplishments have marked advances in proton therapy over the same period. Although it can be envisaged that technological developments will continue to improve the dose profiling achievable with photon therapy, the latter cannot be expected to fully match the dosimetric advantage offered by protons since the integral dose difference cannot be overcome. Several radiobiological uncertainties, concerning

the late effects of sub-lethally damaged healthy cells and cell signalling-mediated modifications of the tumour microenvironment, persist that, coupled with economical issues, hamper ^{12}C-based hadrontherapy wider adoption [98]. In the last years, therefore, many strategies have been designed with the aim of increasing the biological effectiveness of light hadron beams. Possible methodologies investigated chemical radiosensitizing agents or, more recently, electromagnetic-driven enhancement of local dose through high-Z metallic nano-particles [68]. All these approaches additionally attempt to exploit energy-dependent mechanisms in order to differentiate conveniently between healthy tissue (entrance channel) and tumor (target).

1.6.1 High-Z nano-particles

Radiation therapy is a critical treatment approach in the radiotherapy field. A sufficient damage to DNA by using ionizing particles can arrest cell growth and prevent metastasis [68]. But the primary drawback of the conventional radiotherapy with X-rays are the collateral damages: there is a little distinction in absorption between healthy and malignant tissues, and thus doses must be limited in order to mitigate unwanted damage to the tumor surroundings. Recently, it has been demonstrated that heavy elements can be radiosensitizers: drugs contain high Z ions can enhance the effects of ionizing radiation through the so-called *high Z effect*, or what has come to be known as *Auger therapy*. Heavy elements have significantly higher photoelectric cross-sections than soft tissue for sub-MeV energies, approximated for *X-ray energies* by the equation:

$$\sigma_{pe} \propto \frac{Z^n}{e^3} \tag{1.3}$$

where σ_{pe} is the cross-section, E=hν is the photon energy, Z is the atomic number, and n is a parameter between 4 and 5 depending on

the value of E. When ionized by X-ray or γ ray energy, mid- to high-Z elements (roughly Br and up) can produce a cascade of low-energy Auger electrons that can locally enhance the effective radiation dose. Dense inorganic nano-particles can also provide radiation dose enhancement that depends upon the composition and size of the particles, uptake of particles into cells, and the energy of the applied radiation. In the last years, Au nano-particles have been under investigation as possible agents for selective amplification of radiation dose in tumors. The promising in-vitro experiments performed by using gold Au nano-particles was followed by several studies examining their mechanism action as well as attempting to optimize the concentration, size, and the energy and dose of applied X-rays [56]. Alternatives to Gold are understudied i.e. Bismuth (Bi, Z = 83) and Platinum (Pt, Z = 78). Dose enhancement is also predicted to increase with decreasing nano-particle size because the smaller nano-particles accumulate closer to the nucleus, where they can cause the greatest damage. However, the radiotherapy approach based on high-Z nano-particles is still discussed by the scientific community because appear complicated to find the correct relation between the deposited local dose and the observed biological effect. Research efforts are underway to increase the efficiency of nano-particle-based treatments and improve the physical and chemical description.

1.6.2 The Targeted Alpha Therapy

At today, the radioimmunotherapy is considered a good candidate to treatment the radioresistant cancer cells. Monoclonal Antibodies (MAbs) that recognize tumor-associated antigens are conjugated to alpha or beta-emitting radionuclides that can provide selective systemic radiotherapy to primary and metastatic tumor sites. A number of targeted agents for radioimmunotherapy have been successfully constructed and

labelled with alpha, beta and Auger emitters [43]. The different physical properties of the radiations confer some advantages and disadvantages in various clinical situations, as schematically illustrated in Figure 1.8. Alpha particles have the advantage of high specificity thanks to the densely ionizing track and short path length (comparable to cell diameters). Beta particles can traverse several millimeters in soft tissue but the ionization is quite sparse. Auger particles have a high ionization probability but energy is deposited in the nanometer scale, being comparable to the size of DNA, so the radioisotope should be used within the cell nucleus for effect.

The Targeted Alpha (α)-particle Therapy (TAT) is a methodology where α-emitting nuclides are conjugated to a carrier, normally an antibody [9]. Generally, an alpha particle with an energy from 4 to 9 MeV can deposit about 100 keV/μm within a few cell diameters (40–90 μm), causing direct DNA double-strand breaks, which lead to cancer cell apoptosis. Today the TAT is potent enough to eradicate disseminated cancer cells or cancer stem cells that are minimally susceptible to chemo- or radio-resistance. The relative biological effect of alpha particles is from 3 to 7, which means that for the same absorbed dose, the acute biological effects of alpha particles are 3 to 7 times greater than the damage caused by external beam photons or beta radiation. This methodology is then ideally suited to liquid cancers or micrometastases. However, the regression of metastatic melanoma lesions after systemic TAT in phase I clinical trial has extended the application to solid tumors also [10].

1.6.3 The Binary Approaches driven by nuclear reactions

As already mentioned, the advent of hadrontherapy has allowed the study and development of new non-invasive therapeutic modalities. In

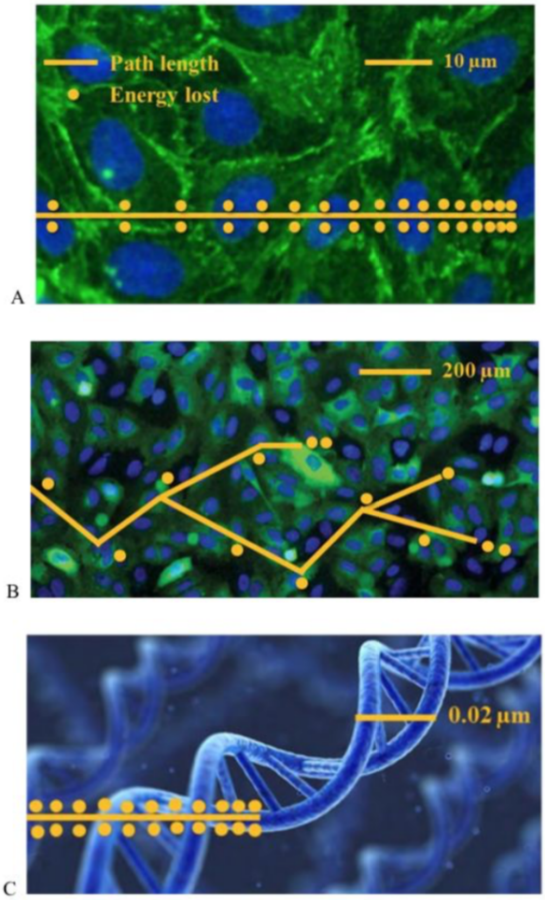

Figure 1.8: Alpha,beta and Auger radiation: the cells were dyedfluorescent green,the nucleus was dyed blue and yellow dots represent the ionization probability. (A) Short path length of alpha particles (a few cell diameters) and densely ionization along the track compared with (B) the longer path length of beta particles and (C) very short path length of Auger particles. The figure A and B were adapted from [43].

this framework, it has been widely investigated the so-called *binary-systems*. A binary system consists of two separate components that are combined to achieve a therapeutic effect. Briefly summarized, it's a two-step procedure: firstly, the patient is injected with a tumor-

localizing drug containing a non-radioactive isotope that has a cross-section of many times greater than the other elements present in tissues such as hydrogen, oxygen, and nitrogen. In the second step, the patient is radiated with an incident ionizing radiation (such as neutron or protons). Beside lose they energy penetrating tissues, the incident particles may also inelastically interact with the injected isotopes, which a subsequent emission of charged particles that can selectively kill tumor cells. The Boron Neutron Capture Therapy (or BNCT) is one of the most famous binary approach already applied in clinical practice. Recently, a new promising method called Proton Boron Capture Therapy (or PBCT) has been proposed. PBCT will be discussed extensively in the Chapter 2 of this thesis work.

The Boron Neutron Capture Therapy

Boron Neutron Capture Therapy is based on the reaction of low energy neutrons with ^{10}B producing two high-LET particles: a ^{7}Li ion and an α particle. The cross section of the $^{10}B(n,\alpha)^{7}Li$ reaction is 3837 barn at neutron thermal energies (Q-value = 2.790 MeV). With a probability of 94%, the reaction gives rise to the Li ion in an excited state, which returns to its fundamental level with a γ emission of 478 keV. In the rest of the cases, the reaction takes place at the fundamental level [74]. A scheme of the reaction channels is reported in Figure 1.9.

The principle of the therapy is that tumoural cells can be loaded with ^{10}B and subsequently irradiated with thermal neutrons. When the reaction takes place inside a cell, the two ionizing particles can cross the nucleus and cause non-repairable damages to the DNA. The potential efficacy of BNCT lies in its selectivity: using, in fact, proper borated compounds the tumoural cells can be loaded with higher boron concentration compared to the normal cells. This fact was experimentally observed since two drugs were synthesized and used in BNCT

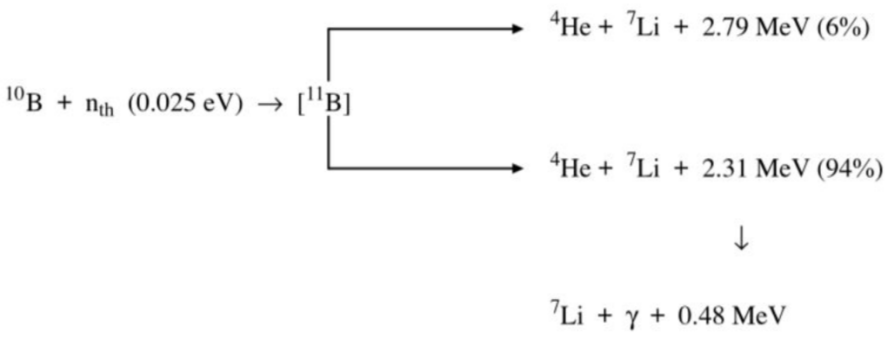

Figure 1.9: Scheme of reaction channels involved into BNCT

research. These are the Boronophenylalanine (BPA) and the Sodium-Dodecaborane (BSH), which are still used in the BNCT research programs for their ability to concentrate the boron atoms preferably in tumoural cells [29] [147]. When irradiating the tissue with neutrons, the total absorbed dose is made up of different components. Some of these dose components are a non-selective background radiation that cannot be avoided, as they originate from the interaction with tissue elements. The selective dose delivery is based on the boron concentration ratio between the tumour and the healthy tissue, that must be as high as possible. Today critical issues that must be addressed include the need for more selective and effective boron delivery agents, the development of methods to provide quantitative estimates of tumor boron content before treatment, and a need for randomized clinical trials with an unequivocal demonstration of therapeutic efficacy [97]. The best survival data from the clinical trials performed for the treatment of glioblastoma multiforme are comparable with those obtained by current standard therapy.

The Proton Boron Capture Therapy

Recently, a method to induce an enhancement of the biological efficacy of proton therapy and called PBCT, has been suggested [158]. It is based on the use of Boron atoms that, if localized inside a tumour mass, promote the occurrence of specific nuclear reactions and consequently the production of high-LET radiation. Specifically, this approach leads to the possibility to exploit the $^{11}B(p,\alpha)^{8}Be$ nuclear fusion reaction channel where three α particles, with an average energy around 4 MeV, are emitted [17]. The $^{11}B(p,\alpha)^{8}Be$ reaction proceeds predominantly by sequential decay through the ground or the first excited state of ^{8}Be, that immediately decays into two secondary α particles. These particles have a range (around 30 μm in water) sufficient to release most of their energy in the cell nucleus, and high-LET values (77 keV/μm), able to severely damage the DNA and produce an enhancement of the proton beam biological efficacy [120]. The first experimental in-vitro test has been performed at Laboratori Nazionali del Sud (LNS) of Istituto Nazionale di Fisica Nucleare (INFN) in Catania (I). The experimental campaign has suggested that the achievable enhanced effect is due to the damage of high-LET particles inside the irradiated cells [39]. At today, other experimental campaigns with different cell lines are ongoing as well as a systematic Monte Carlo and analytical study to describe the observed effect. This is one of the main topic of this thesis work and widely reported and discussed in the Chapter 2.

Chapter 2

A new approach for the radiobiological enhancement of clinical proton beams: the Proton Boron Capture Therapy

In the last years, many strategies have been designed to increase the biological effectiveness of proton beams. In the framework of this thesis the use of p-^{11}B nuclear reaction, triggered by clinical protons generating short-range high-LET alpha particles inside the tumors, thereby allowing a highly localized DNA-damaging action has been investigated [39]. In this Chapter is reported the first experimental results with appearing evident the radiobiological effect due to the boron atoms injection in a biological sample. The first Monte Carlo and analytical calculations performed to reproduce the biological effect as well as a critical study conducted to investigate the potentiality of Boron atoms as a potential imaging technique is described.

2.1 Rationale for the enhancement proton-therapy using the p-B reaction

Charged particle inverted dose-depth profile represents the physical pillar of protontherapy[106]. On the other hand, there is no obvious radiobiological advantage in the use of protons since their LET in the clinical energy range (a few keV/μm, at mid-Spread-Out Bragg Peak, SOBP) is too low to achieve a cell killing effect significantly greater than in conventional radiotherapy [82] [81]. This currently prevents protontherapy from being useful against intrinsically radioresistant cancers. A well-known relationship links physical radiation quality (LET) and its biological effectiveness (RBE), based on the notion that cellular lethality increases with the degree of DNA damage clustering, i.e. complexity, which reflects the nano-scale mode of radiation action [108] [107]. Therapeutic ^{12}C ion beams show an LET at mid-SOBP of about 50 keV/μm, conferring these particles a greater RBE for tumour cell killing, which is the radiobiological justification for their use against radioresistant cancers [131]. However,the non-negligible dose deposition beyond the SOBP due to nuclear fragmentation and economical issues encumber this form of hadrontherapy. In this context, strategies combining greater RBE at cell tumour inactivation while maintaining reasonably low-dose levels in healthy tissues are desirable. Historically, the first approach to predict a tumour-confined increase of radiobiologically effective dose by irradiation with a primary beam is BNCT, which exploits the $^{10}B(n,\alpha)^{7}Li$ reaction [74] [29] . It requires: a) neutrons, whose availability and dosimetry are not trivial; b) selectivity in boron uptake by tumour cells only [78] [147]. Another binary approach has been proposed that exploits the $^{11}B(p,\alpha)^{8}Be$ reaction, whose cross section resonates at 675 keV [17]. In protontherapy such energies are those of protons as they slow down across the tumour region. The

latter eliminates the requirement for selective boron uptake by cancer cell as alpha particles will be not generated, in principle, in healthy tissues where incident proton energy is too distant from that of the cross section maximum; together with the growing number of protontherapy centres, this elegantly bypasses the main drawbacks of BNCT.

2.2 The p-B nuclear fusion reaction cross section

The proton-boron nuclear reaction considered is usually formalized as $^{11}B(p,\alpha)^{8}Be$. It has a positive Q-value (8.7 MeV) and is often referred to as *proton-boron fusion reaction* since the incident proton is completely absorbed by the ^{11}B nucleus [17]. This reaction has gathered interest since the 1930s because of the process ability to produce copious numbers of alpha particles in an exothermic reaction. According to the literature, the p-B nuclear fusion reaction shows three resonant energies (0.162 MeV, 0.675 MeV and 2.64 MeV) and can be described as a two-step reaction. A proton interacting with a ^{11}B nucleus induces the formation of a $^{12}C^{*}$ compound nucleus formed in the 2^{-} or 3^{-} excited state. If the $^{12}C^{*}$ nucleus is formed in its 2^{-} state, it will decay to the first 2^{+} state of ^{8}Be emitting one alpha-particle with $l = 3$ [139]. If the $^{12}C^{*}$ nucleus is formed in its 3^{-} state, then the primary alpha particles can be emitted either with $l = 1$ from the decay to the first 2^{+} ^{8}Be excitated state, or with from the decay to the 0^{+} ^{8}Be ground state. In either case, the remaining ^{8}Be (2^{+} or 0^{+}) nucleus immediately decays into two secondary alpha particles with $l' = 2$. Alpha particles emitted in the first stage present a well-defined energy distribution and are commonly referred as α_0 and α_1 if the ^{8}Be 2^{+} or the 0^{+} states are populated, respectively [92]. In the Figure 2.1 is reported the total cross section for α_1 emission, the most probably reaction channel.

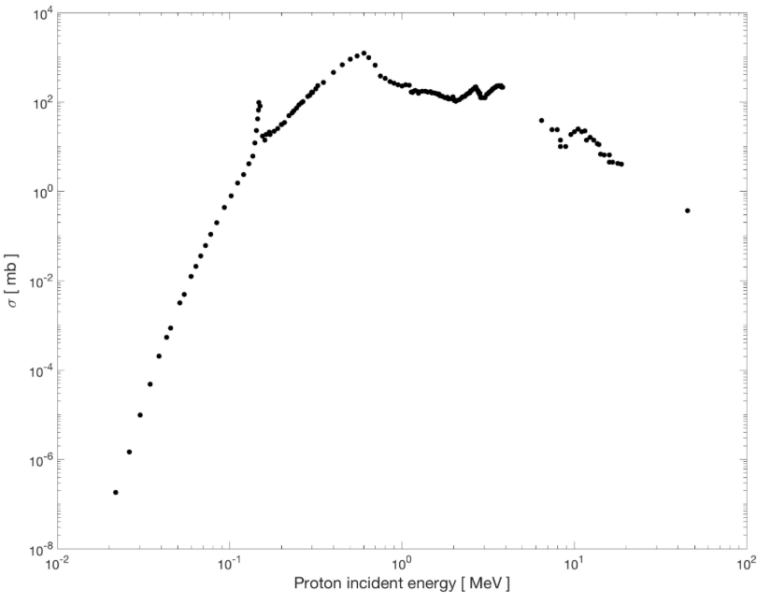

Figure 2.1: Experimental total cross section of $p +^{11} B \rightarrow 3\alpha$ fusion reaction for the most probable α_1 channel decay

Few authors report that a very unlikely fourth channel, characterized by a maximum cross section of 10 μb in the 2.0 - 2.7 MeV energy range, can be also populated. In this case, the $^{12}C^*$ directly breaks into three α particles skipping the intermediate ^8Be stage, resulting in a continuous energy distribution. The emitted α particles exhibit a wide energy spectrum with a predominant energy around 4 MeV as shown in Figure 2.2.

Such a reaction has been considered very attractive for the generation of fusion energy without producing neutron-induced radioactivity [158] [50]. As said above, the p-B fusion reaction is expected to play a strategic role in medical applications improving the effectiveness of protontherapy. Besides the advantage of using a neutron-free nuclear fusion reaction, the relevance of this method stems from the fact that the fusion reaction cross section becomes significantly high at relatively

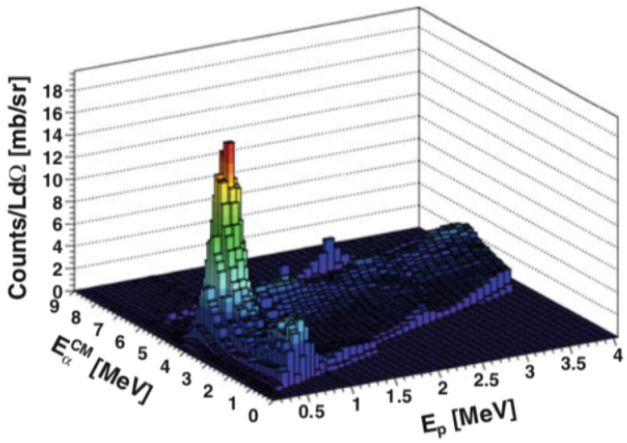

Figure 2.2: Spectrum of alpha particles emitted as a function of incident proton energy

low incident proton energy, i.e. around the Bragg peak region. Actually, in conventional protontherapy, the proton beam is typically slowed down inside the tumour thickness (the Bragg peak region). Thus, most of the beam energy (i.e. dose released) is delivered to the tumour cells. Assuming that a given concentration of ^{11}B nuclei is present preferentially, but not exclusively, in the tumour volume, fusion reaction events can be triggered by the incoming slow protons generating a relevant yield of highly DNA-damaging alpha particles localized in the tumour region.

2.3 Experimental proof of PBCT

2.3.1 BSH enhances cell death following proton irradiation

To test whether the $^{11}B(p,\alpha)2\alpha$ reaction results in an enhancement of cell killing by therapeutic proton beam irradiation, cells from the human prostate cancer line DU145 were irradiated with graded doses

at the middle position of the clinical Spread-Out Bragg Peak of the INFN-LNS protontherapy ocular facility. Irradiations were performed in the presence of two concentrations of BSH. As a control, DU145 prostate cancer cells grown and irradiated without BSH were used. The considered BSH concentrations were equivalent to 40 ppm (parts per million) and 80 ppm of ^{11}B. These values were chosen in order to maximize the ^{11}B content in the cells on the basis of what is done for the ^{10}B-enriched BSH for BNCT [147].

Boron treatment enhanced proton biological effectiveness resulting in a significant increase of mortality of DU145 cells. Cells that were irradiated after pre-treatment with, and in the presence of, boron-containing BSH exhibited a greater radiosensitivity in comparison with cells exposed to radiation alone [96]: BSH-treated cells yielded a much steeper clonogenic dose-response curve than that obtained for cells grown and irradiated in BSH-free medium (Figure 2.3).

The clonogenic Survival Fraction (SF) following irradiation with protons alone was best fitted to a linear-quadratic function of dose, i.e. SF = exp (-α*D-$\beta * D^2$), with data from proton irradiation in the presence of BSH exhibiting a purely exponential behaviour as a function of dose. Least-square fitting parameters are reported in Table 2.1.

A slight yet not statistically significant effect due to boron concentration was observed. Based upon the measured survival dose-responses, a calculated Dose Modifying Factor (or DMF) of 1.46 $\pm$ 0.12 was determined at the 10 survival level (DMF10).

2.3.2 Dependence of BSH-mediated cell killing enhancement upon proton energy

The pB nuclear fusion reaction critically depends on the incident proton energy; hence, its radiobiological effectiveness can be expected to vary along the clinical proton SOBP. To verify this hypothesis, the in-

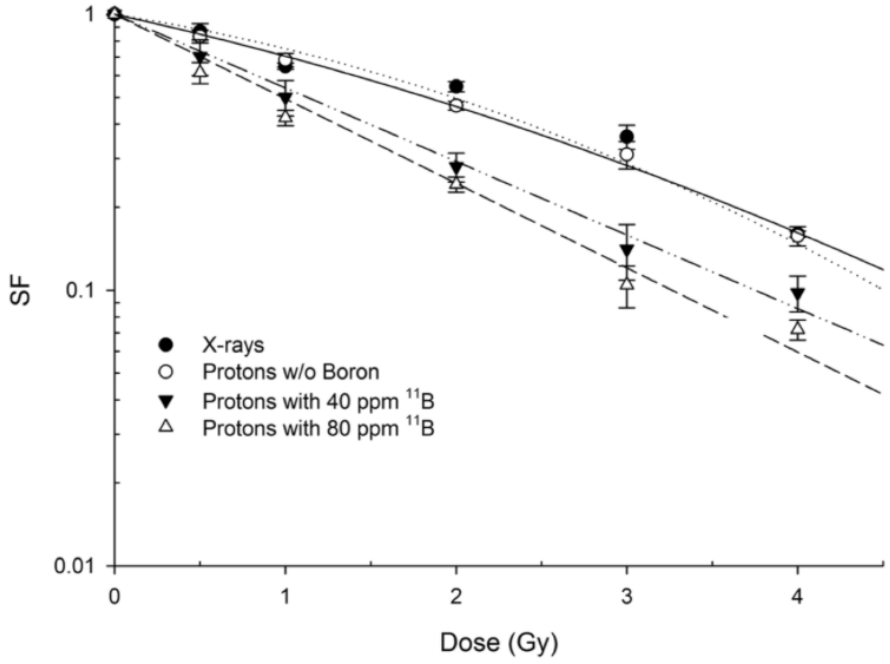

Figure 2.3: Clonogenic dose response curves of DU145 irradiated with therapeutic protons in the presence or absence of BSH at mid-SOBP. Data are weighted mean values plus standard error from four independent experiments in the case of proton irradiation in the absence of BSH (open circles) and in the presence of the compound at highest concentration used (80 ppm, open triangles) Two experiments were performed with cells irradiated in the presence of 40 ppm of ^{11}B. X ray-irradiation survival data are also shown for comparison.

duction of cell killing in the presence of the boron compound at the concentration of 80 ppm ^{11}B (Figure 2.3), was investigated irradiating the cancer DU145 cell line at the beam entrance (P1 position), at the SOBP distal end (P3 position), and at the middle of the SOBP (P2) as above reported (Figure 2.4).

The panel in Figure 2.5 shows the clonogenic survival dose-response curves derived from the three positions along the SOBP, in the absence

	alpha(Gy^{-1})	**beta**(Gy^{-2})
X ray irradiation	0.222 ± 0.062	0.064 ± 0.014
Proton irradiation in the absence of BSH	0.314 ± 0.022	0.035 ± 0.007
Proton irradiation with 40 pm 11B	0.614 ± 0.069	-
Proton irradiation with 80 pm 11B	0.705 ± 0.033	-

Table 2.1: Cell killing dose-response fitting parameters. Calculated values for α and β parameters are obtained from the fitting of experimental data by linear-quadratic model for radiation-induced cell killing, are reported. Statistically equivalent to zero β values were found for proton irradiation in presence of BSH.

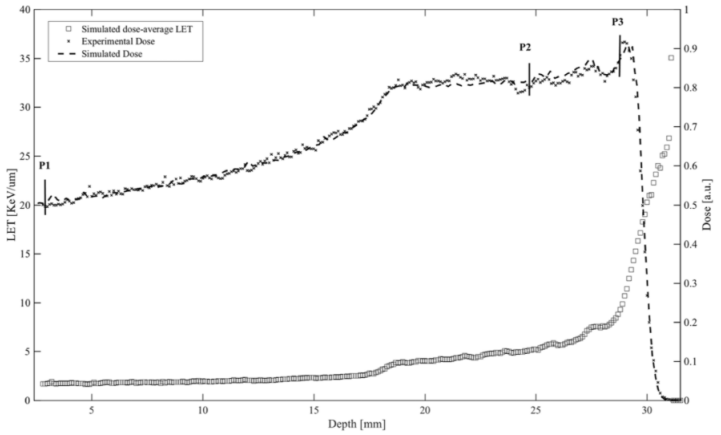

Figure 2.4: Cell irradiation along the proton SOBP. Measured dose and calculated LET profile for cellular irradiation at different positions along the clinical proton SOBP at INFN-LNS. Shown are the three depths along the SOBP at which cells were irradiated and the corresponding calculated LET values (open squares). Dose profiles as obtained by direct measurement by Markus chamber and by Monte Carlo simulations

or presence of BSH.

In line with the expected variation in cell radiosensitivity along a

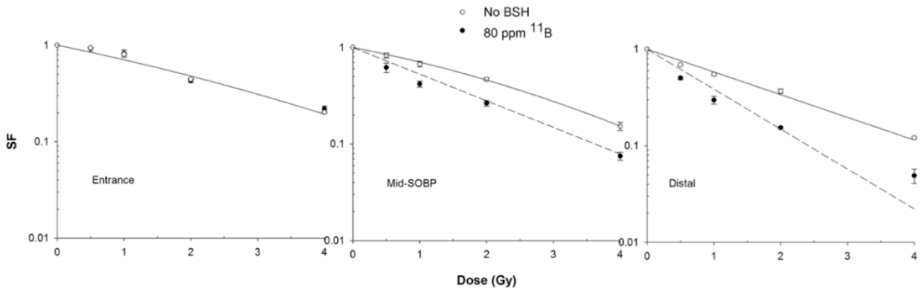

Figure 2.5: Clonogenic survival along the proton SOBP. Data shown here refer to dose-response curves obtained at positions P1, P2 and P3 as indicated in Figure 2.4along the clinical proton SOBP.

clinical SOBP, proton irradiation alone resulted in a progressive increase in cell killing from P1 to P3. Interestingly, data clearly show no effect of BSH at the beam entrance. A DMF of about 1.4 was confirmed at 10% cell survival at mid-SOBP: here, fitting parameters were α = (0.309 $\pm$ 0.022) Gy^{-1} and β = (0.040 $\pm$ 0.006) Gy^{-2} for proton irradiation without BSH and α = (0.653 $\pm$ 0.018) Gy^{-1} in the presence of 80 ppm ^{11}B. At the distal end of the SOBP, however, BSH appeared to be even more effective with a recorded DMF of 1.75 $\pm$ 0.13: at this position, cell killing was best described by a pure exponential for both protons alone and protons in the presence of BSH, with values for the α parameter of (0.541 $\pm$ 0.027) Gy^{-1} and (0.952 $\pm$ 0.053) Gy^{-1}. These experimental results and particularly the lack of a measurable effect due to the presence of ^{11}B at beam entrance where the incident proton energy is the highest, confirm that the enhancement of biological effectiveness is caused by the occurrence of p-B nuclear fusion events, which have a higher probability (i.e. higher cross section) at relatively low energy (MeV level) of the incoming protons, i.e. towards the end of their range.

2.4 An analytical estimation of the radiobiological effect

Monte Carlo simulations coupled to analytical calculations were performed to estimate the number of alpha particles generated along the SOBP from the $^{11}B(p,\alpha)2\alpha$ reaction and quantify the emission necessary to produce the observed radiobiological effect. The experimental total cross section was directly applied to proton energy spectra extracted along the Bragg Peak. The estimated alpha particles yield was then applied to quantify the total dose-average LET and estimate the radiobiological observed effect. A detailed description of the application used for the Monte Carlo calculations as well as the algorithm adopted for LET computing and reproducing the radiobiological effect are reported in Chapter 4, 5 and 6 respectively.

2.4.1 Evaluation of the alpha particles yield

`Hadrontherapy` is a publicly available Geant4 application and was used to reproduce the whole beamline and the cells irradiation conditions during the radiobiological experiments. A standard water phantom for clinical absolute dosimetry, divided into slices of 100 μm, was also simulated: here particles fluence, energy spectra, dose and LET distribution were recorded. The energy spectra of the incident proton beam calculated along the SOBP are reported in Figure 2.6

The alpha particles produced were estimated applying experimental cross section (Figure 2.1) to the simulated energy spectra (2.6). Specifically, alpha particle yields were calculated assuming a ^{11}B layer of 100 μm and a density of $8 * 10^{-5}$ g/cm^3 corresponding to 80 ppm of ^{11}B, that is the concentration used in the experiments. A number of histories of the order of 10^9 were simulated to deliver a total dose of 2 Gy at the middle of the SOBP, according to the experimental results. The

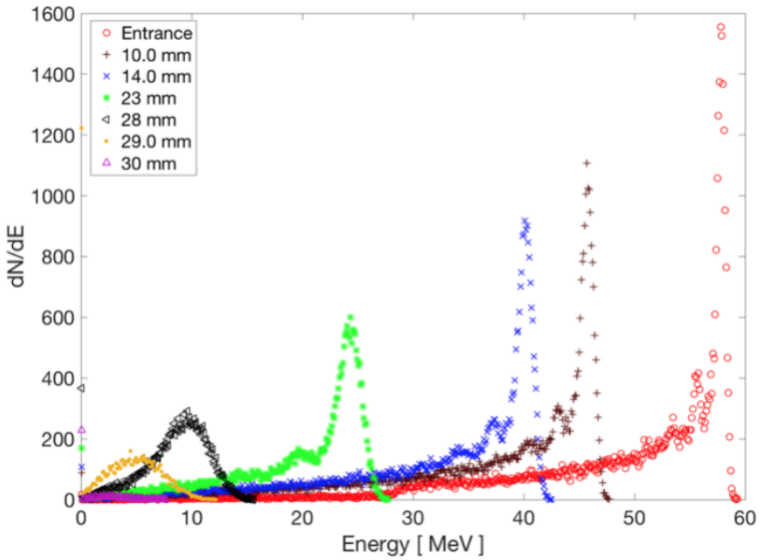

Figure 2.6: Energy spectra of the incident proton beam calculated at several depths along SOBP

results are reported in Figure 2.7 where the SOBP (in arbitrary units) is plotted along with primary proton fluence and the corresponding generated alpha particles. The dose related to each components, the number of incident protons and the emitted alpha particles are shown in Figure2.8.

2.4.2 The LET and RBE calculation

The estimated alpha energy spectrum has been then used to calculate the radiobiological quantities of interest like Linear Energy Transfer and the biological damage expressed in term of DMF. In Figure 2.9 the average dose-LET along the SOBP calculated in two different conditions is reported:

- Condition 1: when only primary incident protons are considered;
- Condition 2: when the contribution of the generated alpha parti-

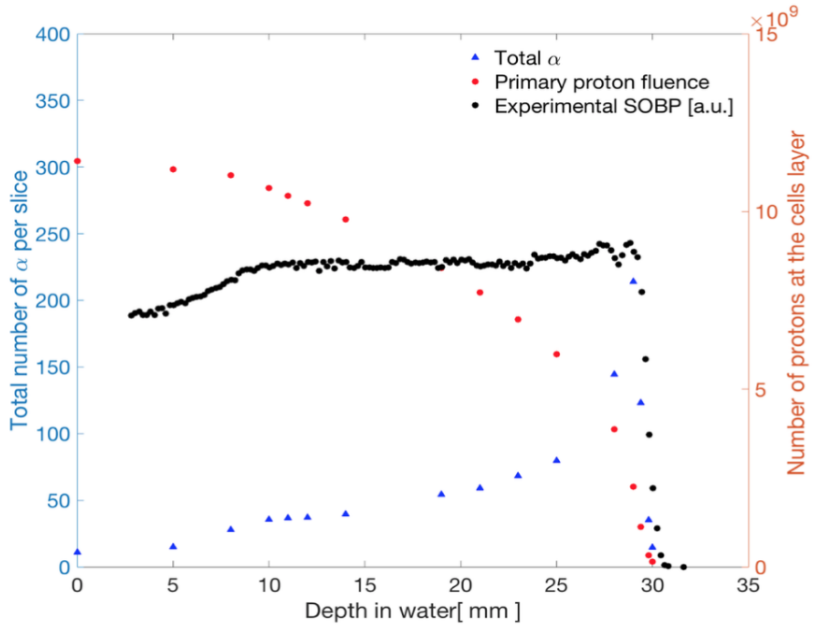

Figure 2.7: Number of alphas particles generated in the p-B reaction. Fluence of primary protons and total alphas from the reaction $^{11}B(p,\alpha)2\alpha$ produced in each slice. The experimental dose distribution is also shown in arbitrary units.

cles is added to the primary protons.

LETs for the Condition 1 and 2 were estimated with Equations 2.1 and 2.2, respectively:

$$LET_p = \frac{dE_1^p \cdot \frac{dE_1^p}{dx_1^p} + dE_2^p \cdot \frac{dE_2^p}{dx_2^p} + ... + dE_N^p \cdot \frac{dE_N^p}{dx_N^p}}{dE_1^p + dE_2^p + ... + dE_N^p} \tag{2.1}$$

$$LET_p{+}LET_\alpha = \frac{dE_1^p \cdot \frac{dE_1^p}{dx_1^p} + ... + dE_N^p \cdot \frac{dE_N^p}{dx_N^p} + dE_1^\alpha \cdot \frac{dE_1^\alpha}{dx_1^\alpha} + ... + dE_N^\alpha \cdot \frac{dE_N^\alpha}{dx_N^\alpha}}{dE_1^p + ... + dE_N^p + dE_1^\alpha + ... + dE_N^\alpha} \tag{2.2}$$

In both cases, at middle of SOBP (in water), average dose-LET resulted to be 5.69 keV/μm. Appear then evident that to obtain an

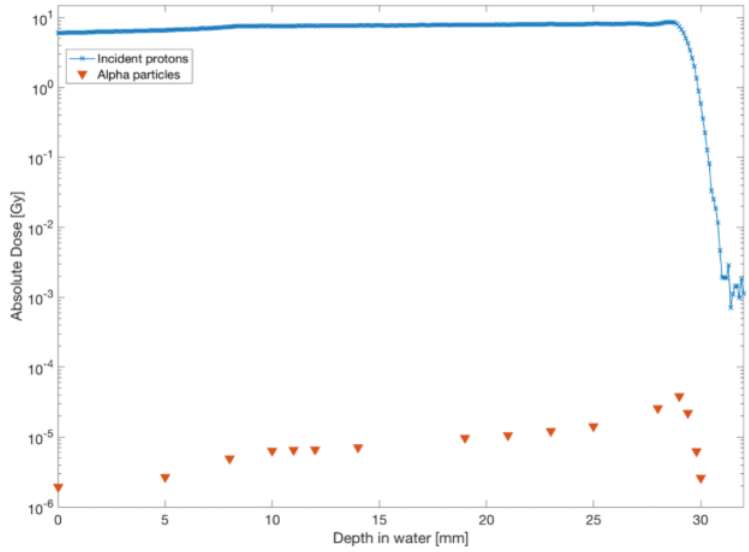

Figure 2.8: Dose distribution as a function of the depth for incident protons and generated alpha particles, supposed that 2 Gy are released at the MID-SOBP, according to the experimental data

evaluable increment in the LET value is necessary to consider some different order of magnitude in the estimated alpha particles yield. The expected effect of the $^{11}B(p,\alpha)2\alpha$ reaction seems to be negligible, being the dose and LET due to this reaction channel orders of magnitude lower than the contribution due to the primary protons. When, at the same depth, the presence of 10^5 alphas is considered applying Formula 2.2, the augmented averaged LET due to the high-LET alpha particles (Condition 2) resulted 12.40 keV/μm. In Table 2.2 is reported the necessary LET value for the experimental SOBP (Figure 2.2) to obtain the experimental dose modified factor at the positions P1, P2 and P3.

The DMF estimation reported in the Table 2.2 has been performed using the parametrisation and the MKM model described in Chapter 6. The Surviving Fraction curve, experimentally measured without boron, has been chosen as reference to demonstrate the enhancement effect.

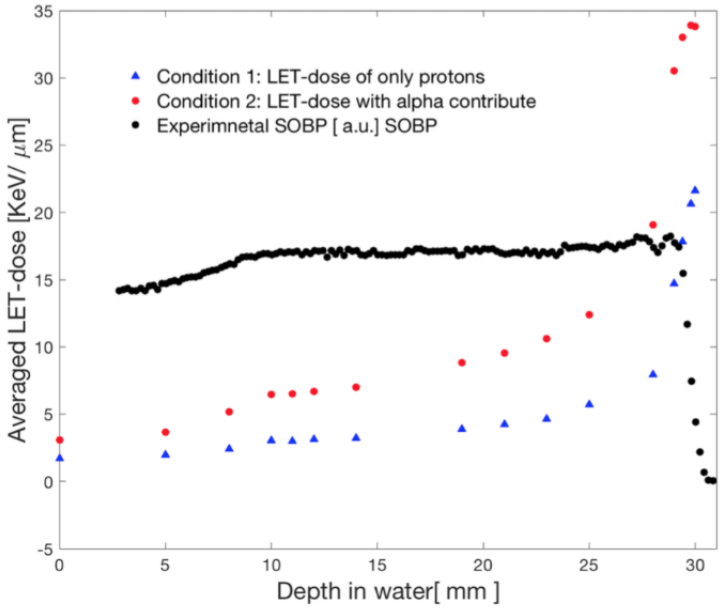

Figure 2.9: Estimated increment of LET-dose when alphas from the p-B reaction are taken into account. Averaged LET-dose calculated with Equation 2.1 when only primary protons are considered (blue triangles) and when the contribute of the generated alphas is considered (red crosses) applying Equation 2.2. The experimental dose distribution is reported in arbitrary units.

Position	**Depth in water [mm]**	**Proton LET [KeV/μm]**	**Total LET [KeV/μm]**	**Dose Modifying Factor (DMF)**
Entrance	5	1.96	3.66	1.17± 0.37
Mid-SOBP	21	4.24	9.53	1.36± 0.44
Distal	29.8	20.62	33.92	2.04 ± 0.66

Table 2.2: DMF estimation (last column) at three different depths along the SOBP; Proton dose averaged LET and Total dose averaged LET due to the contribute of alpha particles are also reported.

The estimation of theoretical DMF calculated at the same experimental positions along the Bragg curve has shown a maximum deviation of the order of 15% in comparison to the experimental results obtained with the clonogenic analysis (Section 2.3). To further substantiate the reasonableness of the analytical calculation, has been applied the MKM model considering the supposed incremented total dose averaged LET at the experimental MID-SOBP position. In Figure 2.10 is reported the Survival Fraction curve calculated with and without boron concentration as well as the experimental data.

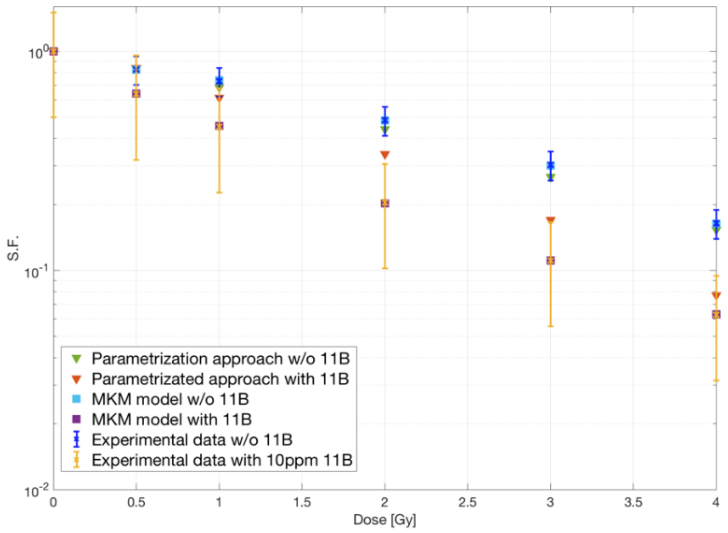

Figure 2.10: The Experimental survival fraction with and without boron injection (yellow and blue triangles, respectively) as a well as the estimated damage calculated by applying MKM model ad parametrized approach described in Chapter 6

In conclusion, radiobiological data suggest that the $^{11}B(p,\alpha)2\alpha$ reaction is a good candidate to justify the observed increase in the biological effectiveness of the clinical proton beam. However desirable, it's not simple provide analytical computation able to explain the bio-

logical results, for instance by correlating the biological effect with the total number of α-particles that can be expected to be generated under our experimental conditions. The current knowledge of biological radiation action has nonetheless established that, the biological effects of low-energy high-LET radiations cannot be interpreted solely on the basis of macroscopic concepts like the absorbed dose or the average LET distributions. This is due to the intrinsically inhomogeneous nature of energy deposition events along radiation tracks, which becomes more significant with their increasing ionization density. Therefore, micro- and nano-dosimetric approaches must be taken into account to analyse the effects arising at cellular level. In addition, the role of extra-targeted phenomena, such as the bystander effect whereby cells that have not been traversed directly by radiation tracks may express cytogenetic damage, is still largely undetermined in such scenario thereby contributing to the overall uncertainty between the physical dose distribution at the micro or nano-dosimetric level and at the cellular one.

2.5 Imaging potentialities of PBCT : A study of gamma-ray emission by proton beam interaction with injected Boron atoms for future medical imaging applications

The presence of Boron inside the neoplastic cells can also be exploited to spatially map the biological distribution of the Boron and, hence, the tumour regions where the RBE enhancement occurs [120] [119]. Characteristic gamma prompt emission from p-B interaction can in fact be detected, thus allowing the determination of the spatial distribution of their emission point. This possibility was discussed by D.K. Yoon et

al. in [158] who proposed the use of ^{11}B isotope. In this thesis has been to investigate the potentiality of this technique. A critical analysis revealed that the vision described in [158] is quite optimistic for two reasons. First, the prompt-gammas of 0.718 MeV are emitted from the ^{11}B(p,p')^{11}B inelastic scattering channel (and not the fusion channel, as they erroneously state), and they are the same as generated by the interaction of protons with the main constituents of the human body (^{12}C and ^{16}O). Moreover, the maximum concentration of B nuclei that can be reached in a tumor, conferring minimal cell toxicity, is in the order of 10^{-5} g/cm^3 [147], five orders of magnitude less than the value proposed in [158]. With such small densities, prompt gamma rays emitted at high incident proton energies are completely drowned out by the gamma particles generated by the interaction of the proton with the biological tissue.

The purpose of this study has been then to investigate the configuration discussed in [158], determining its real feasibility and establishing its limitations. Furthermore, a complementary approach was found. The gamma prompt spectra obtained with proton irradiation on ^{11}B and ^{10}B have been measured in a clinical configuration during an experimental campaign carried out at LNS-INFN. The same set-up has been simulated using the Talys [80] nuclear reaction code and outputs compared with the experimental results. This procedure enabled the selection of useful prompt-gamma lines and simultaneous validation of the code. Once validated, Talys was adopted to extend the study, considering different materials and to make additional considerations for the future improvement of this technique. The comparison has shown that the emission from the Boron atoms is not sufficient to produce a detectable signal at least at high energies. In this framework, a new approach based on using natural Copper directly bonded to Boron was proposed. The characteristic gamma prompts from Copper are characterized by

energies in a region far from that present in the background. This will permit their detection avoiding the unwanted interference coming from human body elements.

2.5.1 Imaging by gamma prompt emission

When a sample is irradiated with energetic protons, several nuclear reactions, such as (p, p'γ), (p, γ) and (p, α) with gamma prompts are emitted in a temporal scale ranging in the 10^{-19} to 10^{-9} s. These occur also during a typical proton-therapy treatment, where many secondary prompt gamma rays are induced from the proton-tissue interaction. In particular, discrete gamma ray emission can be generated from the excited states of ^{16}O and ^{12}C that are the most abundant human tissue constituents. In the last decade, many experimental studies [137, 125] and simulations [149, 124] have shown that gamma prompt detection can be adopted as online dose monitoring and beam range estimation [87], as well. In this investigation, four characteristic gamma peaks (0.429 MeV, 0.719 MeV, 1.022 MeV and 1.435 MeV), coming from the p-^{11}B and p-^{10}B targets, were investigated in order to evaluate their potential use in imaging applications. These peaks are generated by both B isotopes, even with different mechanisms (prompt and non-prompt), and from different reaction channels. Table 2.3 summarizes the reaction channels generating the investigated gamma lines. The maximum total production cross sections per channel and the corresponding emission mechanisms, are also reported.

According to literature [63, 92, 32], the gamma-prompts emitted from p-^{11}B and p-^{10}B interactions have the same energy as the ones generated by the interaction of protons with ^{16}O and ^{12}C (see Table 2.4).

E_γ	Target	Product	Nuclear Reaction		Emissio Mechanism	Maximum gamma emission cross section[mb]	Nuclide production cross section [mb]
0.429	^{10}B	^{7}Be	$^{10}B(p,\alpha)^{7}Be^{*}$	$^{7}Be^{*0.429} \rightarrow$g.s.	PROMPT	27.8 at 19 MeV	56.8 at 19 MeV
	^{11}B	^{7}Be	$^{11}B(p,n\alpha)^{7}Be*$		PROMPT	17.18 at 19 MeV	287.7 at 19 MeV
0.718	^{10}B	^{10}B	$^{10}B(p,p')^{10}B^{*}$	$^{10}B^{*0.718} \rightarrow$g.s.	PROMPT	163.5 at 11 MeV	253.8 at 11 MeV
	^{10}B	^{10}B	$^{10}B(p,n)^{10}C*(\beta^{+})^{10}B^{*}$		NO-PROMPT	-	134.4 at 12 MeV
	^{11}B	^{10}B	$^{10}B(p,2n)^{10}C*(\beta^{+})^{10}B^{*}$		NO-PROMPT	-	2.39 at 30 MeV
	^{11}B	^{10}B	$^{11}B(p,d)^{10}B*$		PROMPT	82.09 at 22 MeV	126.9 at 22 MeV
1.022	^{10}B	^{10}B	$^{10}B(p,p')^{10}B^{*}$	$^{10}B^{*0.718} \rightarrow$ g.s.	PROMPT	38.5 at 11 MeV	253.8 at 11 MeV
	^{11}B	^{10}B	$^{11}B(p,d)^{10}B^{*}$		PROMPT	20.72 at 22 MeV	26.9 at 22 MeV
1.430	^{10}B	^{10}B	$^{10}B(p,p')^{10}B^{*10}$	$^{10}B^{*2.15} \rightarrow ^{10}B^{*0.718}$	PROMPT	10.26 at 11 MeV	253.8 at 11 MeV
	^{11}B	^{10}B	$^{11}B(p,d)^{10}B*$		PROMPT	6.61 at 22 MeV	126.9 at 22 MeV

Table 2.3: Summary of the reaction channels and corresponding characteristic gamma emission, occurring in the p-^{10}B and p-^{11}B interactions. For each peak, the considered target and corresponding residual nucleus are reported (columns two and three); In columns four and five the reaction channels are described and the de-excitation producing the gamma (column five); Finally, the emission mechanism (column six) and the maximum gamma production total cross sections (column seven) are reported as well as the nuclide production cross sections (column eight).

E_γ [MeV]	Target	Product	Nuclear Reaction		Emission mechanism
0.429	^{12}C	^{7}Be	$^{12}C(p,^{6}Li)^{7}Be^{*}$	$^{7}Be^{*0.429} \rightarrow$ g.s	PROMPT
	^{16}O	^{7}Be	$^{11}B(p,X)^{10}B^{*}$		PROMPT
0.718	^{12}C	^{10}B	$^{12}C(p,^{3}He)^{10}B^{*}$	$^{10}B^{*0.718} \rightarrow$ g.s.	PROMPT
	^{12}C	^{10}B	$^{12}C(p,t)^{10}C*(\beta^{+})^{10}B^{*}$		NO-PROMPT
	^{16}O	^{10}B	$^{16}O(p,^{7}Li)^{10}C^{*}(\beta^{+})^{10}B^{*}$		NO-PROMPT
	^{16}O	^{10}B	$^{16}O(p,X)^{10}B^{*}$		PROMPT
1.022	^{10}B	^{10}B	$^{12}C(p,^{3}He)^{10}B^{*}$	$^{10}B^{*1.022} \rightarrow$ g.s.	PROMPT
	^{11}B	^{10}B	$^{16}O(p,X)^{10}B^{*}$		PROMPT
1.430	^{12}C	^{10}B	$^{12}C(p,^{3}He)^{10}B^{*}$	$^{10}B^{*1.430} \rightarrow$ g.s.	PROMPT
	^{16}O	^{10}B	$^{16}O(p,X)^{10}B^{*}$		PROMPT

Table 2.4: Summary of reaction channels occurring in the p-^{12}C and p-^{16}O interactions generating the gamma lines of interest. For each peak the target and corresponding residual is reported (columns two and three); The nuclear reaction and emission mechanism is also included (columns four and five). Column six indicates the emission mechanism.

2.5.2 Experimental set-up

Experimental runs have been performed at the *zero-degree* experimental hall of INFN-LNS where 62 MeV proton beams, accelerated by the LNS superconducting cyclotron, are available. Gamma spectra were measured using a cylindrical, high-purity germanium detector (HPGe) GEM series model 70220-S, connected to a signal amplifier and an analog-to-digital converter MCA Amptek model 8000-A. The detector has a nominal energy resolution of 1.84 keV (at 1.33 MeV, as from ^{60}Co) and a relative efficiency of 60.08%. Its sensitive volume has dimensions of 69.2 mm and 81.8 mm in diameter and height, respectively. Energy calibration was performed using a ^{152}Eu source. The experimental set-up is shown in Figure 2.11. Targets were positioned at 15 cm from the beam exit point corresponding with the Kapton window, making the interface between vacuum and air. The HPGe detector front surface was 7.5 cm from the cylindrical target, with its axis perpendicular to the beam.

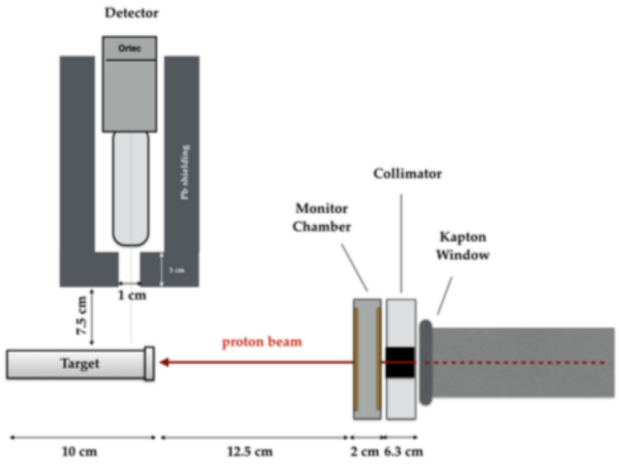

Figure 2.11: Schematic representation of the experimental setup used for the gamma spectra measurement

The 62 MeV proton beam exits in air, traversing a 50 μm Kapton. It is then intercepted by a PMMA (PolyMethylMethacrylate) collimator fixing the beam circular spot size at 10 mm in diameter. Just beyond the collimator, a transmission ionization chamber is adopted for the on-line monitoring of the total released dose. It is composed by two Kapton/Gold foils 25 μm in thickness, separated by 9 mm of air [44]. An electric field of 800V between the two foils ensures the complete charge collection at the adopted rate. The role of the transmission chamber was essential to normalize the number of detected gamma rays with respect to the total incident proton flux. Finally, the beam reaches the Boron sample and it is completely stopped in it with a range of 3.41 $\pm$ 0.14 cm. The detector was shielded with a 5 cm thick lead wall to minimize the environmental gamma radiation. The Boron targets, produced at the INFN-LNS chemical workshop, consisted of two Mylar cylinders, 10 cm in length and with an external and internal diameter of 31 mm and 15 mm, respectively. One of the two targets is shown in Figure 2.12. They were filled alternatively with pressed ^{11}B and ^{10}B powders, and in both cases the resultant density was 1.15 g/cm^3. The bases of the Mylar cylinders were plugged with two 25 μm kapton foils to avoid Boron powder dispersion and at the same time to minimize the proton beam energy loss.

2.5.3 Experimental results

The two gamma spectra obtained with the irradiation of ^{10}B and ^{11}B are shown in Figure 2.13, both normalized to the same beam flux of 1.69*10^7 particles. They were acquired in a fixed time interval of 500 seconds. Proton beam current was kept at the value of about 15 pA at sample surface, in order to reduce pile up effects. Spectra were then normalized taking into account the total beam flux.

Both spectra show the 0.511 MeV peak, originating from positron

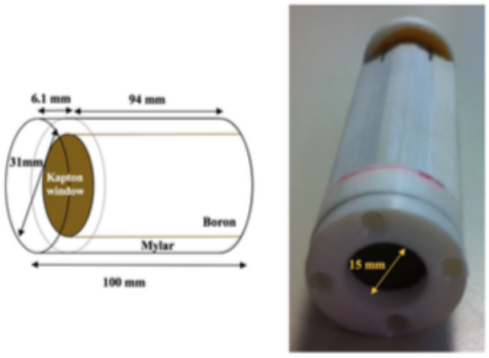

Figure 2.12: Right: picture of one of the irradiated Boron targets; the mylar cylinder has an internal diameter of 15 mm and its thickness is chosen to minimise gamma attenuation. It contains the pressed Boron powder; Two kapton foils on its base prevent Boron powder leakage. Left: the target sketch with the mylar cylinder, the Boron insert and the kapton window.

annihilation after electron-positron pair production in the target material and in the detector itself. Moreover 0.429 MeV, 0.718 MeV, 1.022 MeV and 1.435 MeV peaks are present in agreement with the reactions reported in Table 2.3. Experimental gamma spectra have been compared against Talys analytical simulations performed with the *outgamdis* modality [62]. Such a modality corresponds to an option in Talys which permits the gamma emission yield calculation taking into account all possible nuclear transitions. The real experimental concentration of Boron nuclei on the target was considered. Furthermore, the experimental detection solid angle and the total production cross sections were taken into account in the total gamma yield calculation. The main aim of this study being the comparative evaluation of the different gamma contribution from ^{11}B and ^{10}B isotopes irradiated with clinical proton beams, it was compared the relative difference between the analytical (Talys) and experimental data. Table 2.5 reports the percentage

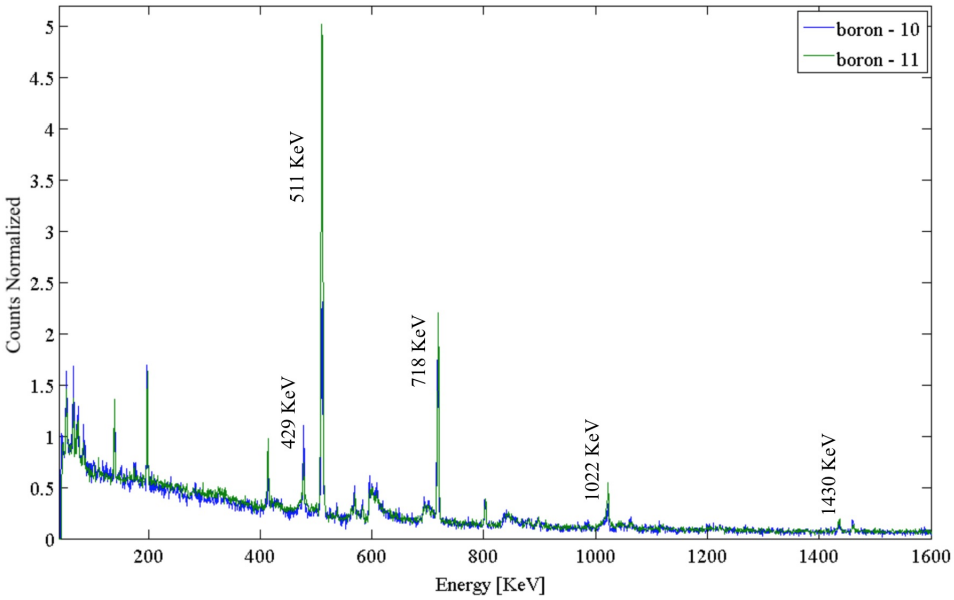

Figure 2.13: Normalized gamma rays spectra from p-^{10}B (blue) and p-^{11}B (green). The energies of the four studied peaks are indicated together with the annihilation peak.

difference of each gamma yield line produced from p-^{11}B and p-^{10}B interactions. The total count **N** of each considered gamma line has been evaluated for both targets, as the integral under the correspondent peaks. The counts percentage difference obtained as the difference between ^{11}B and ^{10}B counts divided by ^{11}B yield in the experimental case (Δ_{exp}) has then been compared with the corresponding one (Δ_{ana}) calculated with the Talys analytical simulations. The results of these comparisons have been reported in Table 2.5 for three different target positions, corresponding to different proton beam energy intervals.

The differences reported in Table 2.5 between the calculations and experimental observations are all within the acceptable precision required for it (estimated to be the order of 40%) and making us confident

$\mathbf{E_\gamma}$	**Energy [MeV]**	$\Delta_{exp}\%$	$\Delta_{ana}\%$	$\lvert\Delta_{tot}\%\rvert$
	62-50	59,3 ± 8,5	74,2	14,8 ± 8,5
0.429	56-43	59,9 ± 9,2	72,8	12,9 ± 9,2
	43-28	59,6 ± 9,2	66,7	7,1 ± 9,2
	62-50	54,1 ± 7,0	51,1	2,9 ± 7,0
0.718	56-43	52,0 ± 9,1	57,6	5,5 ± 9,1
	43-28	54,2 ± 8,5	63,4	9,2 ± 8,5
	62-50	67,6 ± 7,7	71,5	3,6 ± 7,7
1.022	56-43	67,7 ± 7,8	74,2	6,5 ± 7,8
	43-28	63,4 ± 8,9	77,9	14,5 ± 8,9
	62-50	56,4 ± 6,7	55,7	1,1 ± 6,7
1.430	56-42	57,5 ± 6,9	60,8	3,2 ± 6,9
	44-28	61,0 ± 5,6	66,3	5,2 ± 5,6

Table 2.5: In the second column the energy range corresponding to a specific cylinder position with respect to the detector slit, is reported. The percentage difference of each gamma yield line produced from p-^{11}B and p-^{10}B interaction for the experimental results (column three) and analytical calculation (column four) is also shown. The absolute value of the comparison between these quantities is reported in the fifth column. The error reported in the third and fifth columns has been calculated considering both the statistical uncertainty and an uncertainty of 1 mm in the cylinder positioning.

in the efficacy of Talys for the evaluation of the concrete possibilities to use injected Boron for imaging purposes in a clinical configuration.

2.5.4 Gamma emission evaluation in a real treatment configuration

Many investigations have been carried out to maximize the Boron concentration in a tumor [97, 78]. Recently, it has been demonstrated that the maximum Boron concentration, ensuring the minimal cell toxicity and the maximum absorption, is in the order of 80 ppm or 10^{-5} g/cm^3 [147]. On the other hand ^{12}C and ^{16}O are commonly present in the human body with concentrations of the order of 0.18 g/cm^3 and 0.65 g/cm^3 for Carbon and Oxygen, respectively [6]. The gamma yields of the four considered peaks, expressed as number of transmitted photons per mm and per incident proton, are reported in Figure 2.14 as function of the proton incident energy. Results for ^{11}B, ^{10}B, ^{12}C and ^{16}O, are shown. The gamma yields coming from p-^{12}C and p-^{16}O are at least two orders of magnitude higher (Figure 2.14) than those coming from the proton-B reactions with an incident proton energy greater than 30 MeV. This will make the gamma prompt emission from injected Boron in a biological tissue difficult to use for imaging purposes. It will be almost impossible obtain a map of the dose distribution during the treatment. A specific concentration of boron nuclei could be used for the verification of the proton range.

Following the above considerations, in order to maintain the proton-Boron therapeutic role while simultaneously improving the imaging capability, we suggest the use of Boron in combination with natural Copper atoms. Copper can be easily bound to the dipyrromethene, BodiPy, [157] a carrier molecule whose use is extensively documented [15] and is applied for biological labelling, drug delivery, imaging, sensing, and theranostics. Natural Copper consists of two stable isotopes:

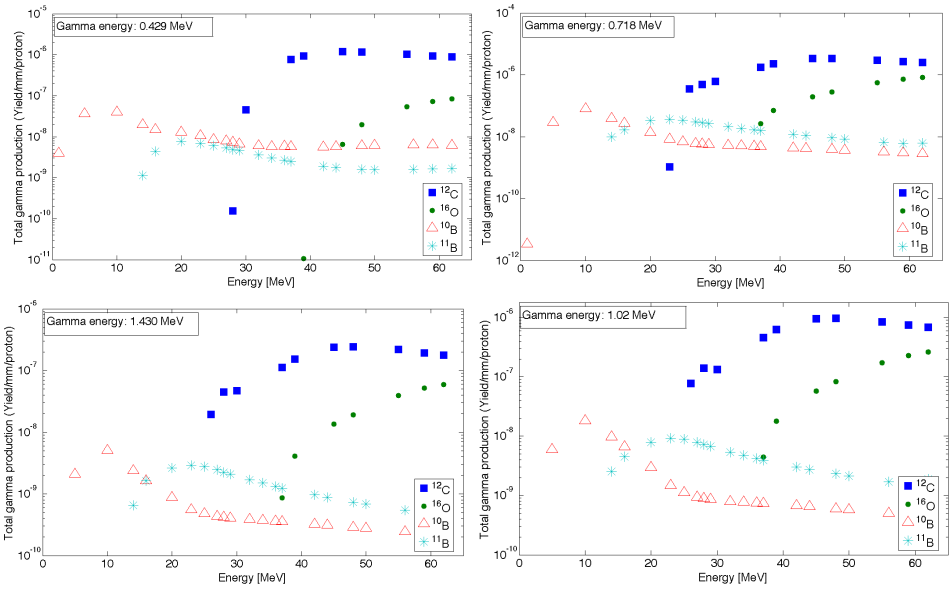

Figure 2.14: The total gamma production per mm of traversed material and per incident proton, calculated using Talys for each gamma line. Curves have been calculated considering the realistic concentration of ^{10}B, ^{11}B, ^{12}C, ^{16}O.

^{63}Cu and ^{65}Cu (abundance of 69.15% and 30.85%, respectively). The ^{63}Cu, specifically can emit several peaks in the energy range between 0 to 2 MeV, generated mostly in the ^{63}Cu(p,p')^{63}Cu elastic reactions. A combination of different prompt gamma rays could be useful for a mapping dose. Specifically, the 1.3 MeV gamma line could be used, being located very far from the spectral region where there are abundant emissions from biological components. The total maximum production cross section for this gamma line is 120 mbarn at 35 MeV. Another gamma peak, that could be a good candidate for the mapping dose, is the gamma line at 0.99 MeV that shows a cross section of 450 mbarn at

17 MeV of incident proton energy. In conclusion, the high p-B nuclear cross section for low proton energies connected with the high cross section of the copper gamma lines at higher incident energies, make the natural Copper-BodiPy compound a simple and attractive solution.

Chapter 3

The Monte Carlo approach

One of the main focus of this thesis work has been to performed critical study dedicated to the improvement of the methods for the calculations of the fundamental parameters in protontherapy i.e. LET and RBE as a well as the realization of new devices to increase the quality of the protons and ions beams. All of these studies have been carried out by using the Geant4 Monte Carlo code. In this Chapter are described the main characteristics of the Monte Carlo algorithms. A section is entirely dedicated to the Geant4 method and its application in medical physics and radiobiological purposes.

3.1 The method

The Monte Carlo (MC) is a mathematical approach aiming to model nature through direct simulation of the essential dynamics of a given system. In the framework of physics processes studies, the Monte Carlo is used, for example, to model a macroscopic system through the simulation of its microscopic components. Based on the random numbers generation and belonging to the so-called family of statistic and not-parametric methods, the term Monte Carlo was coined in 1947, by the scientists J.Von Neumann and S. Ulam, at the starting age of

computers[101] [100]. They in fact, associated the intrinsic stochastic nature of the approach with the Monte Carlo city, being a roulette an almost perfect analogic random number generator.

In order to find a solution using the Monte Carlo three fundamental steps should be accomplished [103] [41]:

1. The generation of a sequence a random numbers and the determination of the input variable, depending on the chosen probability distribution;

2. The calculation of the output parameter;

3. The loop on previous points and comparison of the results in order to establish the minimum value of the associated variance.

The randomness of the generated numbers is a key requirement for the reliability of any Monte Carlo result. The number sequence generated by a calculator is defined to be pseudo-random because a pre-established relation between a sampled number and the previous one exists. The entire sequence depends on the first number of the chain which is called seed.
A huge list of simulation codes, based on a Monte Carlo approach, have been developed and adopted in many application fields. Many of these have been specifically developed and publicly distributed to permit the simulation of particles interaction and propagation inside matter. Table 3.2 shows some of the most widespread Monte Carlo codes, the particles they are able to handle and the programming language used for their development.

3.2 Simulations in medical physics

The history of the Monte Carlo method applied to the medical physics field is tied to the development of methods for the simulation of electron

Table 3.1: List of the most widespread Monte Carlo codes used for particle tracking

Code name	Particles handled	Language
ETRAN/ITS	Protons, Electrons	Fortran
PHITS	All paticles	Fortran
SHIELD-HIT	All particles	Fortran
MCNP	Protons, Electrons, Neutrons	Fortran
MCNPX	All particles	Fortran
EGS	Photons, Electrons	Fortran
PENELOPE	Photons, Electrons	Fortran
GEANT3	All particles	Fortran
GEANT4	All particles	C++
FLUKA	All particles	Fortran
PETRA	Protons, Electrons, Neutrons	C++

Table 3.2: List of the most widespread Monte Carlo codes used for particle tracking

transport in complex geometries and in the description of electromagnetic cascades. In the 1950, Robert Wilson published the first papers describing the Monte Carlo method in the electron transport [154].

The growth of the use of linear electron accelerators (LINACs) for radiotherapy also pushed-up the development of Monte Carlo methods for the dose calculation. Since that time, the deployment in Monte Carlo radiation transport algorithms has had an important impact in different areas of radiation dosimetry. For the experimental determination of absorbed dose, for example, several quantities are difficult to estimate accurately without numerical models. Radiation dosimetry detectors are in fact mostly constituted by several parts and different materials. In this context, Monte Carlo simulations can solve the problem related to the change in energy loss inside the materials [156]. Over the recent generations of radiation dosimetry protocols, progress in Monte Carlo techniques has permitted an improvement in accuracy in the determination of the absorbed dose. Nowadays, applications of the Monte Carlo method in medical physics span almost all topics, including radiation protection, diagnostic radiology, radiotherapy and nuclear medicine with an increasing interest in new applications such as nano-particles technique, BNCT, DNA damage and microdosimetry. Thanks to the rapid development of computational power, Monte Carlo based treatment planning for radiation treatment are becoming feasible, too [31] [68] [67].

3.3 The Geant4 simulation toolkit

Geant4 (GEometry ANd Tracking) [12] [7] is one of the most widely used Monte Carlo toolkits to study particles interaction and transport in the matter. It is currently used in a large number of experiments and projects and in a variety of application domains, including high

energy physics, astrophysics and space science, medical physics and radiation protection. The Geant4 diffusion is essentially due to its advanced functionalities in the geometrical description and to a wide and well-tested set of available physics models. The first product of the Geant *family* was released in 1974 at CERN (Geneva, CH) in order to simulate the interaction of high energy elementary particles with matter. It was limited to a restricted set of particles and simple detector geometry. In 1982 a new project started: its aim was to develop a completely new toolkit written in Fortran [23][11]: it was called Geant3 and discontinued at the end of the nineties, even if many researcher still use it. It allowed to simulate large experimental apparatus and the transport of high energy beams. The last member of the Geant4 family was born in 1998 when, after a first development phase, an Object Oriented, reusable and easy to maintain C++ toolkit was released. This new product was called Geant4. Geant4 is currently developed by an international collaboration, constituted by about one hundred members from Europe, US, Asia and Australia that release a new version of the code twice per year [2]. The public version of the Geant4 toolkit consists of a collection of C++ libraries containing all tools that the user has to include to develop his/her specific application. The object-oriented technology allows the easy and reusable development of distinct classes that can be used to simulate different aspects of a typical experiment: there are classes to construct the geometry, to define the materials, to model the source, the physics processes and so on. The public Geant4 distribution also contains a wide set of examples (divided in three main categories) representing the ideal users' starting point:

1. Basic examples: developed to illustrate the the basic functionalities of Geant4 toolkit;

2. Extended examples:focused on many specific capabilities and do-

mains on which Geant4 can be used;

3. Advanced examples: each describing a full experimental apparatus

Over the last years, the code evolved to address many requirements by a wide and growing community of Users and to encompass many physics applications and technological evolutions. The possibility to exploit the modern CPU multi threads has been, for example, recently introduced. Other different options for the future developments of Geant4 are also explored: GPUs [105] and accelerated processors offer, for example, great potentialities for speeding up intensive applications like those common in physics. Moreover, massively parallel computing and vectorization are being examined as a way to exploit available supercomputer capacity. In 2013 a new project was launched, named GeantV, to develop an all-particle transport simulation package with the broad objective of developing a tool based on Geant4 but several times faster to be used on CPU accelerators. A first alpha version of GeantV has been recently released [13].

3.3.1 Geant4 use in medical physics

Thanks to its great flexibility and precision in terms of physics models, geometry and transport parameters, Geant4 allows the Users to simulate complex three-dimensional geometries, possibly importing Computers Aided Design (CAD) and/or Digital Imaging and COmmunications in Medicine (DICOM) images, routinely used in the medical physics community [76]. Coupled with these advanced geometry capabilities, Geant4 offers several interesting features in terms of transport parameters, specifically introduced for dosimetric and micro/nano dosimetry studies. A particle can be transported until its kinetic energy goes down to approximately zero. Specific production thresholds

Table 3.3: List of medical physics examples released inside the Geant4 distribution

Advanced examples	Extended examples
Brachytherapy	Dicom
Cell_irrdiation	dna
Human_Phantom	FanoCavity_1
Medical_linac	FanoCavity_2
IORT_Therapy	ElectronScattering_1
Hadrontherapy	ElectronScattering_2
GammaKnife	GammaTherapy

Table 3.4: List of medical physics examples released inside the official Geant4 distribution

of secondary particles (protons, electrons, positrons, and gamma) can be defined in order to optimize the dose depositions and the overall simulation precision [64]. Several examples focused on medical applications are included in Geant4 distribution to guide the Users in the simulation of specific problems from the conventional radiotherapy to the Hadrontherapy and nuclear medicine applications (for diagnostic and therapy) and to the dosimetry at macro-, micro- and nano scale level. The medical physics examples in *Advanced* and *Extended* categories [24] [47] are listed in the Table 3.4.

Geant4 is currently able to simulate and model biological effects of ionizing radiation at the DNA scale [66]. A tool extension, named Geant4-DNA and included in the low-energy Electromagnetic (EM) package, contains discrete EM physics models applicable to electrons, protons, neutral Hydrogen ions, Helium ions and its charged states in liquid water (that are the main component of biological media)[65]. This package is able to simulate all interactions step-by-step in order to precisely reconstruct track structures of ionizing particles at nanometre

scale, thus allowing for a more precise understanding of damage at the DNA level [55] [88].

Chapter 4

Hadrontherapy: a based Monte Carlo tools for the hadrontherapy beam lines simulation

The studies on the protontherapy quality improvement were conducted in two steps; first, the simulation of each element of the beamline of interested was performed; then the new elements for the transport parameter optimization was designed, simulated and tested. All simulations were provided by using the Gean4 advanced example `Hadrontheray`. In this Chapter the main characteristics of this application as a well as the recent improvements to the code are described. In this context, new physics lists and the possibility to import an external phase space for the simulation of the particle source were inserted. The new transport element simulated, realized and tested for light ions beams was reported in the section 4.5.2 and 4.5.3. The new simulated TIFPA beamline, as well as the new elements simulated and installed, are in 4.6.

4.1 Introduction

Among the *Advanced Examples* released with the Geant4 distribution, `Hadrontherapy` is an application specifically developed for dosimetric and radiobiological studies with protons and ions beams [36] [37]. The application has been realized in the framework of a joint project between the INFN and the Geant4 collaboration. The main purpose of this project, started in 2003, was the development of an open source Monte Carlo application able to reproduce each element of the CATANA [38] beam line, the first Italian protontherapy facility dedicated to the treatment ocular melanomas. At the end of 2004, the first version of `Hadrontherapy` was released. Over the past several years, the application has been improved in order to get more flexibility and additional capabilities. Specific tools were added to permit the collection of information on the energy spectra of primary and secondary particles. The primary event generator has been optimized, with the introduction of a new approach based on phase space, allowing to run fast simulations also in the case of complex sources. `Hadrontherapy` also provides the possibility to activate physics lists via simple macro commands. Recently, a set of classes specifically devoted to the calculation of biological quantities: dose, averaged LET-dose, RBE, Survival Fraction and biological dose has been introduced [118]. A detailed description of the methods implemented in the code is reported in Chapter 5 and 6. The geometrical module of `Hadrontherapy` is divided in two main independent blocks, described by two different classes: a block is delegated the simulation of the beamlines geometry, the second is reserved to the simulation of the voxelized detector immersed in a water box. The detector is a specific volume (whose dimensions, position and material can be easily changed by macro commands) permitting the scoring of several quantities of interest such as deposited dose and

particle fluence. `Hadrontherapy` allows the simulation of three passive proton/ion beamlines, including all necessary transport elements: scattering and modulation systems for spatial and energy distribution beam definition, collimators, transmission detectors and detectors for dose distribution measurements. In particular `Hadrontherapy` allows the precise simulation of three INFN beam lines:

- CATANA proton therapy facility of INFN-LNS (Catania, I);
- Zero degree multidisciplinary facility of INFN-LNS (Catania, I);
- Multidisciplinary beam line of INFN-TIFPA (Trento, I)

In the following sections a detailed explanation of each main element of the application will be provided. The new improvements realized in the framework of my thesis work will be emphasised, as well.

4.2 Physics lists

Since the release 10.0, Geant4 provides nine reference *physics lists* (classes containing a complete set of physics models and dedicated to specific applications) [88] [155]. `Hadrontherapy` provides three custom physics lists suggested for medical physics applications (see Table 4.1).

The electromagnetic interactions are simulated using the `G4EmStandardPhysics_option4` builder, which implements a condensed-history algorithm based on the Beth-Bloch energy loss formula [109]. This physics constructor was designed for applications for which high accuracy of electrons, hadrons and ion tracking is required. It includes the most accurate standard and low-energy models and it is suggested for the simulations focused on medical physics application. Hadronic interactions are reproduced with models implemented in the

	HADRONTHERAPY_1	HADRONTHERAPY_2	HADRONTHERAPY_3
Electromagnetic	standard_opt4	standard_opt4	standard_opt4
	G4EmExstraPhysics	G4EmExstraPhysics	–
	–	–	G4EmLivermorePhysics
Hadronic	G4DecayPhysics	G4DecayPhysics	G4DecayPhysics
	G4RadioactiveDecayPhysics	G4RadioactiveDecayPhysics	–
	G4IonBinaryCascadePhysics	–	G4IonBinaryCascadePhysics
	G4HadronElasticPhysicsHP	G4HadronElasticPhysicsHP	G4HadronElasticPhysics
	G4StoppingPhysics	G4StoppingPhysics	G4StoppingPhysics
	G4HadronPhysicsQGSP_BIC_HP	G4HadronPhysicsQGSP_BIC_HP	G4HadronPhysicsQGSP_BIC
	G4NeutronTrackingCut	–	G4NeutronTrackingCut

Table 4.1: Summary of the physics lists available inside Hadrontherapy application

`QGSP_BIC` and `QGSP_BIC_HP` constructor, in which Geant4 native pre-equilibrium and de-excitation models are used as low energy stages of the Binary Cascade model for protons, neutrons and ions [14]. The builder `QGSP_BIC_HP` uses the addition data driven high precision neutron package (ParticleHP) to transport neutrons and light charged particle below 20 MeV down to thermal energies.

4.3 Primary Event Generator

The `Hadrontherapy` particle source module was planned to provide Users' with two choices: a standard random event primary generator and a phase space file, which contains data related to the events (position, direction of propagation, kinetic energy and particle type). The use of the phase space also allows to reduce the computing time without affecting the results accuracy. The phase space approach permits to divide the whole simulation into two steps. During the first step, the information of all particles hitting a scoring plane are recorded in a file from which they are recalled during the second step of the computation. This approach reduces the computing time considerably because the same primary data can be used in different simulations.

4.4 CATANA protontherapy facility of INFN-LNS

4.4.1 Set-up of the beamline

CATANA (Centro di AdroTerapia ed Applicazioni Nucleari Avanzate) was the first Italian protontherapy facility and in operation since 2002. The beamline is fully simulated inside the `Hadrontherapy` Geant4 application (Figure 4.1). A picture of the real beam line is displayed in Figure 4.2. Accelerated protons exit in air through a 50 μm Kapton win-

dow. Range shifters and range modulators are positioned downstream the scattering system. Two transmission monitor ionization chambers provide the on-line control of the dose delivered to the patient. In order to monitor the beam stability during the treatment, a micro strip ionisation chambers detector [51] is placed at the end of the beamline. The beamline ends with a final (50 cm long, 36 mm in diameter) brass collimator, defining the final emittance of the beam at patient location.

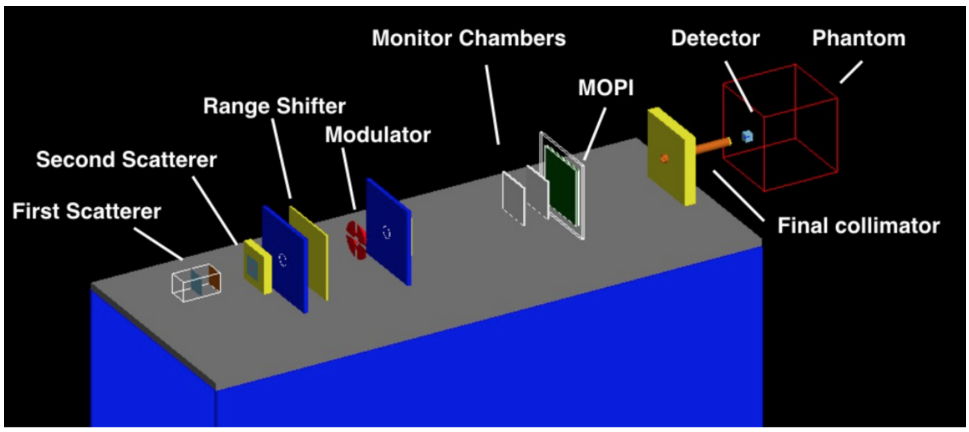

Figure 4.1: The CATANA beamline geometry implemented inside `Hadrontherapy` application

4.4.2 The scattering system

Lateral and energy beam spread is obtained in CATANA by interposing static systems (scattering foils, plastic modulator wheels) along the beam path. Different approaches can be adopted to spread the accelerated beam laterally. The simplest scattering system consists of a single scattering foil able to spread the beam into a Gaussian-like profile [53]. A collimator then fixes the beam dimensions. The scattering foil is generally made of high-Z materials (tantalum, gold, etc.) to obtain the maximum scattering minimising the energy losses (Figure 4.3).

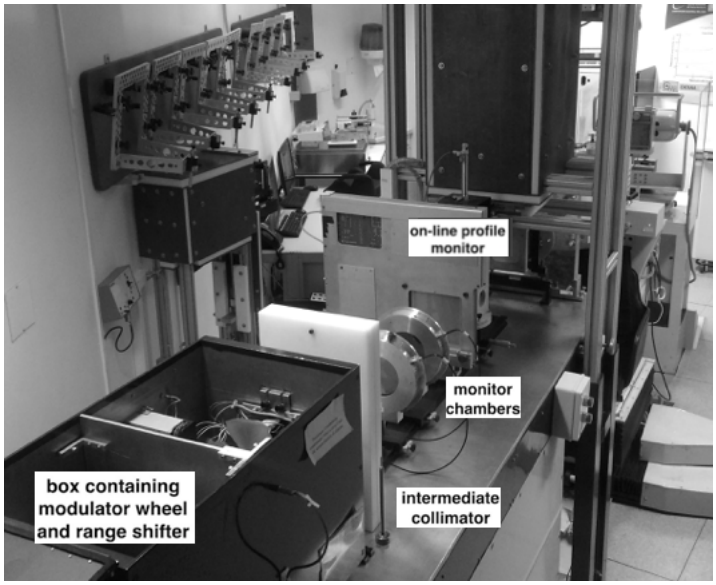

Figure 4.2: Picture of the transport section of the CATANA beamline

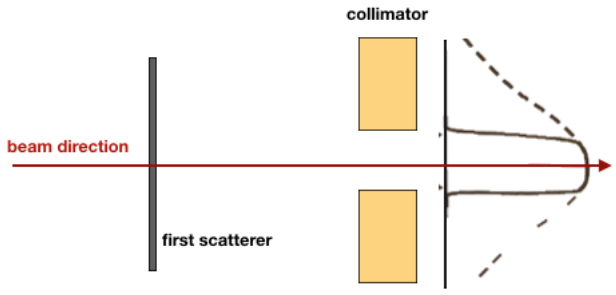

Figure 4.3: Scattering system scheme based on a singles scattering foil

The efficiency of this scattering system is very low: spreading is limited to small fields of the order of millimeters [141]. A better efficiency can be achieved by using a double-scattering system: the first scatterer spreads the beam that then reaches the second scatterer. By inserting an occluding central stopper between the two scatterer a wider uniformity in the lateral dose distribution can be easily achieved. A layout of a double-scattering system is reported in Figure 4.4.

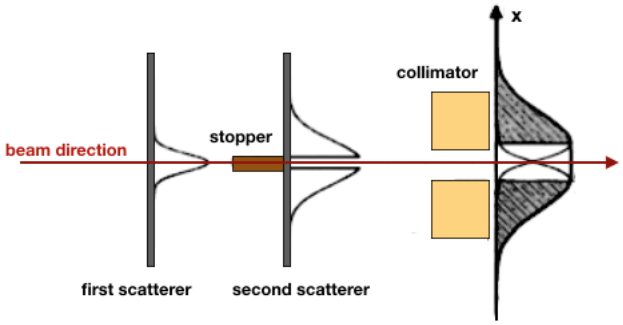

Figure 4.4: Scattering system layout based on a double scattering foil with a central stopper

The CATANA protontherapy facility [38] adopts such kind of system to obtain a lateral dose profile in accordance with the clinical ocular melanoma treatment prescriptions. Specifically, the double scattering system consists of two tantalum foils of 15 μm and 25 μm, respectively. The brass central stopper is 4 mm in diameter and 7 mm high. The first foil is located in the vacuum region of the beam transport line, about 20 cm upstream the in-air section, while the second is located in air, 15 cm beyond the 15 μm Kapton window separating the vacuum from the air section. The scattering system has been completely simulated and inserted into the `Hadrontherapy` application. The comparison of the experimental results and simulated data is reported in the Figure4.5.

4.4.3 Energy modulation system: modulator wheel

Energy modulation is achieved by means of PMMA modulator wheels. A modulator wheel is made of different steps of varying thickness able to reproduce pristine peaks of different energies to finally achieve a SOBP [106]. Using analytical calculations based on the power-law approximation of the proton stopping power, it is possible to describe the proton Bragg peaks and calculate the optimal weights for a SOBP

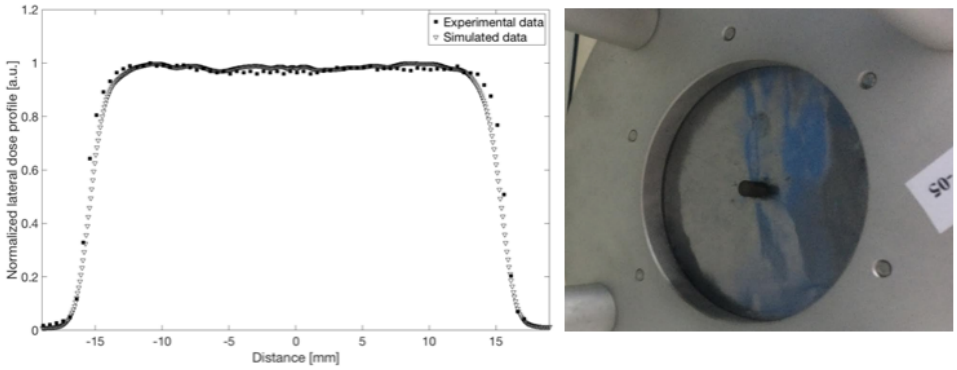

Figure 4.5: Left: experimental lateral dose profile distribution (circles) of a 62 MeV proton beam and the corresponding simulation dose (triangles). Right: second scatterer with its stopper of the system installed at the CATANA facility

[20]. The `Hadrontherapy` application provides a dedicated class for the simulation of the CATANA modulator wheels. Users can change the modulation region according to the different geometrical simulation of the available wheels. An example of the available SOBPs that can be reproduced in `Hadrontherapy` is reported in Figure 4.6.

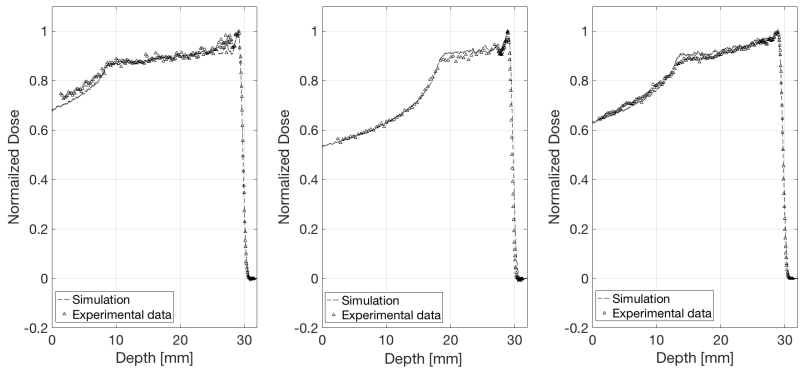

Figure 4.6: Experimental and simulated Spread Out Bragg Peak obtained by using three different modulator wheels

4.5 Zero Degree multidisciplinary facility of INFN-LNS

4.5.1 Set-up of the beamline

The Zero Degree (ZD) beamline is a passive beam line installed at LNS-INFN and entirely dedicated to in-air irradiation with ion beams ($Z > 1$, $E \leq 80 AMeV$). A sketch of the beam line geometry inserted inside the `Hadrontherapy` application is shown in Figure 4.7.

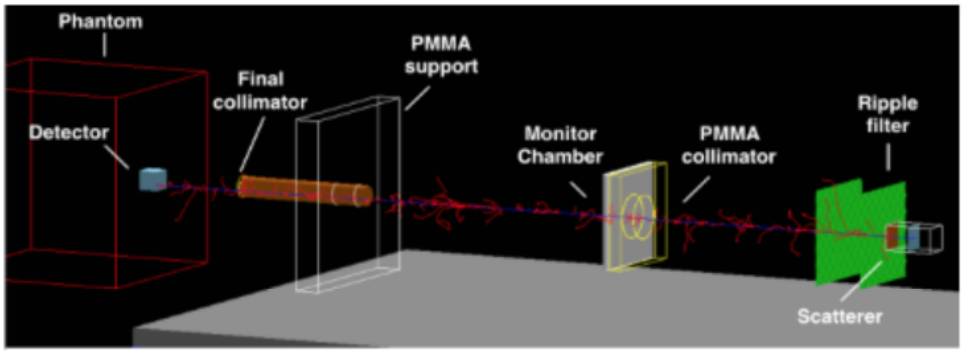

Figure 4.7: The ZD beamline geometry implemented inside `Hadrontherapy` application

Accelerated ions exit in air through a 50 μm Kapton window. The transported beam hit a scattering system composed by a tantalum foil with 20 μm in thickness and a brass central stopper. Two different systems for the beam modulation energy are available: a ripple filter specifically designed for 62 AMeV carbon ion beams and a ridge filter designed for 62 AMeV helium and oxygen ion beams. Both system are positioned downstream the scattering system. A transmission monitor ionization chambers provide the on-line control of the dose delivered. The final collimator system is composed of a brass tube (50 cm long and 27 mm in diameter) and a brass collimator with a variable in diameter from a maximum of 27 mm to 1 mm.

4.5.2 The scattering system

The passive scattering system installed at the ZD beamline is based on a double scattering foil with a central stopper. This solution is the result of a systematic study performed in order to identify the best configuration in term of profile width and flatness with three different transported ions species: ^{4}He, ^{16}O and ^{12}C. In the next section will be illustrated the results of a feasibility study conducted with the Geant4 code as well as the comparisons with the experimental data acquired by using the *Beam Profiler detector* described in the Chapter 8.

Double scattering foil with a central stopper

Most scattering systems for ions beams today are based to a dual ring scatterer, but an occluding cylinder with a second scatterer is an easy way to obtain a flatten the profile also. Because the particles are not distributed but blocked, the efficiency of an occluding system drops significantly. However, the energy loss is smaller though because a relatively thin second scatter foil is needed to spread out the beam. The investigated parameters were the energy loss, the fluency, and FWHM of the lateral dose distribution at the isocenter. First has been evaluated the effect due to a single foil placed in vacuum, then the contribution due to the second foil with a central stopper positioned at 10 cm of distance from the Kapton window. A profile obtained by using a single tantalum foil with a thickness of 15 μm has been chosen as reference value. In Table 4.2 and 4.3 the percentage difference of the parameters of interest as respect to the reference value are reported.

The FWHM of the lateral dose profile with the double foil and a central stopper of 6 mm in diameter is evidently larger than the one obtained with the other investigated configurations. A scatterer system composed of a single foil is less efficient as respect to a double system. In the case of ZD beamline, the thickness of the second foil has been fixed

Material	**Tantalum**					**Gold**	**Tungsten**
Thickness [μm]	20	25	30	40	50	15	15
diff. % Energy	0.37	0.40	0.70	1.20	1.21	0.10	0.22
diff. % Fluence	1.20	1.21	1.27	1.41	1.41	1.13	1.13
diff. % FWHM	8.04	8.08	8.15	9.10	9.10	7.39	7.40

Table 4.2: Percentage difference of the parameters of interest, i.e. Energy measured at isocenter position, incident particles fluence, FWHM of the lateral dose profile as respect to the parameters obtained with the reference configuration (single tantalum foil with a thickness of 15 μm)

Stopper diameter	**4mm**	**6mm**
diff. % Energy	2.07	2.09
diff. % Fluence	2.76	5.33
diff. % FWHM	9.85	10.38

Table 4.3: Percentage difference of the parameters of interest, i.e. Energy measured at isocenter position, incident particles fluence, FWHM of the lateral dose profile as respect to the parameters obtained with the reference configuration (single tantalum foil with a thickness of 15 μm and without a central stopper)

in accordance with technical needs. The stability of the central stopper could be compromised by using a too thin foil. This system has been tested during an experimental campaign performed with three different ions beams: ^4He, ^{16}O and ^{12}C. In all cases, a uniformity region with a width of the order of 1.5 cm, i.e. a region with a maximum variation of the 10% as respect to the beam axes, was obtained in both X and Y direction.

4.5.3 Energy modulation system

At the ZD beam line two energy modulation systems are installed: a ridge filter, designed for helium and oxygen beams and a ripple filter for carbon ion beams. In the next session the new ridge filter designed, simulated and realized as well as the characteristics of the ripple filter recently inserted inside the `Hadrontherapy` application, will be discussed in detail.

The Ridge Filter

The ridge filter consists in a 2D array of pins, whose shape and thickness can be optimized to obtain a SOBP with the desired characteristics. The functioning principle of the ridge filter is the same as the modulator wheel: the thickness of the ridge filter steps determines the peak positions and the width of the steps sets the weight of the peaks. Ions hitting the tip of the ridge will form the distal peak [106]. The thickness and width of the steps are optimized to provide a flat SOBP. The energy lost depends on the location where the ions hit the filter. Specifically, the developed ridge filter has been designed to obtain a uniform physical dose $D(x, y, z)$ region (SOBP) by superimposing several Bragg curves of different penetration depths with appropriate weights, which are calculated taking into account the parallel beam approximation [106]. This is the reason why the ridge filter is placed

upstream the scattering system: in this case, in fact, the beam can still be approximated parallel and the particles hit the ridge filter with a negligible divergence. The implementation method can be described mathematically as follows. The dose in the SOBP can be expressed as the superimposition of many Bragg curves expressed as:

$$D(x, y, z) = \sum_i w_i B_i(x, y, z) \tag{4.1}$$

where $B_i(x, y, z)$ is a Bragg curve that can be determined experimentally and analytically; w_i is the optimized weight determining the ridge shape, and accounting for the contribution of each peak i to the final SOBP [20] [8]. The weights can be obtained by the minimization of a cost function, Q, defined as

$$Q^2 = [D_p - D(x, y, z)]^2 \tag{4.2}$$

where D_p is the prescribed dose (taken constant to flatten the physical dose) and D(x,y,z) is the three-dimensional dose distribution of the Bragg curves, that are assumed to have a well-defined shape and lateral profile for each depth. The final dose distribution can be described by the product of the following three terms (assuming z is the beam direction):

$$B(x, y, z) = A(x, y, t_i) X d(z + \omega_{rf} t_i x F(t_i)) \tag{4.3}$$

here t_i is the thickness of the ridge filter material, which determines the range of Bragg curve, and ω_{rf} is the conversion factor of the thickness to the water equivalent thickness. The first term A is the lateral dose profile at the Bragg peak, d is the depth dose profile of the Bragg curve, which is obtained experimentally. It follows that each curve will be shifted by $\omega_{rf} t_i$. The last term F takes in account the nuclear interactions in the ridge filter material and water, and is calculated as the

difference of the ion fluence at the Bragg peak with and without the ridge filter material. In Figure 4.8 the developed ridge filter composed of 900 pins, each having a square base of 1.7 x 1.7 mm^2 and height of 4.72 mm is shown.

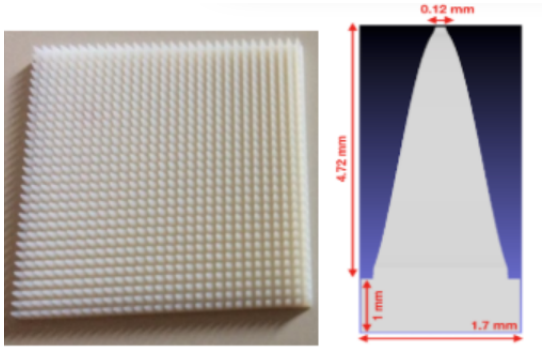

Figure 4.8: Left: Picture of the realised Ridge Filter; Right: scheme of a single pin

The material chosen for its realization was plastic (C21 O4 N24) with a density of 1.18 gr/cm^3. The development of a sophisticated geometry like a ridge filter requires both an accurate design, performed by using a Computer Aided Design (CAD) program, and simulation of performance under a realistic particle flux generally performed by using a Monte Carlo code. The above mentioned filter was designed and produced thanks to a collaboration between the INFN-LNS group and the GSI, Darmstadt (D) [1]. In order to reproduce correctly the geometry in Geant4 two different strategies has been adopted: the direct importing of the CAD model into the code and a reconstruction of the geometry by using a superimposing of native structures already presented in Geant4 kernel [150]. Transfer of the design from the CAD program to Geant4 has required several intermediate steps:

- the model of one single pin has been converted in the standard format STEP (STandard for the Exchange of Product model data);

- the generated STEP file has been converted into the Geometry Description Markup Language (GDML) format that is used by Geant4 for importing and exporting geometry models.

After this procedure, the single pin (see Figure 4.9) has been duplicated by using the G4Replica class to simulate the entire filter geometry.

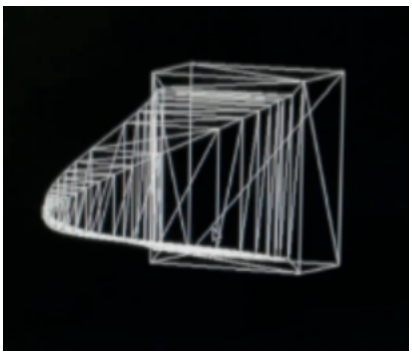

Figure 4.9: Single pin of the ridge filter geometry imported in Geant4

Such strategy, although extremely accurate, requires a huge computation time. For this reason, the second strategy, based on the superimposing of single elements with a trapezoid shape (created by using G4Trp function) was adopted in the final simulation. In Figure 4.10 and Figure 4.11 the simulated and experimental dose distributions a for ^{4}He and ^{16}O beam are shown.

The Ripple Filter

The Carbon Bragg peak is narrower than the proton on. Similar consideration applies also to the transverse dose distributions. In the Carbon ion beam case, a configuration with two ripple filters is the most suggest as reported in [22]. This is the solution that has been adopted at the ZD beam line: the first filter was positioned at 7 cm from the exit windows of the beam and the second one at 10 cm from the first.

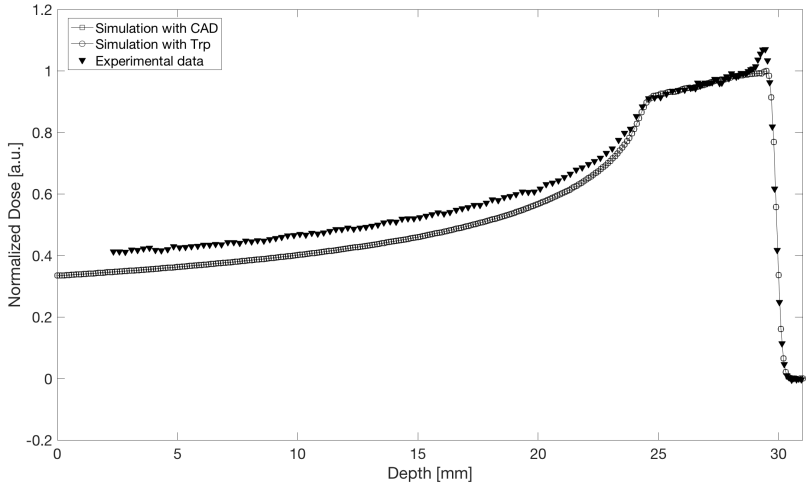

Figure 4.10: Experimental depth-dose distribution measured in water by using a ionization Markus chamber (Mod. 3002) and a spatial resolution of 10μm . The simulated dose distribution is also shown. The energy of the incident Helium ions beams was 62 AMeV

A section of a single pin as well as the entire geometry is reported in Figure 4.12

A single structure has a triangular section with a thin base of plexiglass (200 mm x 200 mm x 0.3 mm) and a basis 3 mm in thickness. The material density is 1.19 g/cm^3. Also in this case the geometry has been simulated by an overlap of trapezoid shapes. In Figure 4.13 the comparison between the simulated and experimental depth dose is shown. These filters was realized thanks to a collaboration between the INFN-LNS and INFN-TO groups.

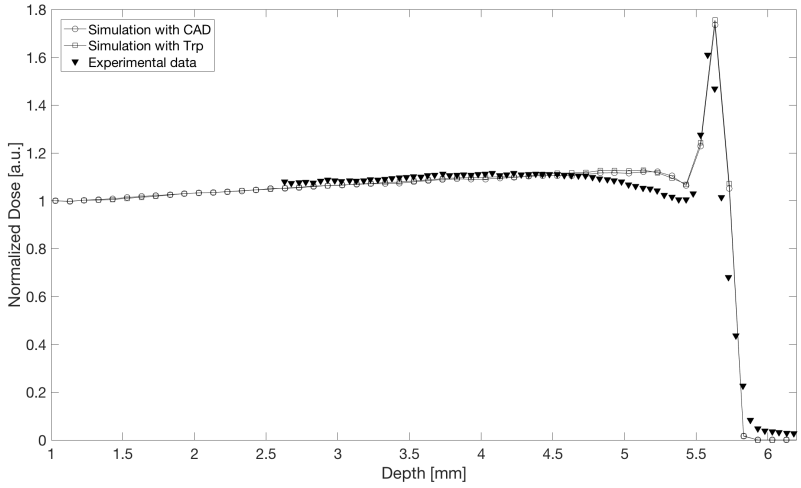

Figure 4.11: Experimental depth-dose distribution measured by using a ionization Markus chamber (Mod. 3002) placed in a water phantom with a spatial resolution of 10um . The simulated dose distribution is also shown. The energy of the incident Oxygen ions beams was 62 AMeV.

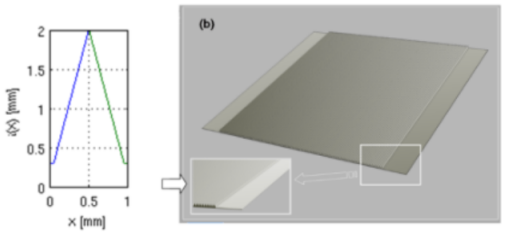

Figure 4.12: a) Section of single ripple filter structure b) Entire geometry of the ripple filter

4.6 Multidisciplinary beamline of INFN-TIFPA

4.6.1 Set-up of the beamline

A proton beam in the energy range between 70 and 228 MeV is available at the Trento proton therapy centre. Beam intensity can be adjusted in

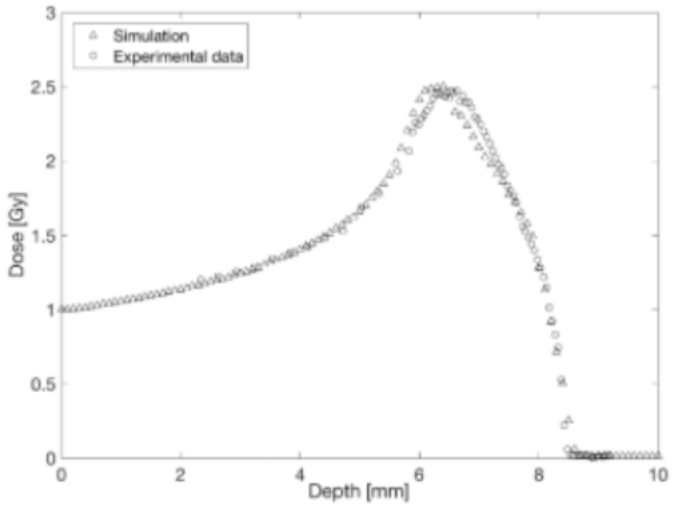

Figure 4.13: Experimental and simulated depth-dose distribution with 62 MeV incident carbon ion beams

the range 1-300 nA. The beam is accelerated to the maximum energy by a cyclotron (Proteus Plus, IBA, Belgium), followed by an Energy Selection System (ESS) allowing the transport of any energy in the range 70-228 MeV either to the treatment gantries or to the experimental room [145]. A sketch of the in-air beam line geometry scheme is shown in Figure 4.14.

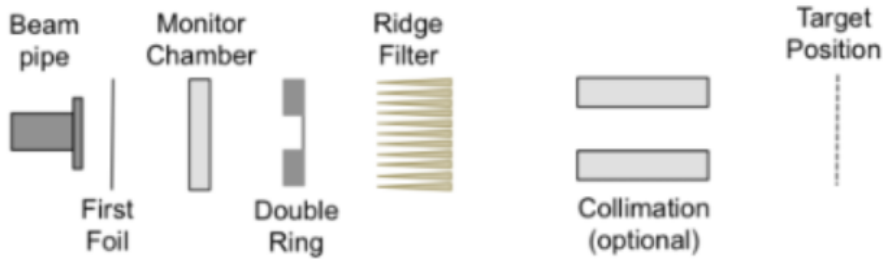

Figure 4.14: Sketch of the TIFPA beam line

Accelerated ions exit in air and hit a scattering system composed by

a scattering foil coupled to a double ring system. A monitor chamber performs an on-line check of the beam characteristics (in terms of shape and intensity). Then, a ridge filter modules the beam in energy. After 150 cm two collimator are applied in order to cut the radiation field laterally and produce a sharp profile.

4.6.2 The scattering system

The passive scattering system implemented in the facility is based on the double-ring design proposed by Takada [141]. The system is composed by a first scattering foil of high atomic number, producing a first enlargement of the beam, followed by a second scattering element characterized by two regions of different scattering power but same water-equivalent thickness (i.e. the dual ring). The different elements (material composition, thickness and lateral dimension) can be optimized in order to obtain a flat profile at target position. During this work it was decided to design two scattering systems for a 148 MeV proton beam, which is a typical energy used in proton therapy. The distance between the first foil and the double-ring, and from the beam exit window to the target position, were then fixed at 0.5 and 2 meters, respectively. Details on the scattering elements for the two set-ups (small and big ring) are reported in Table 4.4.

The 2D beam spot measured at target position for the small and large ring set-up are shown in Figures 4.15 and 4.16, respectively. X-Y profiles extracted at the spot centre are also presented.

In the case of small ring, an uniformity of 98.4% and 98.1% was obtained in X and Y direction, respectively in the central region (± 3 cm) of the spot size. For the large ring set-up, the uniformity was evaluated in a larger region (± 8 cm) resulting into 97.4% and 96.5% in X and Y direction, respectively. This slightly lower uniformity is due to the "wave effect" observed in the beam profile. This is due to

Setup	First Foil		Inner Ring			Outer Ring	
	Material	Thickness	Material	Thickness	Diameter	Material	Thickness
Small Ring	Pb	0.8 mm	Pb	1.5 mm	11 mm	Al	5 mm
Big Ring	Pb	3.4 mm	Pb	5.5 mm	22.5 mm	Al	16 mm

Table 4.4: Characteristics (size and material) of scattering elements for the small and large set-up.

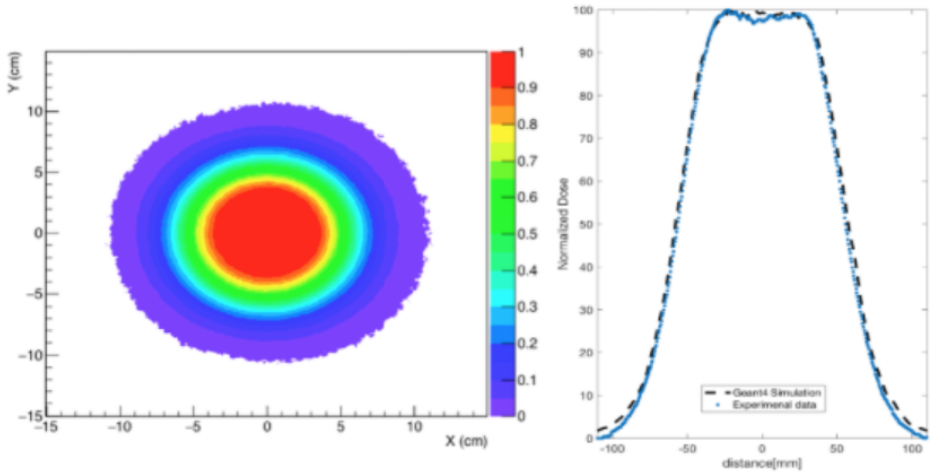

Figure 4.15: The 2D intensity map obtained for the Small Ring with Lynx detector (left) and corresponding X-Y profile extracted at the centre of the field (right). The experimental data are plotted together with the corresponding Geant4 simulations

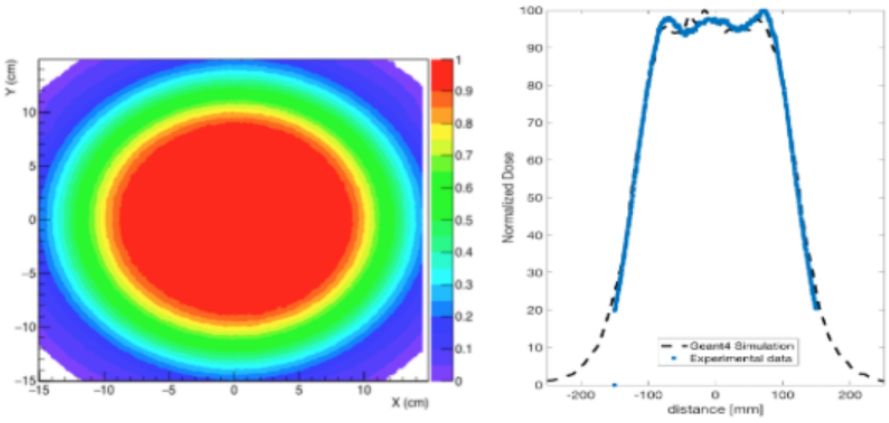

Figure 4.16: The 2D intensity map obtained for the Small Ring with Lynx detector (left) and corresponding X-Y profile extracted at the centre of the field (right). The experimental data are plotted together with the corresponding Geant4 simulations

the mixing of the beam components scattered by the inner and outer ring, this effect being more pronounced in larger fields. In any case,

uniformity well above the requested 90% was obtained with both set-up.

4.6.3 Energy modulation system

In order to produce the Spread Out Bragg peak, a ridge filter has been installed. The ridge filter was designed and constructed for the 148 MeV energy to produce 2.5 cm of SOBP. It consists of 961 pins, each having a basis of 2.5 x 2.5 mm^2. Figure 4.17 illustrates the ridge filter used in the beam line, which was designed and produced by GSI, Darmstadt.

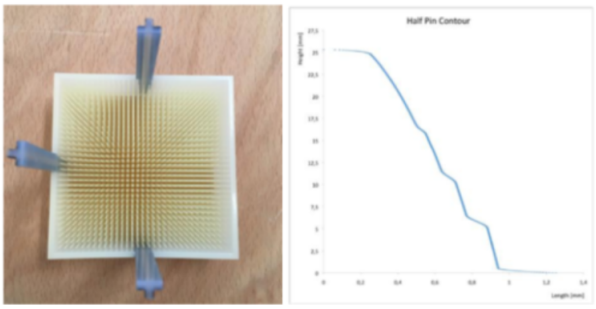

(a) Photo of the ridge filter produced by GSI, Darmstadt

(b) Lateral profile of each pin

Figure 4.17: Details of the ridge filter adopted in our setup, producing a modulation of 2.5 cm.

This ridge-filter was manufactured using the 3D-printing technique. The material used is under patent, thus only partial information are available, as the chemical formula. In order to implement the material, the density was needed and had to be adjusted by running several simulations up to a value of $\rho = 1.40$ cm^3, which resulted in the best fit with experimental data. The single pins were built in the simulations by combining several trapezoid elementary volumes. The good agreement between experiments and simulations is illustrated in the Figure 4.18

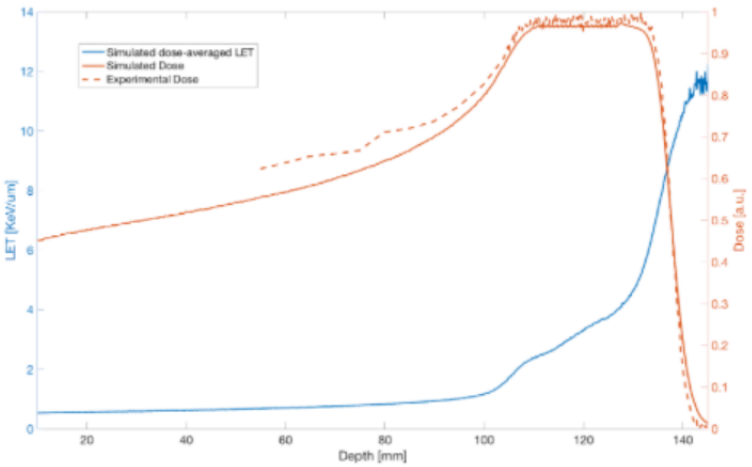

Figure 4.18: Experimental depth-dose distribution measured in water by using a ionization chamber CC01 (IBA-dosimetry) [3]. The simulated dose distribution as well as the averaged dose LET distribution is also shown.

Chapter 5

Linear Energy Transfer in radiation therapy

5.1 Microdosimetry

The interaction of ionizing radiations with biological systems induces many different effects (cell killing, mutation, chromosome aberration, etc.) correlated to the mechanisms of local energy deposition. The physical descriptions of these microscopic patterns establish the field of *microdosimetry*. Since 1967 the term *microdosimetry* was used, to describe the dependence of biological outcomes on the spatial distributions of the physical events [71]. At present, biological outcomes considerations in conventional photon radiotherapy, are only derived from the macroscopic measure of physical dose distribution in patient. However, different are the cases of radiotherapy with protons/ions, characterised by high energy deposition event. In these cases fluctuations at the cellular level may be of practical importance to estimate the biological effect. An example of the simulated patterns energy deposition along their track for photons, helium and oxygen ions incident in a medium [143] is reported in Figure 5.1.

The main physical quantity describing the radiation quality and,

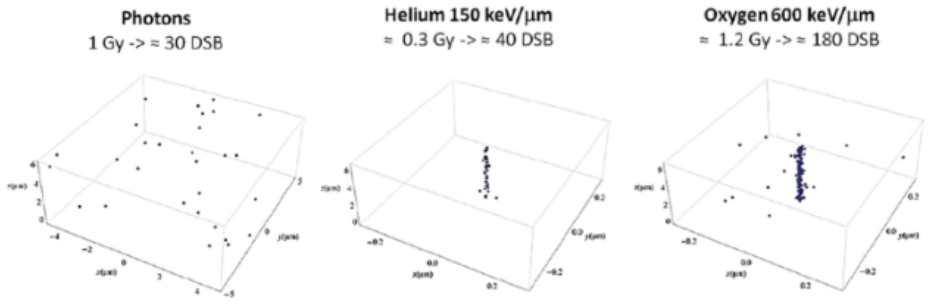

Figure 5.1: Simulated patterns of biological damage expressed in term of DSB (Double Strand Break) distribution after photon and ion irradiation in a typical cell nucleus (radius of ~ 5 μ m). Photons shown a sparsely ionizing radiation (and consequently a sparsely distribution of lesions). Low energy α particles and oxygen ions shows that considerable dose is released in the cell nucleus after a single particle traversal; anm high dose is released close to the particle track, resulting in the induction of an increased number of close-by DSB (densely ionizing radiation).

consequently, the local energy deposition is the so-called, Linear Energy Transfer or LET [71]. This concept has been introduced by Zirkle et al. in 1952 [159]. Since the 1950s many strategies to estimate this quantity with the highest possible precision was adopted. Micro- and nano- dosimeter detectors, as well as new algorithms, were developed to this scope. In this framework, Monte Carlo simulations have revealed to be the better method to simulate the components of a clinical beam and to estimate accordlingly the LET also in a biological enviroment.

Nowadays, more than one Monte Carlo based algorithms are known. The scope of this thesis has been to identify the best algorithm to calculate the LET by using the Geant4 Monte Carlo code. A comparison between known algorithms was performed and new strategies were proposed to obtain the highest precision with the lowest possible dependence from the main Monte Carlo parameters like voxel size and

secondaries production cut threshold.

5.2 Rigorous definition of LET

The LET or restricted linear collision stopping power (L_Δ) [4] is a measure of the average ionization density of a charged particle along its path direction. It's closely related to the concepts of mean linear ion density [52] and to the more common stopping power definition. Following the ICRU definition, the LET of a charged particle in a medium is the ratio between the mean energy dE loss by a charged particle and the distance dl where this loss happens in a distance dl and considering only the collisions where an energy less than a threshold Δ is transferred:

$$L_\Delta = (dE/dl)_\Delta \tag{5.1}$$

If no energy cut-off is imposed, L_Δ is called *unrestricted* or L_∞ and it is equal to the electronic stopping power, S_{el}, which analytically describes the energy loss per unit of length travelled by charged particles with no care to the secondary electrons set in motions. The unrestricted collision stopping power L_∞ may be determined from experimental measurements of deposited energy in a micro-dosimeter detector with an active area of the order of micro/nano-meter scale. However, the accuracy of the this method is limited by the production and escape of delta rays from the detector.
When the studied beam is composed by many different energetic components, as in the clinical practice, the calculation, even of L_∞, shows additional complexities [152]. A real beam is usually composed of particles of different atomic and charge numbers and different velocities: it hence contains a distribution of LETs. It is more convenient, for these cases, to introduce the concept of an average LET distributions, representing the average of the energy losses and of the track lengths

of charged particle into a specific spatial region. In literature such distributions are referred as track average LET ($\bar{L}_T$) or as absorbed dose average LET ($\bar{L}_D$) [71]. They defined as:

$$\bar{L}_T = \frac{\int_0^\infty L \cdot f(L)dL}{\int_0^\infty f(L)dL} \tag{5.2}$$

$$\bar{L}_D = \frac{\int_0^\infty L^2 \cdot f(L)dL}{\int_0^\infty L \cdot f(L)dL} \tag{5.3}$$

Here $f(L)$ is the frequency with which a particle if found with LET between L and $L + dL$. The track averaged $\bar{L}_T$ assumes that each unit of track length has equal statistical weight. It is the expectation value of L. The absorbed dose average $\bar{L}_D$ weights each unit of track length in proportion to the transferred energy.

The $\bar{L}_T$ and $\bar{L}_D$ definitions can be extended to take into account also the contribution of secondaries produced in the hadronic inelastic interaction of primary beam with the target materials. Such an extension brings to the definition of the following quantities:

$$\bar{L}_T^{Total} = \frac{\sum_{j=1}^N \int_0^\infty L_j \cdot f_j(L)dL}{\int_0^\infty f_j(L)dL} \tag{5.4}$$

$$\bar{L}_D^{Total} = \frac{\sum_{j=1}^N \int_0^\infty L_j^2 \cdot f_j(L)dL}{\int_0^\infty L_j \cdot f_j(L)dL} \tag{5.5}$$

Where the sum on j represents the contributes related of each particles, secondary and primary.

5.3 LET calculation via Monte Carlo approach

A number of Monte Carlo *track structure* codes have been developed to simulate individual radiation tracks. In such codes, every interaction

of both primary ion and its secondaries could be simulated sequentially by random selection from distribution of the interaction cross sections. This technique has enormous potential and is now being widely applied. MC simulations offer a simple solution to obtain local energy spectra in a given geometry making use of the information retrieved step-by-step along particles track. In this work it's proposed and discussed algorithms for $\bar{L}_D$ and $\bar{L}_T$ able to eliminate the present dependence on simulation transport parameters, like the voxel size, the production cut of secondaries and the step maximum length. These parameters are intrinsic to any condensed-history Monte Carlo simulation tool and have an impact in clinical practice. In the next section will be discussed three different methods for the $\bar{L}_D$ calculation and two for $\bar{L}_T$. The main conclusion of this work is that one of the proposed new algorithms gave the most consistent performance among the compared methods. This new algorithm has been implemented inside the official Geant4 example `Hadrontherapy`.

5.3.1 Absorbed dose average LET (LD)

Method 1

This method, proposed by Cortes et al. [42] shown a very low dependence from transport parameters. The developed calculation to compute the $\bar{L}_D$ is the following: if N is the total number of all steps performed by a primary particles inside a voxel, the equation 5.3 can be written as:

$$\bar{L}_D = \frac{\frac{(\sum_{i=1}^{N} \varepsilon_i)^2}{\sum_{i=1}^{N} l_i}}{\sum_{i=1}^{N} \varepsilon_i} \tag{5.6}$$

where l_i and ε_i are, respectively, the step length and the electronic energy loss of the primary particles. Analogously, this approach [42] has been extended for the calculation of $\bar{L}_D^{Total}$. This one, can be easily

retrieved if in the term i the energies loss by primary particles and all produced secondary ions j produced, are included. In this case, the $\bar{L}_D^{Total}$, in accordance to equation 5.5, can be written as:

$$\bar{L}_D^{Total} = \frac{\sum_{j=1}^{n}\left[\frac{(\sum_{i=1}^{N}\varepsilon_i)^2}{\sum_{i=1}^{N} l_i}\right]}{\sum_{j=1}^{n}\left[\sum_{i=1}^{N}\varepsilon_i\right]} \tag{5.7}$$

Method 2

A variation of Equation 5.2 was also implemented as the second method for the calculation of absorber dose average LET. Instead of computing the LET as the quotient between the actual electronic energy loss and step length computed during the simulation, the LET of the step, L_i, was calculated as the corresponding mean energy loss per unit path length in the material according to the proton kinetic energy at the step. In the new developed algorithm, this parameter, called L_i, was obtained with the method `ComputeElectronicDEDX()` of `G4EmCalculator` class. This function can be applied at each step and calculates the LET from electronic stopping power tables built at the beginning of the simulation, once particle type, kinetic energy and material are provided. The kinetic energy was the arithmetic mean between the values at pre- and post-step points. Further, L_i was calculated for steps terminated only by an electromagnetic interaction (such as $\delta - ray$ production by ionization) or a boundary crossing, since other kinds of interactions (e.g., inelastic hadronic) may completely lose the identity of the track. Thus, the average of L_i weighted by the electronic energy loss (ε_i) computed at that step yields:

$$\bar{L}_D = \frac{\sum_{i=1}^{N} L_i\varepsilon_i}{\sum_{i=1}^{N}} \tag{5.8}$$

Taking into account the contribution due to the produced secondary

particles the equation 5.8 becomes:

$$\bar{L}_D^{Total} = \frac{\sum_{j=1}^{n}[\sum_{i=1}^{N} L_i \varepsilon_i]_j}{\sum_{j=1}^{n}[\sum_{i=1}^{N} \varepsilon_i]_j} \tag{5.9}$$

Method 3

In this third approach the final average LET is computed in an easier way. At a specific depth (or voxel), LET is averaged step-by-step without explicitly separating the contributions due to different isotopes. Energy deposited along the step i is divided by the particle step length l_i and the stopping power calculated for the specific step is weighted by the released energy in the step:

$$\bar{L}_D = \frac{\sum_{i=1}^{N} \frac{\varepsilon_i^2}{l_i}}{\sum_{i=1}^{N} \varepsilon_i} \tag{5.10}$$

where $i = 1, ..., N$ represents the steps done by primary particles in a fixed slab. This method was implemented in a previous version of the `Hadrontherapy` advanced example and shown a not negligible dependence to the cut parameter. Such implementation can be also extended to the secondary particles contribute:

$$\bar{L}_D^{Total} = \frac{\sum_{j=1}^{n}[\sum_{i=1}^{N} \frac{\varepsilon_i^2}{l_i}]_j}{\sum_{j=1}^{n}[\sum_{i=1}^{N} \varepsilon_i]_j} \tag{5.11}$$

where the index j is referred to each ion scored in a voxel.

5.3.2 Track average LET (LT)

Method 1

Accordingly to the definition 5.2 MC permits the calculation of the ratio between the total energy depositions and total track lengths from

all primary charged particles, as reported in [54]:

$$\bar{L}_T = \frac{\sum_{i=1}^{N}(\frac{\varepsilon_i}{l_i})l_i}{\sum_{i=1}^{N} l_i} = \frac{\sum_{i=1}^{N}\varepsilon_i}{\sum_{i=1}^{N} l_i} \tag{5.12}$$

where ε_i is the energy loss for the nuclear and electromagnetic interaction l_i is the track length and N the total of the steps related to charged primary particles within a specific voxel volume. In the present study, the LET track calculation, developed just for the primary particle, was extended to include the whole spectrum of secondaries produced by the primary beam:

$$\bar{L}_T = \frac{\sum_{j=1}^{n}[\sum_{i=1}^{N}(\frac{\varepsilon_i}{l_i})l_i]_j}{\sum_{j=1}^{n}[\sum_{i=1}^{N} l_i]_j} \tag{5.13}$$

where $j = 1, ..., N$ is referred to a specific particle type inside the voxel.

Method 2

The second approach consists on compute the track average LET by using the method `ComputeElectronicDEDX()` of `G4EmCalculator` class according to the formula 5.11 and 5.12. The average of L_i is weighted by the track length of the charged primary particle (l_i):

$$\bar{L}_T = \frac{\sum_{i=1}^{N} L_i l_i}{\sum_{i=1}^{N} l_i} \tag{5.14}$$

Taken into account the contribution due to the produced secondary particles the formula 5.11 becomes:

$$\bar{L}_T^{Total} = \frac{\sum_{j=1}^{n}[\sum_{i=1}^{N} L_i l_i]_j}{\sum_{j=1}^{n}[\sum_{i=1}^{N} l_i]_j} \tag{5.15}$$

5.3.3 LET dependence on production cuts: a systematic study

Production cuts for the generation of secondaries is a crucial parameter in any MC simulation. It strongly affects, in fact, the energy deposition especially when small volumes are considered. In Geant4 the production cut is a distance (expressed in unit of length) and the secondary particles (electrons, positrons, gammas and secondary protons) are tracked only if their expected range in that medium is larger than the imposed cut. Otherwise, secondaries are not tracked and their kinetic energy is deposited in the secondaries production position. In Figure 5.2 a schematic representation of the effect due to a different cut value when a particle traverses a slices on the secondary particles tracking is reported.

If the definition of Section XX is followed According to the definition reported in the Section 5.2, the correct tracking of delta rays can influence the computation of the LET. If the secondary particles are neglected or incorrectly tracked the LET could be underestimated or overestimated if cut values are longer or shorter than the voxel size, respectively

The simulation set-up

All calculations were carried out adopting 10.03.p02 Geant4 version and using the official advanced example `Hadrontherapy`. The chosen reference physics list was HADRONTHERAPY1. The simulated beam spot was assumed circular, with a Gaussian fluence distribution and a sigma of 0.5 mm. The initial energy distribution is assumed Gaussian, as well, centred at the nominal energy of 62.45 MeV/n and with a sigma of 0.25 MeV. A small angular divergence of 0.028 degree was also introduced. A total of 10^7 particle histories were considered in each simulation run. Finally, the dose and LET values were scored

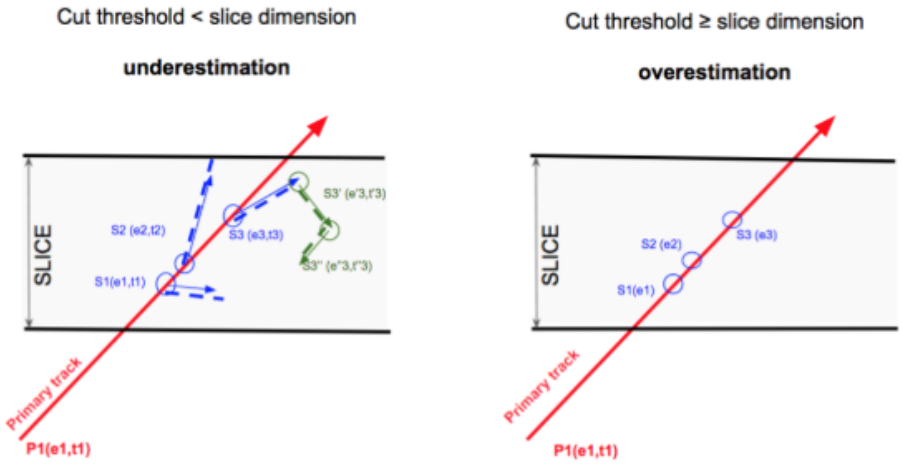

Figure 5.2: Case 1 (left): the fixed cut value is shorter than the slice dimension. In this case, the secondary particles (in blue and in green) produced by the primary one (in red) are tracked. Case 2 (left): the fixed cut value is equal or major than the slice dimension. The secondary particles are not tracked and the energy is considered all deposited at the exact point where are produced.

in a water phantom divided into slabs of 100 μm in thickness. For the tracking of secondary particles (electrons, positrons and secondary protons), the production cut value was varied between 0.01 and 1 mm.

The cut dependence by using the Method 1

A study of primary-LET distribution curves ($\bar{L}_D$, $\bar{L}_T$), calculated with the formulas 5.6 and 5.12, as a function of production cuts values, has been carried out. Primary $\bar{L}_D$ and $\bar{L}_T$ distributions, calculated for proton by using three different cut values are plotted in Figure 5.3. The analysis has been conducted in three positions along the Bragg peak, corresponding to the depths for which the absorbed dose is 15% and 50% of maximum (points P1, P2 and P3 of Figure 5.3).

The production cuts and the corresponding $\bar{L}_D$, $\bar{L}_T$, $\bar{L}_D^{Total}$ and

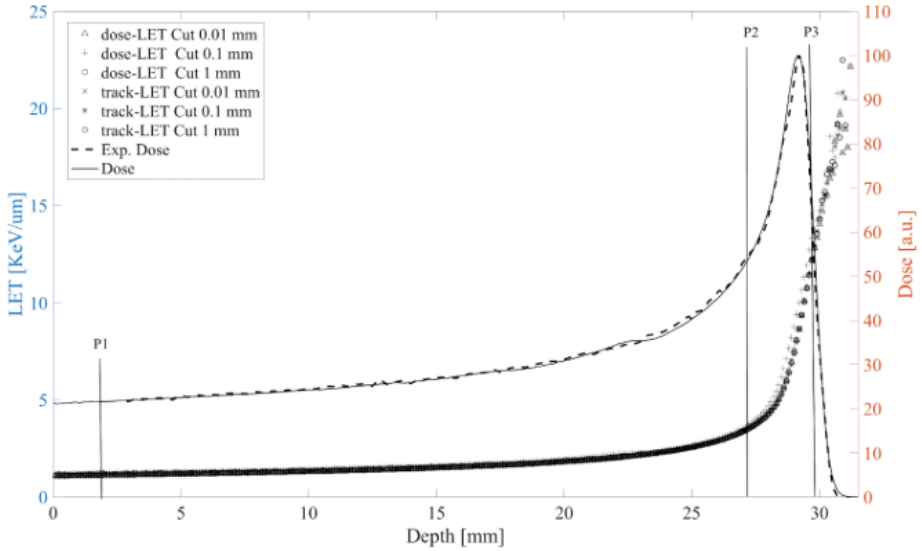

Figure 5.3: $\bar{L}_D$ and $\bar{L}_T$ distributions for 60 MeV proton beams calculated using formulas 5.6 and 5.12 for production cuts from 0.1 mm to 1 mm

$\bar{L}_T^{Total}$ values for each studied positions, are reported in Table 5.1.

LET curves have shown a very low dependence from the production cuts in almost all cases. Except for the calculation of total dose LET, where discrepancies up to 20% were observed, while in all other cases differences are always below 3%. The big instabilities observed in the case of proton $\bar{L}_T^{Total}$ are correlated to the influence of the few low-energy, high-let secondaries produced by protons-water interaction and releasing a relative big energy as respect the incident protons. Biggest differences, in fact, occur in the entrance zone (P1), where the energy deposited by proton is the smallest.

The cut dependence by using the Method 2

The influence on LET calculation results of different cut values has been researched carefully with the *Method 2*, according to the equation 5.8 -

Proton beam									
Position	**Cut [mm]**	$\mathbf{L}_D$ **[keV/μ]**	**diff% $\mathbf{L}_D$**	$\mathbf{L}_T$ **[keV/μ]**	**diff% $\mathbf{L}_T$**	L_D^{TOT} **[keV/μ]**	**diff% L_D^{TOT}**	L_T^{TOT} **[keV/μ]**	**diff% L_T^{TOT}**
P1	0.01	1.09	0.91	1.09	0.91	4.42	20.4	2.22	7.50
	0.1	1.09		1.10		4.78		2.24	
	1	1.10		1.10		3.84		2.40	
P2	0.01	3.26	2.69	3.32	2.99	3.63	3.46	3.14	2.85
	0.1	3.33		3.24		3.66		3.06	
	1	3.35		3.34		3.76		3.15	
P3	0.01	19.34	2.56	13.34	2.56	18.22	7.03	13.10	5.62
	0.1	19.69		13.69		19.22		13.70	
	1	19.57		13.53		19.02		12.76	

Table 5.1: For proton beam in water are reported the values of: $\bar{L}_D$, $\bar{L}_T$, $\bar{L}_D^{Total}$ and $\bar{L}_T^{Total}$ for the three positions studied (P1, P2 and P3). On the fourth, sixth, eighth and tenth column is reported the percentage difference between the$\bar{L}_D$, $\bar{L}_T$, $\bar{L}_D^{Total}$ and $\bar{L}_T^{Total}$ values calculated by using three different cut values: 0.01, 0.1 and 1.

5.9 for the $\bar{L}_D$ and 5.14 - 5.15 for the $\bar{L}_T$ calculation. The $\bar{L}_D$ and $\bar{L}_T$ distributions of primary particles, calculated only for proton beam in water and for three different cut values are plotted in Figure 5.4. The analysis has been carried out in three positions along the Bragg peak, as mentioned above.

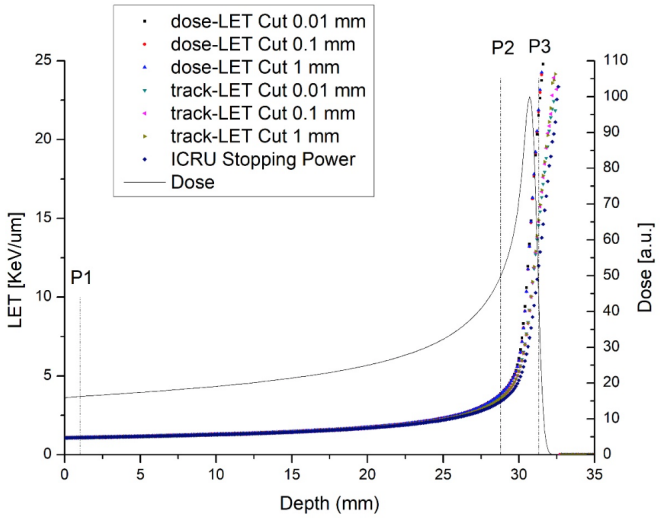

Figure 5.4: LD and LT distributions for 60 MeV proton beams calculated using formulas (9) and (10) for production cuts from 0.01 mm to 1 mm.

Compared with the *Method 1*, the independence between LET results and production cuts is more obvious when employing the *Method 2*. The LET calculation performed in the same three positions P1, P2 and P3 along the Bragg peak is shown in Table 5.2.

In this case, the higher discrepancy observed is the order of 15% for proton total dose LET calculation. While, for all other cases, the differences are below 2%. $\bar{L}_T$ and $\bar{L}_D$ distributions, based on the discussed algorithms, have been also compared for proton and oxygen beam with the same incident energy in water, i.e. 62 MeV/n. The Figures 5.5 and 5.6 show the LET calculated with *Method 1* and *Method 2*. The com-

Proton beam									
Position	**Cut [mm]**	$\bar{L}_D$ **[keV/μ]**	**diff% L$_D$**	$\bar{L}_T$ **[keV/μ]**	**diff% L$_T$**	$\bar{L}_D^{TOT}$ **[keV/μ]**	**diff%** $\bar{L}_D^{TOT}$	$\bar{L}_T^{TOT}$ **[keV/μ]**	**diff%** $\bar{L}_T^{TOT}$
P1	0.01	1.09	0.91	1.09	0.01	4.40	15.44	1.11	0.90
	0.1	1.09		1.09		4.79		1.11	
	1	1.10		1.09		4.05		1.10	
P2	0.01	3.70	0.27	3.46	0.29	4.43	1.81	3.48	0.29
	0.1	3.69		3.45		4.35		3.47	
	1	3.69		3.45		4.40		3.47	
P3	0.01	19.01	1.04	12.73	1.39	19.04	1.14	12.73	1.39
	0.1	19.15		12.86		19.18		12.86	
	1	19.21		12.91		19.26		12.91	

Table 5.2: Corresponding LET values for each of the studied positions (P1, P2 and P3) for proton beams with production cuts from 0.01 mm to 1 mm

parison between experimental and simulated depth dose distributions is also shown.

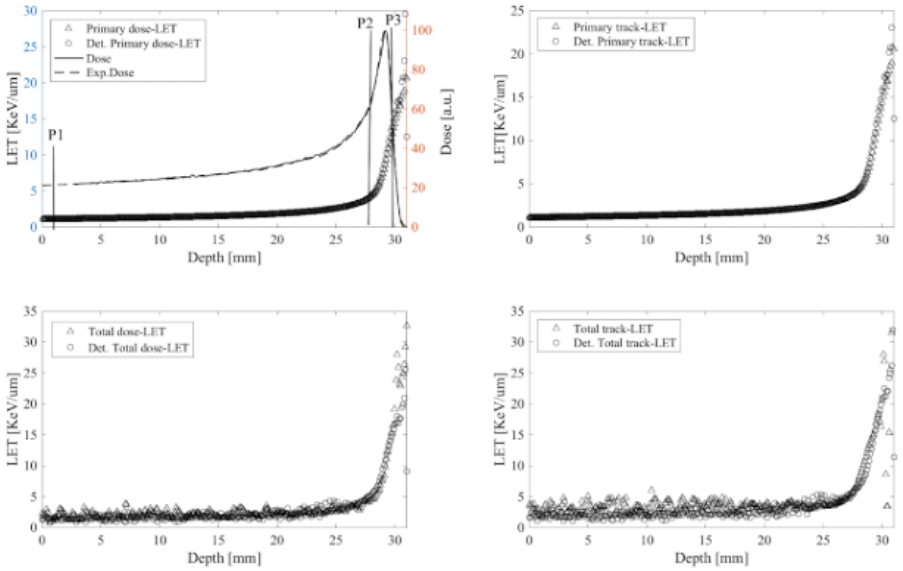

Figure 5.5: 62 MeV proton beams LET distributions calculated in water with the deterministic and MC method. Relative dose distributions, normalised at the peak entrance, (experimental and simulated) are expressed in arbitrary units. (a) Total and primary dose-LET distributions (b) Total and primary track -LET distribution

The maximum discrepancy is achieved at the entrance position of the total LET curve, i.e. 6%. The other position s shows a difference of the order of 1% for both cases total and primary LET. It is evident that the *Method 2* is more stable compared to the *Method 1*. The statistical fluctuation due to the energy deposition are less evident by using the *Method 2* that is essentially based on the tabulated values of Stopping Powers.

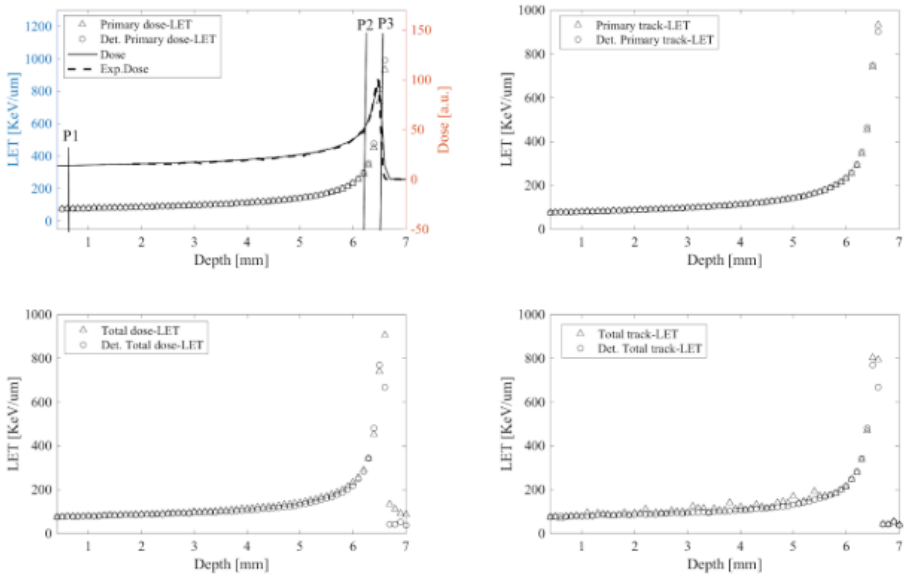

Figure 5.6: LET distributions for the Oxygen beam of 62 MeV/n in water calculated with deterministic and MC method. Relative dose distribution is expressed in arbitrary units. Dose is compared with experimental data, normalized at the entrance. (a) Total and primary LET- dose distributions (b) Total and primary LET- track distributions

5.3.4 The instability of the method 3 for the average dose LET calculation

In order to identify the most accurate method for calculating the LET dose, a systematic study as a function of the cut by applying the *Method 3* was performed. In the Table 5.3 is reported the comparison between the *Method 1* and *Method 3* applied just for the $\bar{L}_D$ calculation.

It appears evident, in this case, a dependence of order of 30% as respect to the cut parameter variation in the entrance position of the proton Bragg peak curve. An even higher value has been registered applying the equation 5.10 and considering the contribute due to the secondary particles produced in a fixed voxel. The maximum variation

Cut [mm]	$\bar{L}_D$ **method 1**	$\bar{L}_D$**method 3**
0.005	1.3212	0.8110
0.01	1.0702	0.9327
0.02	1.0363	1.0050
0.05	1.0702	1.0559
0.08	1.0922	1.0769
0.1	1.0929	1.0871
0.2	1.1489	1.1490
0.5	1.1498	1.1562
0.7	1.1562	1.1562
1	1.1535	1.1535

Table 5.3: The averaged dose-LET for the primary particle calculated with the *Method 1* and *Method 3* (respectively columns two and three) as a function of the cut (column 1)

estimated in this case was the order of 60%. This important result suggested a modification of the previous implemented algorithm in the `Hadrontherapy` application (based on the *Method 3*) and the introduction of a new one based on the *Method 2*.

5.3.5 Validation against the ICRU data-base

In order to validate the *Method 2*, the $\bar{L}_D$ and $\bar{L}_T$ calculated just for the primary particles has been compared to the tabulated value of stopping power reported in the NIST database. For this purpose, the energy spectra of the primary protons in water have been scored for several depth along the Bragg curve (see Figure 5.7)

Cut value has been fixed equal to the voxel size i.e. 100 μm. The energy spectra was converted in a stopping power distribution and compared with the computed LET as shown in Table 5.4

Each LET value resulted to be perfectly in accordance to the tab-

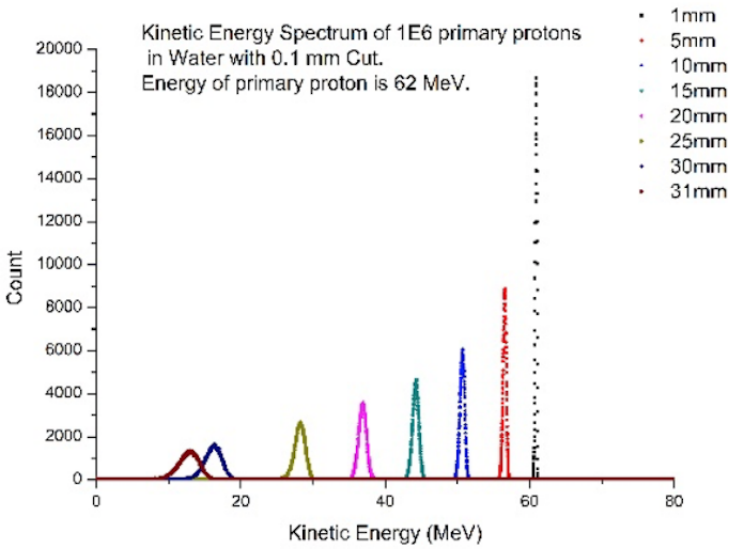

Figure 5.7: Energy spectra of 62 MeV proton beams in water

ulated stopping power spectra. Once validated the algorithm was inserted inside the `Hadrontherapy` application and proceed to a systematic study of light ion LET in water.

5.3.6 A study with light ions by using the Method 2

The results of a systematic study carried out to quantify the influence of secondaries for different ions beam (Z from 1 to 8) and the discrepancy between the $\bar{L}_D$ and $\bar{L}_T$ calculation approaches is reported in this section.

Track and absorbed dose average LET values, for all studied ion beams in three positions along the Bragg peak, is in Table 5.5.

The $\bar{L}_D^{Total}$ is roughly higher than the primary one in the entrance P1. At the distal and proximal position, the $\bar{L}_D$ distributions for total and primary particles are mostly overlapping, the maximum percentage

Depth [mm]	ICRU Stopping Power	$\bar{L}_D$ keV/μm	$\bar{L}_T$ keV/μm
1	1.06 ± 0.01	1.06	1.06
5	1.12 ± 0.01	1.13	1.12
10	1.23 ± 0.01	1.24	1.22
15	1.37 ± 0.02	1.39	1.37
20	1.58 ± 0.04	1.62	1.58
25	1.96 ± 0.09	2.03	1.98
30	3.08 ± 0.46	3.36	3.13
31	3.68 ± 0.72	4.18	3.86

Table 5.4: ICRU Stopping Power (second column) as a function of the proton depth in water (first column) and LET calculated with the *Method 2*: $\bar{L}_D$ (third column) and $\bar{L}_T$ (fourth column)

difference is, in fact, the order of 5%. In Table 5.5 appear, also, evident that in accordance to [4] it is recognised the condition:

$$\bar{L}_D \geq \bar{L}_T \tag{5.16}$$

Thanks to this study, appear evident as, for the same energy beam, a higher local energy to the surrounding normal tissues is released by ions. In fact, in the Table 5.5 has been shown that the portion of the depth-dose curve where high LET is released is strongly influenced by the particle type. While light particles like protons and helium produce high LET only at the distal and proximal part of the Bragg Peak, for the ions from boron to oxygen the high LET region corresponds to the entire curve. Intermediate ions as lithium and beryllium may represent a valid compromise.

The variations occurred using different algorithms have highlighted the

Position	**Ion Species**	$\bar{L}_D$ **[KeV/**mu**m]**	$\bar{L}_T$ **[KeV/**mu**m]**	$\bar{L}_D^{TOT}$ **[KeV/**mu**m]**	$\bar{L}_T^{TOT}$ **[KeV/**mu**m]**
P1	^1H	1.09	1.09	4.79	1.11
	^4He	4.22	4.22	9.34	4.25
	^6Li	9.57	9.57	14.60	9.52
	^9Be	17.08	17.08	21.53	17.05
	^{11}B	26.87	26.87	30.04	26.75
	^{12}C	39.10	39.11	41.49	38.23
	^{14}N	53.61	53.61	55.91	52.14
	^{16}O	70.54	70.54	72.53	68.45
P2	^1H	3.69	3.45	4.35	3.47
	^4He	19.39	19.25	20.81	19.21
	^6Li	44.81	44.55	45.64	40.82
	^9Be	82.43	81.99	82.64	79.79
	^{11}B	136.68	135.68	137.32	129.31
	^{12}C	182.97	181.79	184.64	181.21
	^{14}N	225.27	224.34	226.63	223.11
	^{16}O	272.97	272.16	275.55	273.34
P3	^1H	19.15	12.86	19.18	12.86
	^4He	95.66	70.70	95.03	70.39
	^6Li	210.14	175.67	204.19	175.11
	^9Be	334.74	293.58	327.25	295.42
	^{11}B	452.18	404.64	447.95	406.21
	^{12}C	637.11	586.76	628.70	585.12
	^{14}N	778.99	723.81	769.56	733.44
	^{16}O	930.21	870.73	921.64	869.42

Table 5.5: Dose averaged LET and Track averaged LET at different depth position of the Bragg curve for 62 MeV/n of p, ^4He, ^6Li, ^8Be, ^{10}B, ^{12}C, ^{14}N, and ^{16}O beam.

importance to use a method with a high level of stability and reproducibility. The LET is, in fact, one of the main parameters to estimate the biological damage. The commonly TPSs are based to pre-compiled LET tables and neglect the mixed field contribution present in a real treatment condition. The purpose of this study has been to identify the most stable algorithm that takes into account all components of a real beam for a future application in clinical practice. In the next Chapter an application of the proposed LET algorithm (based on the *Method 2*) for the estimation of the biological damage is discussed.

Chapter 6

Evaluation of Radiobiological Effects in Clinical Proton Beams

At today, there is no simple relationship between released dose and biological effect. Since 1950 to now, several attempts have been done to develop models for the prediction of radiobiological effect as a function of the radiation used in a clinical environment [106]. Some biological aspects as well as the main used radiobiological models will be discussed in this Chapter. One of the main purposes of this thesis work has been, in fact, to evaluate the potentiality of using a Monte Carlo code for the radiobiological damage estimation. The idea has been to study an alternative method to evaluate the biological effect considering the main component of a real beam (i.e. particles species and energy spectra) to improve the quality of the protontherapy treatments.

6.1 The Relative biological effectiveness and the rationale of clinical use of 1.1 RBE value

At equal absorbed doses, radiations of different quality produce different levels of biological and clinical effects. These differences are related to the different mechanisms in energy deposition at the level of particle tracks and subcellular structures [5]. In radiation biology is generally used a quantity called RBE (Relative Biological Effectiveness) to quantify the differences in biological effectiveness of different radiation qualities. The RBE is defined as the ratio of the absorbed dose of a reference radiation D_X, typically 250 kVp X-rays or ^{60}Co gamma rays [5], which produces a given biological effect, to the absorbed dose of the test radiation producing the same effect D:

$$RBE = \frac{D_X}{D} \tag{6.1}$$

At today, the clinical proton therapy is based on the use a single RBE value (RBE=1.1) similar to the adopted value for the photons irradiation (RBE=1). It's well-known that the RBE is not constant (see Figure 6.2), but there are no clinical data indicating that the use of a generic RBE of 1.1 is unreasonable. On the other hand, clinical data cannot confirm that the RBE of 1.1 is correct or not.

In order to implement a future clinical use of a variable RBE understanding of the relationship between LET, dose and biological endpoint is necessary. Systematic quantitative statements regarding therapeutic situations are still difficult due to the experimental uncertainties, the specific experimental arrangements used, and different biological endpoints chosen in the experiments. At present, this aspect is widely discussed. More than one radiobiological models have been developed with the purposing of understand and clarify the relationship between

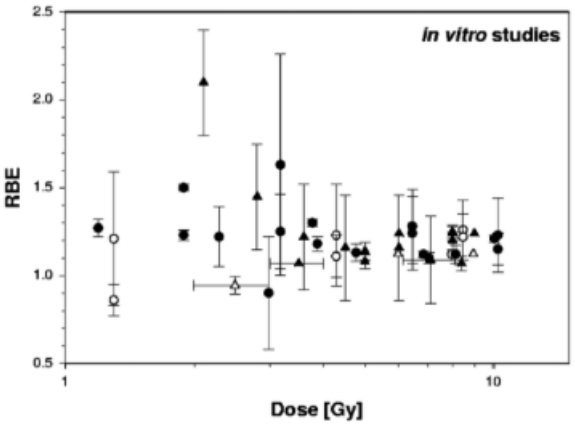

Figure 6.1: Experimental proton RBE values (relative to ^{60}Co) as a function of dose/fraction for cell inactivation measured in vitro in the center of a SOBP. Closed symbols show measurements using Chinese Hamster cell lines and open symbols stand for other cell lines. Circles represent RBE's for E<100 MeV beams and triangles for E>100 MeV beams.

the radiation properties and biological damage [135] [136] [94] [25] [27] [48] [57].

6.2 Modeling cellular radiation effect

Radiobiological models are used in modern radiotherapy to evaluate the biological effects of different treatment plans or radiation modalities. Typically, these models are able to converts a physical quantity to a biological quantity. A wide data acquired in-vitro and in-vivo show a dependence of the dose released to the cell damage that can be described by the Linear-Quadratic (L-Q) Model. Over the last fifty years severals model have been developed to reproduce the observed L-Q trend. At today the wide used are the Local Effect Models (LEM) [135] [136] and Microdosimetric Kinetic Model (MKM) [57].

6.2.1 The Linear Quadratic Model

The Linear-Quadratic model [70] which characterizes the biological damage (in term of number of survived cells as function of the absorbed dose) is described by two main parameters α and β. In particular, the Surviving Fraction (or SF) of irradiated cells at a certain dose D is given by:

$$SF = exp(-\alpha D - \beta D^2) \tag{6.2}$$

At today, this model is widely used in clinical practice, as reported on the ICRU [5]:
The Linear Quadratic model is well established as a mathematical tool used to manipulate total dose and dose per fraction to maintain clinical iso-effectiveness and to predict and plan modified fractionation for any type of ionizing radiation therapy including high and low LET radiation.

Starting to the L-Q model is possible to formulate the RBE considering two survival curves as a function of the dose for the same biological system but for two different radiations: a reference radiation with parameters α_X and β_X and an incident beam, for instance protons, with α_p and β_p (see Figure 6.2).

The RBE at a certain dose D is then given by:

$$RBE(D, \alpha_x, \beta_x, \alpha, \beta) = \frac{\sqrt{\alpha_x^2 + 4\beta_x D_p(\alpha + \beta D)} - \alpha_x}{2\beta_x D} \tag{6.3}$$

in the limits at very low and very high doses, this can be simplified to

$$lim_{D_p \to 0} RBE(D, \alpha_x, \beta_x, \alpha, \beta) = \frac{\alpha}{\alpha_x} \tag{6.4}$$

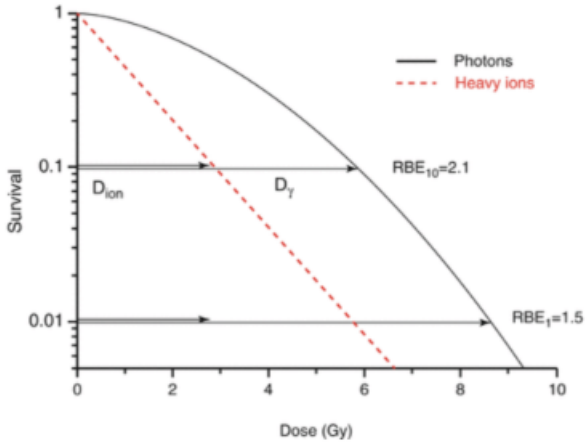

Figure 6.2: Survival curves for cells irradiated with photons and ions and determination of RBE for cells inactivation at 10% and 1% survival level.

$$lim_{D_p \to \infty} RBE(D, \alpha_x, \beta_x, \alpha, \beta) = \sqrt{\frac{\beta}{\beta_x}} \tag{6.5}$$

The tissue and biological endpoint dependence is determined by the α and β parameters for the reference radiation X and for the studied radiation. However the values of α and β are not fixed but they depend on the radiation quality or LET as reported in the Figure 6.3.

6.2.2 The Local Effect Model

General concept

The principal assumption of the Local Effect Model is that the expectation value of the biological effect, i.e. the biological damage in a small subvolume of the cell nucleus, is solely determined by the energy deposition in that subvolume and is independent of the particular radiation type leading to that energy deposit [5].

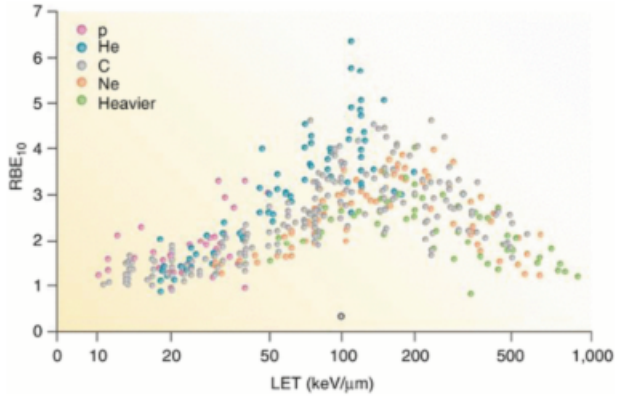

Figure 6.3: Compilation of RBE data for various ions and cell types as a function of the LET

For a given biological object all the differences in the biological action of charged particle beams should then be attributed to the different spatial energy deposition pattern of charged particles compared to photon irradiation. In Figure 6.4 the influence of track structure on the microscopic dose distribution in a cell nucleus is schematically reported.

The calculation of the biological effects of charged particle radiation is based on their different microscopic pattern of energy deposition compared to photon radiation. The basic variable for the calculation is the expectation value of the dose deposited at a given point (x,y,z) in the nucleus for a given set of incoming primary photons or particles; this quantity is called *local dose* and denote it by d(x,y,z) [48]. For photons the spatial distribution of the local dose can be assumed to be homogeneous even down to nanometer volumes. In contrast for particle radiation the distribution is characterized by the extreme heterogeneity due to the $1/r^2$ distribution of local dose [102] [148]. According to the Poisson distribution of the lethal events, the average number of these events per cells can be obtained by the integration of the local density

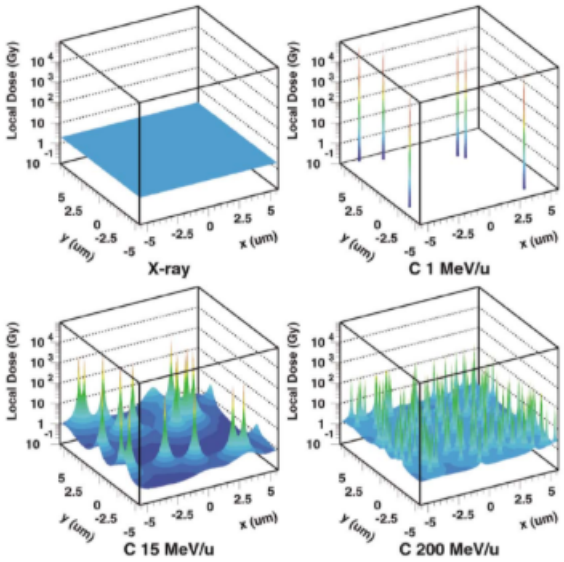

Figure 6.4: Local dose distribution of x-rays and carbon ions at different specific energies. The average dose is 2 Gy in each case. The size of the area is 10x10 μm^2 and corresponds to the typical size of mammalian cell nuclei

$V_{ion}(d(x,y,z))$ inside a nucleus with volume $V_{Nucleus}$.

$$N_{ion} = \int v_{ion}(d(x,y,z))dV_{Nucleus} \tag{6.6}$$

The fundamental assumption of the LEM is that the local biological effect is determined by the local dose (independently to the radiation type), so the event densities for ions are equal to photons for the same local dose:

$$v_{ion}(d) = v_x(d) \tag{6.7}$$

Thus, equal local doses correspond to equal local biological effects:

$$N_{ion} = \int \frac{-logS_X(d(x,y,z))}{V_{Nucleus}dV_{Nucleus}} \tag{6.8}$$

where S_X is the Survival Fraction for the x rays radiation. Equation 6.8 is the most general formulation of the LEM model. A modified version of the linear quadratic approach is also included in the code. Several experimental data suggest the existence of a specific transition from the shouldered to an exponential shape of the dose response curve at high doses.

This transition is described by a parameter D_t representing the transition dose to the exponential shape with slope $s_{max} = \alpha + 2\beta D_t$ so that the doses response is finally given by:

$$-lnS_X = \begin{cases} \alpha_X D + \beta_X D^2 & D \leq D_{cut} \\ \alpha_X D_{cut} + \beta_X D_{cut}^2 + s_{max}(D - D_{cut}) & D > D_{cut} \end{cases} \tag{6.9}$$

The dose D_t is a specific parameter of each cell line and can be experimentally measured. In conclusion, the input parameters of the models are:

- the α_X and β_X parameters experimentally obtained by the irradiation with the reference X-rays;
- the dose D_t related to a specific cell line;
- the mean radius of the cell line $r_nucleus$ that identify the sensible region.

LEM II and LEM III

The first improvement of the LEM (called LEM II) considers an additional mechanism that increases the radiation damage at large local doses. For the X-ray response curve, for higher doses (with a threshold dose D_t above a few hundred Gy), an additional cluster effect due to the enormous ionization densities in the track center must be considered. These clusters produce additional DSBs that are responsible for

an increased radiation effect for high local doses. LEM III applies an energy-dependent track core as a new feature to describe the track center more realistically. This new model reduce the biological response for fast ions with a wide core as compared to the previous version of the model [91].

6.2.3 The Microdosimetric Kinetic Model

Another widespread model that is important to briefly describe is the so-called Microdosimetric Kinetic Model (or MKM). The MKM is based on the concept that the cell nucleus is divided into microdomains with a radius R_D which fill up the cell [69]. The number of lesions in the cell nucleus is related to cell survival by $L_{nucl} = -ln(S)$. It was shown that L_{nucl} can be determined by means of the microdosimetric quantity $z_1 D$ describing the single-event dose [57]:

$$\langle L_{nucelus} \rangle = (\alpha_0 + \beta_{z1D})D + \beta D^2 \tag{6.10}$$

where α_0 and β are the linear-quadratic parameters following X irradiation and D is the absorbed dose. As a result of the derivation of the MKM , the Equation 6.10 shows that the quadratic term β is constant for all radiation qualities and only z_{1D} must be determined. Conveniently, z_{1D} can be either measured with a tissue-equivalent proportional counter or calculated by means of the probability density $f_1(z)$ of the specific energy z deposited by single energy deposition events in the microscopic domain [69]:

$$z_1 D = \frac{\int_0^\infty z^2 f_1(z) dz}{\int_0^\infty z f_1(z) dz} \tag{6.11}$$

the specific energy z can be determined by assuming an amorphous track structure model. The inner part of the track (called core) is assumed as a plateau whose outer range depend on the particle energy.

The radial extension of the track r_{max} depends on the energy E only and can be parametrized by:

$$r_{max} = \gamma E^{\delta} \tag{6.12}$$

with $\gamma = 0.062$ and δ=1.7 Hence, the MKM shows good agreement for in vitro cell inactivation for a large range of LET/particles combination as shown in the Figure 5.6

6.3 A Monte Carlo approach for radiobiological quantities calculation

Event-by-event track structure simulations can be very helpful in understanding the action of radiation in biological targets because they can represent a starting point for the development of models based on the energy deposited at the nanometer scale. Unfortunately, this simulation approach cannot be used for the treatment planning in radiotherapy, due to the enormous number of interactions involved and the high computational time required. A condensed story approach is therefore applied [104]. This method is very efficient but an obvious consequence is a loss of information. A good compromise between condensed story and event-by-event track structure code can be the integration in condensed history Monte Carlo codes of calculation results carried out using event-by-event track structure code. This thesis discusses the potentialities of Geant4 in the calculation of the in-vitro Survival Fraction and the RBE in therapeutic proton beams. Two different approaches have been developed to reach this goal: a pure computational method, that couples the Geant4 (a condensed story approach) with the LEM model (based on a track structure approach); a parameterized method fully inspired to the McNamara work [99] where are applied the results reported in the Chapter 6 on LET calculation; Both methods were ap-

plied to reproduce survival curves measured during two experimental campaigns conducted at the CATANA protontherapy facility.

6.3.1 Survival fraction calculation: the LEM approach coupled to Geant4

The mixed radiation field

The coupling between Geant4 and LEM has been carried out in accordance with the Theory of Dual Radiation Action (TDRA) [72]. This approach is essentially based on the concept that a biological system exposed to more than one radiation type shows a sort of synergism: the total number of lesions is larger than the sum of lesions produced by each hitting particles. Following this theory the number of lesions can be expressed as a sum of more than one contribute weighted to the radiation released dose D. The TDRA can be efficiently applied by using the Geant4 Monte Carlo simulations that can accurately reproduce the mixed radiation field, i.e. a mixture of radiation qualities where different ions of different energies (and, hence, different LETs) concurrently contribute to the radiobiological outcome, i.e. to the cell damage.

The formulation of a model that includes the influence of mixed radiation field has been carried out starting from the observed different effects at low doses and high doses at chromosome damage level. The yield of lesions Y follows a linear-quadratic models [16]:

$$Y(D) = \alpha D + \beta D^2 \tag{6.13}$$

In the case of a sequential exposure due to two doses D_1 and D_2 related to different radiation types, the total number of lesions can be written as a combination effect of these two contributes:

$$Y(D_1, D_2) = \alpha_1 D_1 + \beta_1 D_1^2 + \alpha_2 D_2 + \beta_2 D_2^2 + 2(\beta_1 \beta_2)^{1/2} D_1 D_2 \tag{6.14}$$

where α_1, β_1 and α_2 β_2 are the parameters of Equation 6.13. The method can be generalised to n doses from n radiation types (each characterized by a certain value of the parameters α_i and β_i). In this case the expression 6.14 becomes:

$$\varepsilon(D_1, D_2, ..., D_3) = \sum_{i=1}^{n} \alpha_i D_i + (\sum_{i=1}^{n} \sqrt{\beta_i} D_i)^2 \tag{6.15}$$

Within this formalism the averaged parameters for a mixed field can be calculated as:

$$\langle \alpha_D \rangle = \frac{\sum_i \alpha_{D_i} \cdot D_i}{\sum_i D_i} \tag{6.16}$$

$$\langle \beta_D \rangle = \left(\frac{\sum_i \sqrt{\beta_{D_i}} \cdot D_i}{\sum_i D_i} \right)^2 \tag{6.17}$$

The Equations 6.16 and 6.17 include the contributions of all secondary particles produced by the interaction of the primary with biological tissue. Therefore α_D and β_D result in a weighted mean to the different radiation type.

The implemented algorithm

The approach described in the previous section has been adopted to calculate the cell survival fraction and, consequently, the RBE by using Geant4. The flowchart of the algorithm implemented is reported in Figure 6.5.

The algorithm has been inserted inside a class called `HadrontherapyRBE.cc` of the official version of `Hadrontherapy` example: the α_D and β_D parameters are calculated in the voxelized geometry of the water phantom placed at the end of each beam line. The LET value of any primary ion and of the secondaries generated in each slice of the phantom, is retrieved at each simulation step. The corresponding values of α_{D_i} and

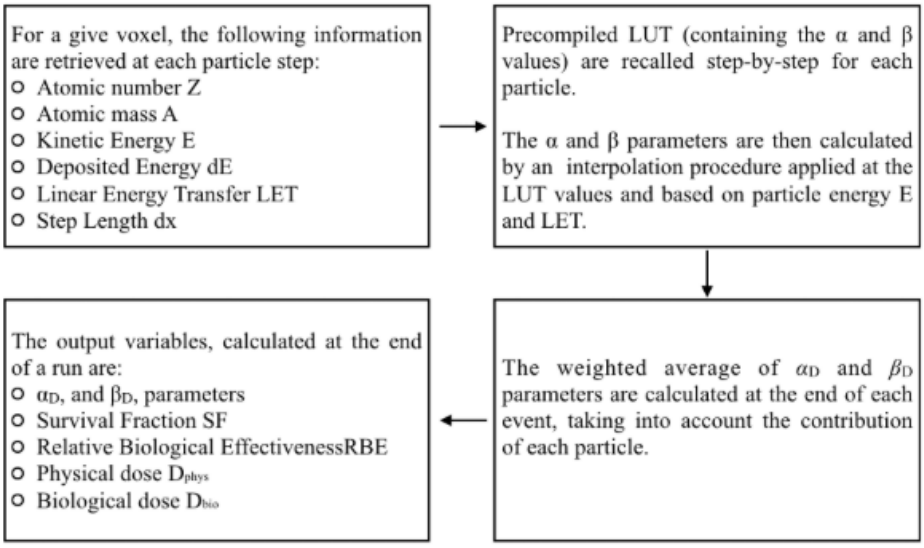

Figure 6.5: Schematic representation of the main steps performed to compute the RBE using the LEM coupled to Geant4 inside Hadrontherapy example

β_{D_i}, for each specific radiation type i with a released dose D_i, are calculated by direct linear interpolation of α_D and β_D values inserted in specific Look Up Tables (LUT) and calculate by using the LEM models. All interpolated α_{D_i} and β_{D_i} are then weighted to derive the average values $\langle\alpha_D\rangle$ and $\langle\beta_D\rangle$ in each slice according to the equation 6.16 and 6.17. This approach allows to take into account, at run time, the complexity due to the presence of a mixed field. The final value Survival Fraction curves is then calculated according to the Linear-Quadratic model:

$$SF = e^{-(\langle\alpha_D\rangle D + \langle\beta_D\rangle D^2)} \tag{6.18}$$

for a specific released dose D.

Calculated Look Up Tables

Specific Look-Up Tables (LUT) containing the α_D and β_D values for a given monoenergetic ions (from Z=1 to Z=8) and cell type and as function of ion LETs and energy values, have been generated using the LEM model. An example of produced LUT is reported in the Figure 6.6

	alpha_x	beta_x	r_nucleus	D_t	specific_energy	let	alpha	beta	cell	particle	RBE_alpha
1	0.11	0.06	6.5	8	172.698	0.5	0.127549	0.0588984	U87	H	1.15953636363636
2	0.11	0.06	6.5	8	143.534	0.567824	0.138268	0.0582273	U87	H	1.25698181818182
3	0.11	0.06	6.5	8	119.965	0.644847	0.149487	0.0575248	U87	H	1.35897272727273
4	0.11	0.06	6.5	8	100.952	0.732319	0.161175	0.0567928	U87	H	1.46522727272727
5	0.11	0.06	6.5	8	85.4798	0.831656	0.173273	0.0560348	U87	H	1.57520909090909
6	0.11	0.06	6.5	8	72.4215	0.944468	0.18615	0.0552277	U87	H	1.69227272727273
7	0.11	0.06	6.5	8	61.3953	1.07258	0.19987	0.0543674	U87	H	1.817
8	0.11	0.06	6.5	8	52.3329	1.21808	0.21415	0.0534717	U87	H	1.94681818181818
9	0.11	0.06	6.5	8	44.5844	1.3833	0.229405	0.0525143	U87	H	2.0855
10	0.11	0.06	6.5	8	38.033	1.57095	0.245631	0.0514955	U87	H	2.23300909090909
11	0.11	0.06	6.5	8	32.4783	1.78404	0.262885	0.0504115	U87	H	2.38986363636364
12	0.11	0.06	6.5	8	27.7871	2.02604	0.281233	0.049258	U87	H	2.55666363636364
13	0.11	0.06	6.5	8	23.8148	2.30087	0.300765	0.0480292	U87	H	2.73422727272727

Figure 6.6: Typical Look Up Table obtained by using Survival code

The LEM evaluations have been performed using the *Survival* software developed by the INFN, which provides the implementation of variants of the Local Effect Model (LEM, version I, II and III) and the MKM [95].

6.3.2 Implementation of the parametrized L-Q model

More than one experimental evidence suggests the existence of a correlation between the local energy deposition, expressed in terms of LET, and the radiobiological effects [108]. Dose-averaged LET ($\bar{L}_D$) represents a reasonably good approximation of the physical characteristics of the radiation field for protons up to the depth at which the Bragg

peak occurs. In a recent paper, McNamara et al. [99] analysed an extremely wide set of radiobiological experimental data, and derived a phenomenological model able to predict the proton RBE when the released dose D_p, the $\bar{L}_D$ and the ratio between α and β value $\left(\frac{\alpha}{\beta}\right)_X$ corresponding to the reference radiation, for a given cell line known. The model permits the calculation of the RBE values by the formula:

$$RBE = \frac{1}{2} D_p \sqrt{R^2 + 4D_p R(p_0 + \frac{p_1}{R} \cdot \bar{L}_D + 4D_p^2(p_2 - p_3\sqrt{R} \cdot \bar{L}_D)^2} - R \tag{6.19}$$

Here p_0, p_1, p_2 and p_3 are the fit parameters and R is the $(\frac{\alpha}{\beta})_X$ ratio while $\bar{L}_D$ is the LET of the incident radiation that in this study correspond to the algorithm described in the Chapter 5 and mentioned as *Method 2*.

6.4 A systematic study of Survival Fraction prediction

The two approaches described in the Section 3 has been applied to reproduce the Survival Fraction and to quantify the biological damage due to proton irradiation with different cell lines of different experimental campaigns. The first chosen experimental campaign was carried out by Chaudhary et coll. [30]. It consisted in the irradiation of U87 radioresistant human glioma cells at six different depths along a monochromatic (62 MeV) and modulated clinical proton Spread Out Bragg Peak beam. During this thesis work another specific experiment was organised irradiating the more radio-responsive prostate DU145 cells and MDA-MB145 respectively along three and two points of the SOBP. The whole experimental set-up of the two campaigns, including the transport beam line, diagnostic elements and cellular irradiation

conditions, were accurately simulated using the public release of the `Hadrontherapy` example.

6.4.1 Simulated set-up

In order to reproduce the experimental depth dose distributions, the CATANA irradiation beam line and its clinical water phantom were simulated. The phantom was divided in slices 400x400x0.01 mm in thickness. The slices were orthogonal to the beam axis direction. Dose, fluence dose-averaged LET, RBE and all quantities necessaries for their estimation were scored during the simulation in each slice. The simulated primary proton beam had a Gaussian energy distribution, centered at the nominal energy of 62.45 MeV with a standard deviation of 0.25 MeV. The beam spot was assumed circular and modelled as a bivariate Gaussian distribution having standard deviations of 0.5 mm. Beam angular distribution was assumed Gaussian with a standard deviation of 0.028 degree. A total of 10^7 particle histories were simulated in each run. The clinical SOBP dose distribution was obtained by simulating one of the modulator wheels used for the clinical sessions. Figure 6.7 shows the simulated SOBP in water and the corresponding primary proton dose-averaged LET.

The corresponding depth dose, acquired in water with a Markus Advanced ionisation chamber, is also displayed.

6.4.2 Irradiation and experimental set-up

It was investigated the response to proton irradiation of radioresistant human glioma (U87), the relatively more radiosensitive prostate cancer DU145 and breast cancer cell line MDA-MB-231. U87 were irradiated in an experimental campaign conducted at the CATANA protontherapy facility of INFN-LNS. Irradiations were carried out in six different

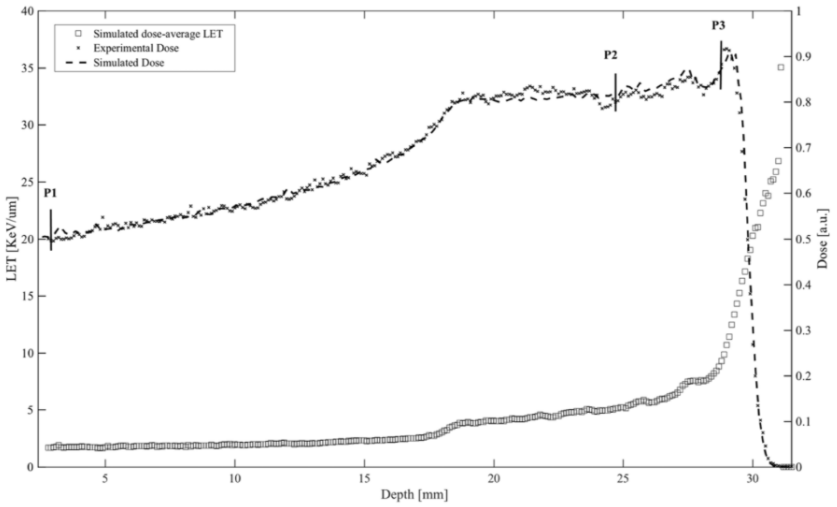

Figure 6.7: Proton Spread-Out Bragg Peak (SOBP) used for cells irradiations, measured in water with a PTW (Freiburg, D) Markus advanced ionisation chamber (dotted line) and simulated (dashed line) with the `Hadrontherapy` Geant4-based application. DU145 cells were placed at points T1, T2 and T3 corresponding to the depths of 5, 21 and 28.9 mm in water, respectively. Triangles represent the dose averaged LET profiles

positions (P1, P2, P3, P4, P5 and P6) along a pristine Bragg peak (corresponding to LET values of 1.1, 4.0, 7.0, 11.9, 18.0, and 22.6 keV/μm, respectively) and in six different positions along a modulated spread out Bragg peak (corresponding to LET values of 1.2, 2.6, 4.5, 13.4, 21.7 and 25.9 keV/μm.). Details on U87 campaign can be found in Chaudhary et al. [30]. DU145 and MDA-MB-231 were irradiated at the same beam line, in a dedicated experimental campaign. Irradiations were performed to gather data in addition to those obtained U87, using a cell line of differing radiosensitivity belonging to a type of tumour frequently treated with protons. DU145 and MDA-MB-231 irradiations were conducted along a clinical proton SOBP in three positions (T1, T2 and T3) corresponding to the depths of 5, 21 and 28.9 mm in wa-

ter (and LET values of 1.96, 4.24 and 20.62 keVμm). In each position doses of 0.5, 1, 2 and 4 Gy were delivered to the cells. Absolute dosimetry was performed in water by means of a plane-parallel PTW 34045 advanced Markus ionisation chamber, according to the International Atomic Energy Agency Technical Report Series 398 Code of practice [5]. Dose were measurements at a depth corresponding to the middle of the SOBP, using a reference 25 mm diameter circular collimator. The clinical proton beam calibration was performed before each irradiation [38].

6.4.3 The comparison with experimental data

Survival curves for U87, DU145 and MDA-MB 231 cell lines were reproduced according to LEM III and the parameterised approaches. Results were compared against the experimental survival curves.

Results obtained with U87 cell line

The work from Chaudhary [30] reports the values of α_D and β_D parameters, derived from the fit of the experimental data with the well-known linear-quadratic expression (equation 6.18) [27] [49]. U87 experimental survival curves, at the six positions along the 62 MeV pristine Bragg peak, are reported in Figure 6.8. The light-grey band represent the SF expectation (68% coverage) based on the data by Chaudhary et al. The band was calculated by letting the parameters α_D and β_D fluctuate according to the central values and the uncertainties reported in [30]. Survival curves calculated using the LEM (open squares) and the parameterized approach (open circles), are also reported. Survival curves for the same U87 cells, irradiated in six different position along the modulated SOBP, are reported in Figure 6.9. The dose-response curves well reflect the increase in RBE with increasing proton LET, which rises from about 1 to over 22 keV/μm from P1 to P6, with a

progressively steeper slope as described by the α_D parameter. A significant increase in radiosensitivity is marked in the shoulder as described by the beta parameter can be observed, which becomes particularly evident in the curves obtained from cells irradiated in positions P4 to P6. A similar trend can be observed for U87 cells irradiated along the SOBP, although in this case the increase in the dose-response curve initial slope is less marked compared to the monoenergetic beam. Similarly, the curvature (β parameter) changes slightly from P1 to P6. α and β parameters resulted dependent from the LET (see Table 6.1). Particularly, α values proportionally increase while β decrease with LET.

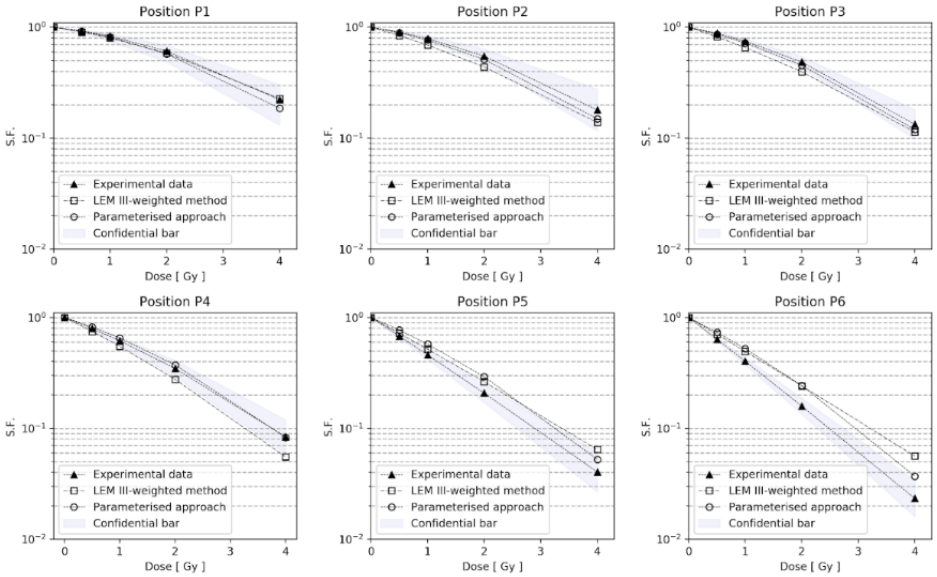

Figure 6.8: Experimental survival data of the U87 cells irradiated in six different positions along the 62 MeV proton pristine Bragg peak (positions from P1 to P6) according to the parametrization of [99]. The light-gray bands represent the expected variations of experimental data, calculated on the basis of the uncertainties reported α_D and β_D. Survival curves calculated using the LEM (open squares) and parameterized approach (open circles), are also reported

U87 - Pristine							
		Position P1	Position P2	Position P3	Position P4	Position P5	Position P6
Experimental results	alpha $[Gy^{-1}]$	0,12 ± 0,04	0,17 ± 0,04	0,22 ± 0,04	0,44 ± 0,04	0,77 ± 0,09	0,90 ± 0,07
	beta $[Gy^{-2}]$	0,06 ± 0,009	0,06 ±0,017	0,07 ± 0,009	0,04 ± 0,002	0,008 ± 0,003	0,01 ± 0,006
Parameterized approach	alpha [Gy^-1]	0,13 ± 0,0001	0,19 ± 0,0002	0,25 ± 0,0003	0,36 ± 0,0004	0,49 ± 0,0005	0,59 ± 0,0006
	beta $[Gy^{-2}]$	0,07 ± 0,0002	0,07 ± 0,0006	0,07 ± 0,0003	0,064 ± 0,003	0,06 ± 0,002	0,05 ± 0,003
LEM III weigthed method	alpha $[Gy^{-1}]$	0,17 ± 0,0002	0,33 ± 0,0003	0,38 ± 0,0004	0,56 ± 0,0005	0,65 ± 0,0006	0,65 ± 0,0006
	beta $[Gy^{-2}]$	0,05 ± 0,0005	0,41 ± 0,0005	0,041 ±0,0005	0,041 ± 0,0007	0,009 ± 0,0009	0,009 ± 0,0005
U87 - SOBP							
		Position P1	Position P2	Position P3	Position P4	Position P5	Position P6
Experimental results	alpha $[Gy^{-1}]$	0,16 ± 0,04	0,19 ± 0,04	0,22 ± 0,04	0,22 ± 0,04	0,41 ± 0,09	0,50 ± 0,07
	beta $[Gy^{-2}]$	0,05 ± 0,015	0,05 ± 0,051	0,06 ± 0,016	0,06 ± 0,016	0,05 ± 0,042	0,06 ± 0,033
Parameterized approach	alpha $[Gy^{-1}]$	0,13 ± 0,001	0,16 ± 0,002	0,2 ± 0,002	0,39 ± 0,004	0,57 ± 0,006	0,57 ± 0,006
	beta $[Gy^{-2}]$	0,07 ± 0,0002	0,071 ± 0,0006	0,069 ± 0,0003	0,063 ± 0,003	0,058 ± 0,003	0,058 ± 0,003
LEM III weigthed method	alpha $[Gy^{-1}]$	0,17 ± 0,0002	0,18 ± 0,0003	0,34 ± 0,0004	0,34 ± 0,0004	0,53 ± 0,0005	0,62 ± 0,0006
	beta $[Gy^{-2}]$	0,05 ± 0,0005	0,05 ± 0,0004	0,04 ± 0,0004	0,04 ± 0,00001	0,003 ± 0,0001	0,002 ± 0,0002

Table 6.1: Alpha and Beta parameters calculated using the two approaches: LEM III weighted method and Parametrized; Experimental data are also reported.

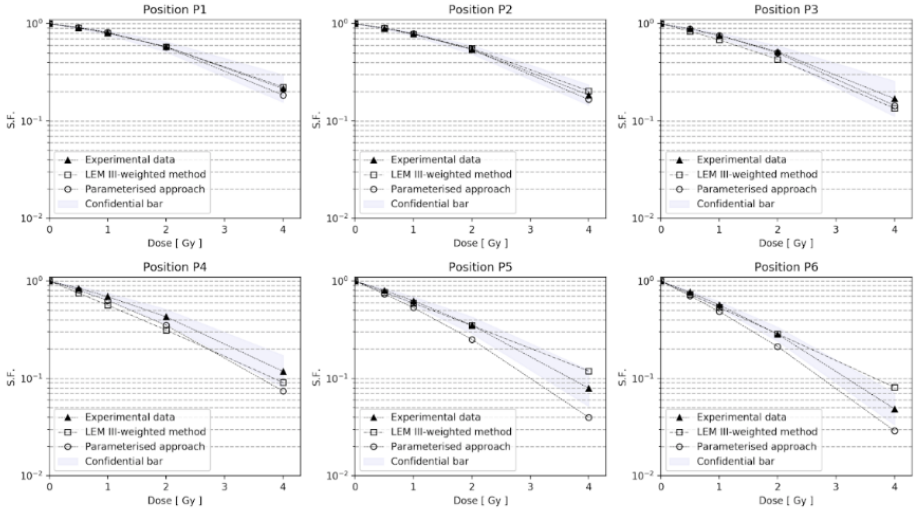

Figure 6.9: Experimental survival data of U87 cells in six different position along the 62 MeV proton SOBP Bragg peak (position from P1 to P6) according to the parametrization of [99]. The light-gray bands represent the expected variations of experimental data, calculated on the basis of the uncertainties reported α_D and β_D. Survival curves calculated using the LEM (open squares) and parameterized approach (open circles), are also reported

Results obtained with DU145 and MDA-MB 231 cell lines

For the DU145 and MDA-MB 231 cells a direct comparison of the SFs at different doses can be performed. In Table 6.2 the experimental alpha and beta parameters compared with the two approaches is reported. Figure 6.10 and Figure 6.11 displays the experimental survival fractions obtained respectively for DU145 and MDA-MB 231 cells irradiated in the positions T1, T2 and T3 of the proton SOBP marked in Figure 6.7. The same plots also report the results from Monte Carlo simulations, using the two calculation approaches. Error bars on experimental data were derived by taking into account the standard uncertainties affecting colony counting, cell dilution and plating efficiency. Specifically, the

error $\sigma_E(SF)$ on the SF must take into account the normalization factor given by the so-called plating efficiency PE, which represents the colony-forming ability or SF of unirradiated cells:

$$PE = \frac{X_{colonies}}{X_{cells}}|0Gy \tag{6.20}$$

$\sigma_E(SF)$ can be determined as follows:

$$\sigma_E(SF_D) = \sqrt{\left(\frac{1}{PE}\sigma_{E_{colonies}}X_{cells}\right)^2 + \left(-\frac{SF}{(PE)^2}\sigma_E(PE)\right)^2} \tag{6.21}$$

Errors on calculations (not visible in the Figure 6.10 and Figure 6.11 being too small) were obtained by combining the simulation statistical errors and the contributions coming from the propagation of the uncertainties of $\langle\alpha_D\rangle$ and $\langle\beta_D\rangle$ from the respective look-up tables.

6.4.4 Statistical Analysis

Experimental clonogenic curves for U87, DU154 and MDA-MB 231 cell lines, all irradiated along the same beam line were compared with the results obtained using two different computational methods: Monte Carlo LEM III-weighted method and a parameterised approach, for the estimation of the radioresponse following cellular exposure to protons. Cells were irradiated using a pristine 62 MeV monochromatic Bragg peak and a clinical SOBP, at various depths in water corresponding to different LET values. The agreement between experimental and calculated curves is satisfactory for the three considered cell lines. As visible in Figure 6.8, Figure 6.9 and Table 6.3, a slightly discrepancy can be observed for the U87 cells at higher LET values, i.e. at greater depths of the particle beams.

Simulations overestimate results for higher LET values (more than 7 keV/μm) corresponding to depths beyond 27 mm in water. Such

DU145				
		Position T1	Position T2	Position T3
Experimental results	alpha $[Gy^{-1}]$	0,32 ± 0,102	0,31 ± 0,02	0,54 ± 0,02
	beta $[Gy^{-2}]$	0,02± 0,0321	0,03 ± 0,007	0,09 ± 0,053
Parameterized approach	alpha $[Gy^{-1}]$	0,26 ± 0,003	0,31± 0,003	0,39 ± 0,003
	beta $[Gy^{-2}]$	0,07± 0,003	0,07 ± 0,003	0,04± 0,003
LEM III weigthed method	alpha $[Gy^{-1}]$	0,22 ± 0,003	0,6 ± 0,003	0,34 ± 0,0004
	beta$[Gy^{-2}]$	0,03 ± 0,003	0,009 ± 0,003	0,04± 0,0004

± MDA-MB 231

		Position T1	Position T2	Position T3
Experimental results	alpha $[Gy^{-1}]$	-	0,22± 0,0545	0,65± 0,0770
	beta $[Gy^{-2}]$	-	0,08 ± 0,0160	0,04± 0,0221
Parameterized approach	alpha $[Gy^{-1}]$	-	0,12 ± 0,0003	0,25 ± 0,0003
	beta $[Gy^{-2}]$	-	0,06 ± 0,0002	0,05 ± 0,0002
LEM III weigthed method	alpha $[Gy^{-1}]$	-	0,23 ± 0,0001	0,58± 0,0001
	beta $[Gy^{-2}]$	-	0,052 ± 0,0002	0,02 ± 0,0003

Table 6.2: Alpha and Beta parameters calculated using LEM III and Parametrized approaches; Experimental data are also reported.

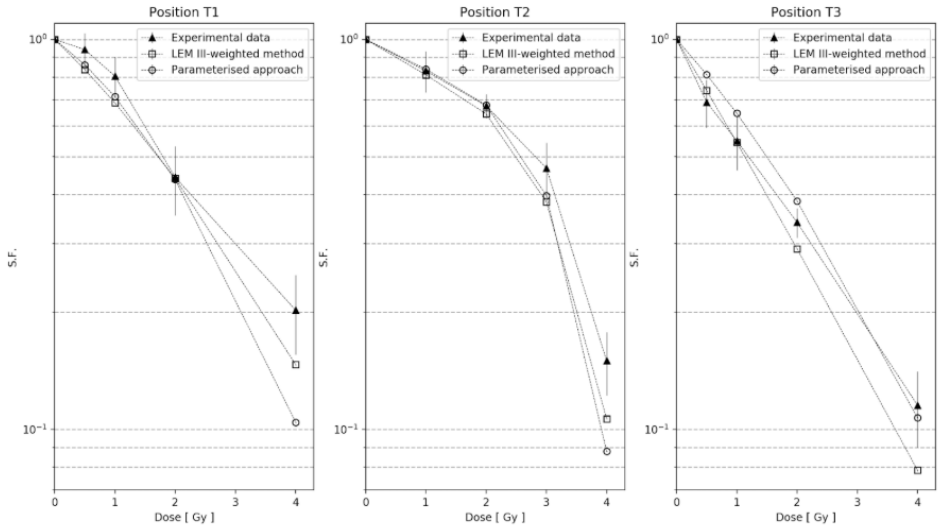

Figure 6.10: Experimental cell survival fraction measured irradiating DU145 cells in three different positions along the clinical proton SOBP of Figure 6.7. The correspond curves calculated by using the Monte Carlo LEM III-weighted method (dashed lines) and the parameterised approach (dotted lines), are reported.

discrepancies may be connected with the uncertainty on flask window thickness and positioning, which becomes critical at the end of the particle range. It may also be connected to the wider particles energy spectra in that position. In the distal part of the Bragg curve, in fact, very small differences in depth (of the order of hundreds of μm) can produce differences in the LET values up to 15%.

For the DU145 and MDA-MB 231 cells, a χ^2 test has been performed in order to quantify the agreement between experimental and simulated SFs. Results of the test are reported in Table 6.3: the χ^2 values calculated over the four available data points (0.5, 1, 2 and 4 Gy) and the corresponding p-values are shown for the three studied positions. For the DU145 cell lines, the resulted p-value is well above than 0.05, showing that the models are able to reproduce the experimental

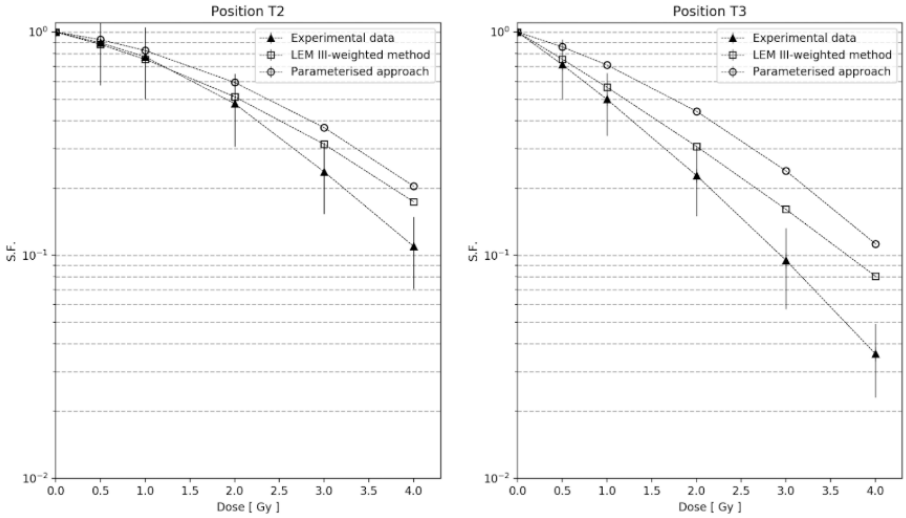

Figure 6.11: Experimental cell survival fraction measured irradiating MDA-MB 231 cells in three different positions along the clinical proton SOBP of Figure 6.7. The correspondent curves calculated by using the Monte Carlo LEM III-weighted method (dashed lines) and the parameterised approach (dotted lines) are reported.

data. The parametrized model under-estimates the SFs at high doses at the distal position T3, yielding a p-value around 0.05. The LEM model also predicts a lower SFs for the high doses at the distal position T3, but the difference is well within the statistical fluctuations.

The MDA-MB 143 cell lines result in accordance with experimental data for the position T2, corresponding to the MID-SOBP of the Bragg curve. The p-value calculated for the position T3 is lower than 0.05 as shown in Table 6.3. This disagreement is essentially due to the higher uncertainty of the cells positioning during the experimental campaign.

In general, the LEM III-weighted model shows a better agreement than the parametrized one; in all cases the most critic points resulted the distal ones where positioning errors are most significant.

The agreement between calculated and experimental data appears

DU145				
	LEM III weigthed method		Parameterized approach	
Position	χ^2	p-value	χ^2	p-value
T1	4,14	0,38	6,06	0,19
T2	4,23	0,37	5,95	0,20
T3	5,14	0,27	5,32	0,25
MDA-MB 231				
	LEM III weigthed method		Parameterized approach	
Position	χ^2	p-value	χ^2	p-value
T2	3,64	0,45	9,10	0,05
T3	15,85	0,03	58,70	$5{,}4*10^{-12}$

Table 6.3: Results of the χ^2 test for the comparison of the experimental survival curves of Figure 4 against survival fraction calculated with the LEM III and parameterised approaches. The corresponding χ^2 probabilities are calculated for four degrees of freedoms

evident also for the RBE curves reported in Figure 6.12. In all investigated cases the RBE prediction entirely falls in the experimental error bars.

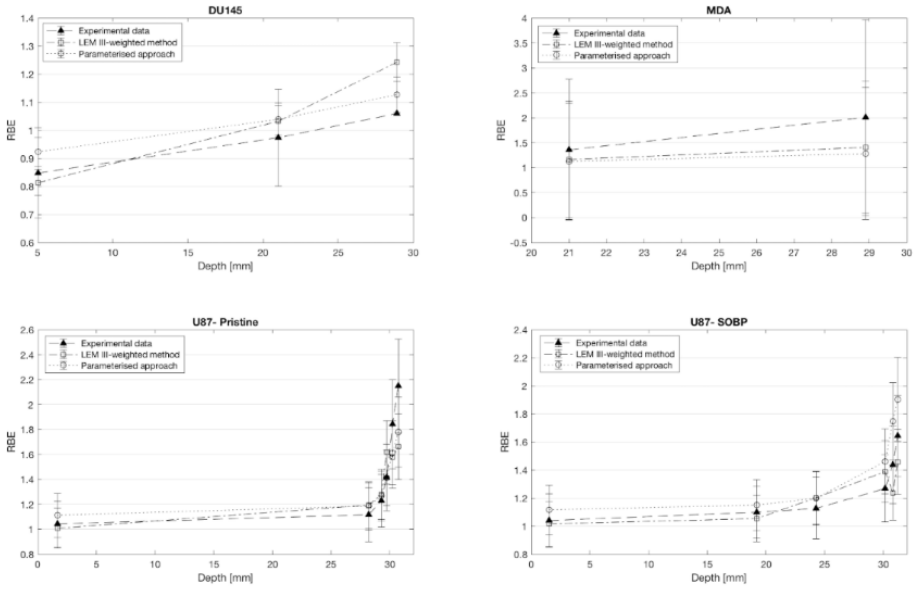

Figure 6.12: Experimental RBE measured irradiating DU145, MDA-MB 231 and U87 cells in different positions along the Bragg curve. The calculated values by using the Monte Carlo LEM III-weighted method (triangle points) and the parameterised approach (dot points), are reported

Chapter 7

Study and development of new system for lateral beam profiling measurements

Relative dosimetry, in terms of the measure and analysis of transversal beam distributions, represents a fundamental step in the quality control procedures for radiotherapy. In particular, for proton and ion beams, characterised by sharp dose gradients, detectors with an high spatial resolution result necessary for a correct beam characterisation. One of the goal of this thesis work has been also to improve the modality adopted for the characterization of the physical beam properties of the beamlines where irradiations and experiments have been performed (see Chapter 4 and Chapter 6). In this framework, a study focused on a characterization of a new beam profiler system detection has been performed. The new systems, based on the use of a scintillating detector coupled with a CCD (Charged Coupled Device) camera, has been characterized during two experimental campaigns:

- the spatial resolution, efficiency, reproducibility, energy dependence was investigated at CATANA INFN-LNS facility with 62 MeV of proton beam;

- a comparison to other well-know commercial systems commonly used for the same purpose (i.e. EBT3 films, Lynx and Timepix detector) was performed at the multidisciplinary experimental room of TIFPA-INFN.

The main advantages of such a device are the relative simplicity of assembly and the extreme velocity into the profile acquisition with a sufficient spatial resolution [34] [35]. A collaboration is actually ongoing between the LNS-INFN group and DDE.TEC.TOR. Srl (Turin, Italy) company for the placing on the market of this system. In this Chapter are described the main detector characteristics as well as the results obtained during the experimental test conducted at TIFPA-INFN facility.

7.1 The new developed beam profiling system

7.1.1 System assembly

The functioning principle of the developed Beam-Profiler (BP) system is based on the detection of the light emitted when a scintillator is hitted by proton or ion beam. It consists of a 50 x 50 mm^2 EJ-204 (Scionix, Bunnik, The Netherland) plastic scintillator screen, characterized by high scintillation efficiency, high speed and good attenuation length, positioned perpendicularly to the beam axis at a fixed distance; the light emitted when the scintillator is hit by the proton/ion beam is detected by a highly sensitive Peltier cooled (down to –10 °C) and low-noise 16-bit monochromatic charge-coupled device camera (Bigeye G-283 Cool Allied Vision Technologies GmbH, Germany) with a resolution of 1928 x 1452 pixels and processed by an in-house software. A 45° mirror, positioned behind the plastic scintillator sheet at a dis-

tance of 80 mm, reflects the light coming from the scintillator itself in the direction perpendicular to the beam axis, thus avoiding the direct irradiation of the CCD-chip. All the components of the beam profiling system are assembled in Teflon light-tight box (Figure 7.1).

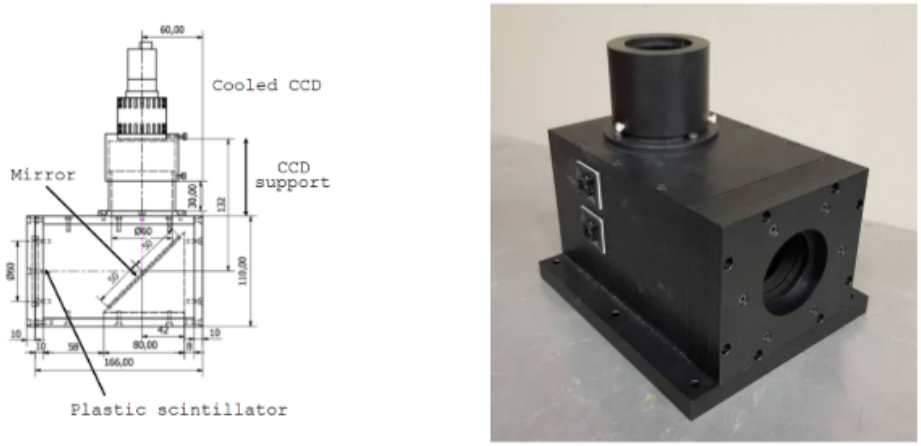

Figure 7.1: Schematic view of the beam profiling system (left) and picture of the external case of the prototype (right)

The CCD camera is fixed to the box by means of some adjustment screws that also permit its accurate alignment; it features an outstanding signal-to-noise ratio and a sensitivity of 73% at 530 nm, being the maximum quantum efficiency for wavelengths from 500 nm to 650 nm. An external-triggered acquisition is also possible, while a GigE Vision interface allows for its connection to the PC.

7.1.2 Acquisition and Processing Software

A dedicated software was developed on the LabView 2016 platform (National Instruments, Austin, TX, USA) for the real-time data acquisition and processing, while suitable MATLAB routines allow for the determination of the beam profile quality parameters along both horizontal and vertical directions. The signal is acquired and stored as a

16-bit matrix, with a dynamic range of 65536 Analog/Digital Units. In order to reduce the contribution due to the ambient light, a specific routine was implemented for the background removing by subtracting from the signal matrix the dark one obtained without any radiation. Each imaging matrix, in particular, was obtained as the arithmetical mean of a preliminarily defined number of consecutive frames, this averaging procedure producing a significant reduction of noise coupled with the scintillation signal. Two- and three-dimensional dose profile reconstruction can be also carried out through specifically developed routines. To avoid spikes affecting final results, which can arise from the interaction between the secondary ionizing radiation produced in the system components and the CCD-chip or from isolated broken pixel, a smoothing algorithm can also be applied, indiscriminately on the 1-D, 2-D or 3-D dose profile.

7.2 A preliminary characterization with high energy proton beam

7.2.1 Experimental Set-up

Experimental runs have been performed at the experimental research beamline of INFN-TIFPA where the cyclotron IBA Proteus 235 accelerates proton beam from 70 MeV to 228 MeV. The experimental setup is shown in Figure 7.2. Detectors adopted for the intercomparison were positioned at 125 cm from the beam exit point in air, corresponding with the Titanium window, also acting as the interface between vacuum and air.

The 100 MeV proton beam exits in air, traversing a 70 μm Titanium. It then interacts with a MiniQ-STRIP detector, a commercial device designed by DE.TEC.TOR. Srl (Turin, Italy) to monitor online the intensity, position and lateral profile of particle beams. The

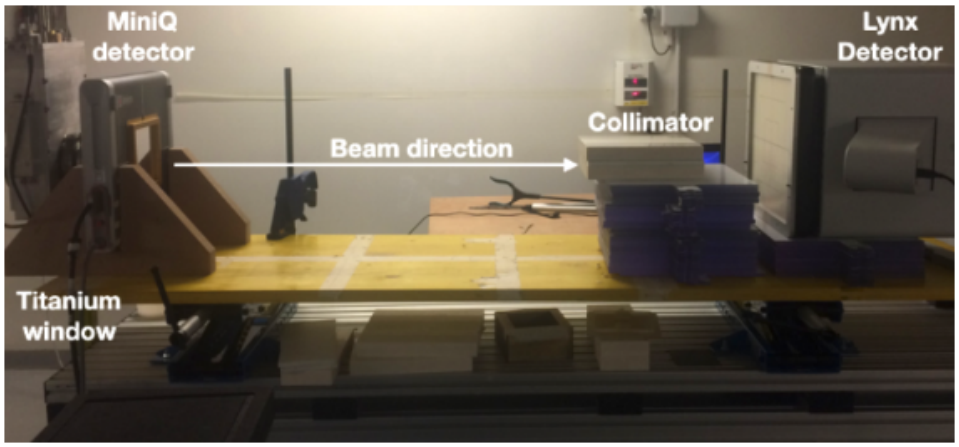

Figure 7.2: Picture of the experimental set-up at TIFPA beam line

information on these quantities comes from the passage of charged particles through a sequences of ionization chambers, each composed by two printed circuit boards. The beam is then intercepted by a PMMA (PolyMethylMethacrylate) collimator fixing the beam square spot with a side of 10 mm. All the detectors used in the intercomparison have been located just beyond the collimator, at the isocenter position, they are the BP developed by INFN-LNS, Lynx, Timepix and Gafchromic films. In the next section a detailed description of the last three devices.

Lynx

The Lynx detector is a 2D system, developed by IBA (Schwarzenbruck, Germany), for charged particles relative dosimetry. It consists of a scintillating screen of gadolinium-based plastic material (0.4 mm in thickness), coupled with a CCD camera in a compact light-tight box as shown in Figure 7.3. It has an active surface area of 30 x 30 cm^2 with an effective resolution of 0.5 mm [129]. When traversing the screen the incoming protons lose energy via ionization and this energy is then converted instantaneously into visible light, which is collected by the

photodiodes of a CCD camera after being reflected by a mirror. At the end of the process, the image of the proton spot is obtained, from which lateral profile and width can be analysed [130].

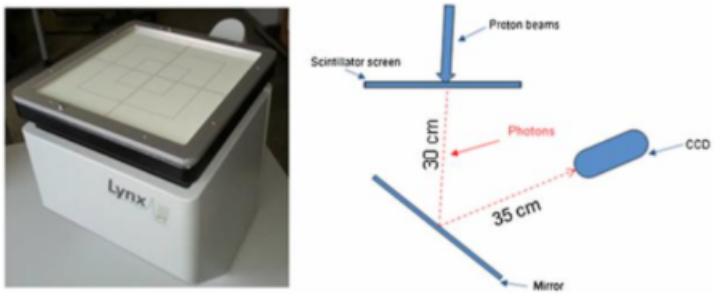

Figure 7.3: Photo of the Lynx detector and schematic view of the operating principle.

Timepix

Timepix is a silicon pixelated detector for ionizing radiation developed by the Medipix Collaboration [19]. This detector is able to measure simultaneously both the energy and position of the incoming particle. Specially, Timepix is made by a silicon sensor covered by a thin aluminium layer for bias application (usually 100V) and whose back is connected by bump bonding to an array of 256x256 individual read-out cells that together with the sensor define a pixel. The sensor is made up of a 300μm thick layer of high resistivity Si which covers an area of 1.5x1.5 cm^2 filled with 256x256 pixels of 55 μm sides each, as can be seen on Figure 7.4.

When a particle interacts with the sensor it creates a charge cloud that is driven by the bias towards the read-out cells where charges are collected.

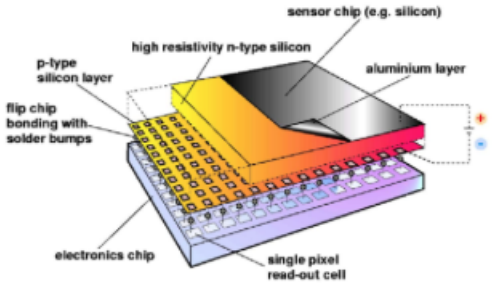

Figure 7.4: Timepix sensor scheme

Gafchromic EBT3 film

Gafchromic EBT3 is a passive detector generally used for the QA for clinical protons and ions beams. It shows a high spatial resolution (0.2 mm), near tissue equivalence, low energy dependence and is easy to handle. EBT3 film consists in three layers: a polyester substrate as a base coated with an active layer film which contains radiation-sensitive component. An over-laminate polyester is bonded to the active film. When the active component is exposed to radiation, it undergoes a polymerization reaction, forming a blue coloured area progressively darker in proportion to the absorbed dose. In order to appreciate only the effect of irradiation, the active layer contains a yellow marker dye which protects the film against ambient light exposure. EBT3 film can be read with a film scanner or digitizer. The best response is obtained if the film is scanned in transmission and the information is extracted from the red colour channel.

7.2.2 Monte Carlo simulations

In order to reproduce the experimental lateral dose profiling distribution, the entirely experimental set-up was simulated. The detector is modelled as a cube divided in slices 0.1x0.1x0.1 mm^3 in thickness. Dose

and fluence are scored during the simulation in each slice. The simulated primary proton beam had a Gaussian energy distribution, centred at the nominal energy of 147 MeV with a standard deviation of 1.1 MeV. The beam spot was circular and modelled as a bivariate Gaussian distribution having standard deviation of 1.805 mm and 2.835 mm along X and Y, respectively. Beam angular distribution was assumed Gaussian with a standard deviation of 0.0032 rad along X and 0.00364 along Y. A total of 10^7 protons were simulated. All calculations were carried out using the `Hadrontherapy` advanced example.

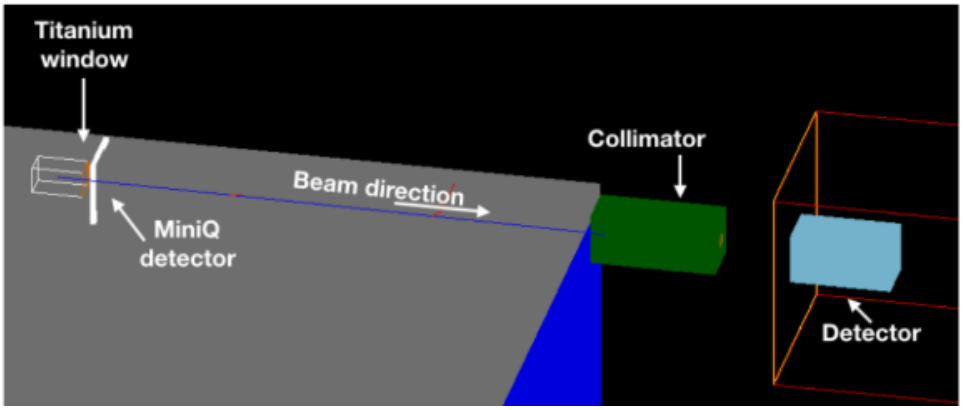

Figure 7.5: View of the simulated experimental setup

7.2.3 Results

The developed BP system has been preliminary characterized at CATANA facility with 62 MeV proton beam. The dosimetric characteristics were investigated in terms of short-term stability, linearity with the number of particles and spatial resolution. It showed an excellent short term stability with a coefficient of variation less than 0.5%. A remarkable linear behavior of the detector was observed, the scintillation signal increasing linearly with the dose rate within the experimental errors with a correlation fitting factor R2 $>$ 0.99.

Beam quality parameters measurements

As described in the previous section, the BP allows the on-line monitoring of transversal dose distribution of a proton/ion beam in order to perform a its fast and accurate characterization. The main parameters, extracted from the lateral dose profiles to provide an accurate and reliable evaluation of the beam features, are the following:

- **Radiation Field:** Full Width at Half Maximum of the profile. It allows to evaluate the effective beam size;
- **Field Ratio:** ratio of the profile widths at 90% and 50% of the maximum dose. It quantifies the difference between the experimental profile and an ideal rectangular step;
- **Lateral Penumbras (left and right):** lateral distance between the 80% and 20% of maximum dose points on both sides of the profile. It gives the value of right and left slopes of lateral dose falls;
- **Flatness:** maximum permissible percentage variation from the average dose across the central 80% of the FWHM of the profile in a plane transverse to the beam axis; according to, it is given by:

$$Flatness = (\frac{D_{max} - D_{min}}{D_{max} + D_{min}}) * 100 \tag{7.1}$$

- **Symmetry:** maximum acceptable percentage deviation of the "left-side" dose from the "right-side" dose of a beam profile often at 80% of the FWHM points;. Symmetry is given by:

$$Symmetry = (\frac{D(x)}{D(-x)}) * 100 \tag{7.2}$$

where D(x) and D(–x) are symmetrical points with respect to the beam axis.

7.2.4 Single spot characterization

The lateral profiles, measured for all the studied detectors,were extracted from the spot images and the FWHM was measured for both the horizontal and vertical profiles. The measured lateral dose profiles for 100 MeV are shown in Figure 7.6.

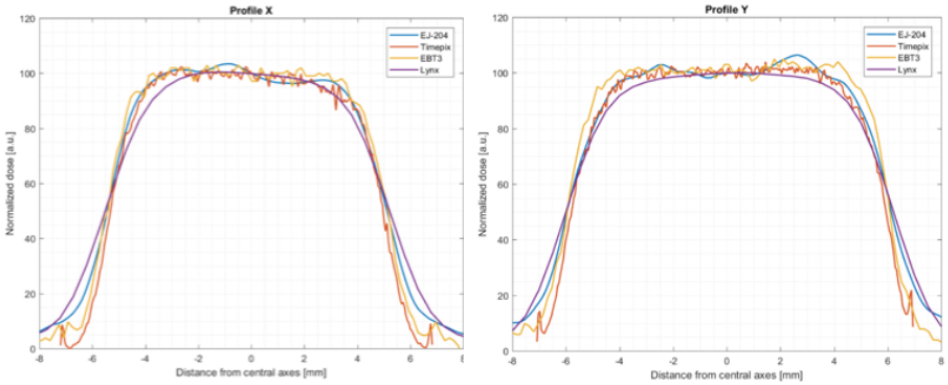

Figure 7.6: XX- XY profile of a monoenergetic proton beam of 100 MeV of energy.

The FWHM measured with the Lynx detector appear to be systematically larger than the one obtained with the other detectors; this is probably due to the higher Z of the material scintillator with respect the BP and a some algorithm based on smoothing process implemented inside the acquisition system. This originates a huge diffusing light resulting in a smearing and broadening of the beam lateral profile. The FWHM values measured with the Timepix detector are instead in agreement within 0.1% of discrepancy with the corresponding ETB3 films. The cross-check with the Timepix, the Lynx and EBT3 demonstrated the suitability of BP system for the online lateral dose distribution

characterization. In this case, the discrepancy with the EBT3 film is of the order of 0.6% as reported detail in Table 7.1.

However, the higher discrepancy as respect to the Timepix, is acceptable with the tolerance level for the FWHM stability protocol ($\pm$ 10% of the reference value). For a more accurate analysis, the spot profiles lateral penumbra (80%-20%) was evaluated (Table 7.1). The lower spatial resolution of the Lynx detector appears also evident from the comparison of the lateral penumbra as respect to the corresponding EBT3 film. A discrepancy of the order of 45% and 1% is recorder for the Lynx and the Timepix, respectively. The asymmetry has been also included and reported in Table 7.1. In general, the Timepix detector shown a better accuracy in the lateral dose profile detection but a less radiation hardness as respect to the BP. The tolerable fluence is the order of 10^6 p/cm^2 for the Timepix and 10^{10} p/cm^2 for BP detector. The Lynx commercial detector is easily-handled but the spatial resolution is less accurate from the point of view of spatial resolution. The EBT3 shown a good resolution (0.2 mm) but it's not a real time detector and more time-consuming for the analysis procedures. In conclusion, a detector monitoring of lateral beam profiling dose for protons and ions beam has been designed, tested and its performance compared with three commercial detectors. Experimental results proved that its accuracy is very close to the silicon pixelated detector (Timepix) and existing dosimetric devices (EBT3). An high resolution has shown as respect to the recently developed system for the relative dosimetry (Lynx). In Table 7.1 are illustrated just the informations about the profile extracted from the horizontal axis. A more extensive analysis as a function of the energy and of the incident particles fluence is actually ongoing .

Profile X	EBT3	Scintillator	Timepix	Lynx	Geant4
FWHM[mm]	10.460 ± 0.330	10.535 ± 0.100	10.450 ± 0.120	10.750 ± 0.500	10.460
90/50 Ratio[%]	0.793 ± 0.025	0.768 ± 0.010	0.765 ± 0.010	0.656 ± 0.074	0.782
Rigth penumbra[mm]	1.370± 0.340	1.400 ± 0.095	1.385± 0.105	2.350 ± 0.550	1.250
Left penumbra[mm]	1.220 ± 0.340	1.295 ± 0.090	1.260 ± 0.100	2.350 ± 0.550	1.360
Symmetry [%]	101.970± 1.530	103.003 ± 1.545	102.864 ± 1.543	101.343 ± 1.520	101.99

Table 7.1: Profile parameters calculated for each detector with 100 MeV of incident proton beam

Conclusions and future perspective

In the last years, protontherapy limitations become increasingly clear particularly in the case of radioresistant cancers, being protons radiobiologically almost as effective as photons. On the other side, although heavier particles, such as ^{12}C ions, could overcome radioresistance, they present radiobiological and economic issues that hamper their widespread adoption. In this context, an overall improvement in the quality of a protontherapy treatment couplet with an enhancement in their radiobiological efficacy is desirable. This thesis work has addressed both these issues.

A nuclear reaction triggered by the protons and able to generate short-range high-LET particles has been investigated to increase the protontherapy efficacy (Chapter 2). The new proposed strategy, called PBCT, is based on the nuclear fusion reaction $^{11}B(p,\alpha) \rightarrow 2\alpha$ able to generate high-LET α particles inside the cell nucleus. Promising results have been obtained irradiating DU145 prostate cancer cells with boron atoms injected. Moreover, a systematic study on PBCT based on prompt-gamma has lead to establish the limitations and potentialities of this technique. Establishing nuclear reaction-based binary approaches as a clinically viable strategy to increase proton radiobiological effectiveness would have a profound scientific and social impact, in addition to being an elegant example of bringing together apparently distant fields such

as nuclear physics and radiotherapy. Unfortunately, at the moment, it appears hard to justify in a rigorous way the observed effect. The newly approved INFN NEPTUNE project will try to study and understand the different physical, chemical and radiobiological aspects associated to the observed processes induced by charged particle beams, with the aim to fully understand the results and propose the pB as a possible future approach in the clinical practice.

In parallel, even if strictly connected with the first part, this thesis report an extensive work performed with the aim to improve the quality of a protontherapy treatment. This last was conducted inside the INFN MOVE-IT project and has been focused on the estimation of the main radiobiological quantities like LET and RBE (Chapter 5 and Chapter 6) as well as new passive elements developed to enhance the transport beam quality (Chapter 4) and new technique for its monitoring (Chapter 7).

A critical study on the current existing LET computation approaches with Monte Carlo has allowed to identify and implement new algorithms to estimate such quantity (Chapter 5). These will be officially released into the Hadrontherapy application in the next Geant4 release (10.05) in December 2018. The newly implemented algorithms able to reduce the actual dependence of calculated LET values from the transport parameters (30% for a change of secondaries production cut from 0.005 mm to 1 mm) to 2%. This makes this new approach suitable to be applied in microdosimetric calculations and permitted us to start a collaboration with the University of Wollongong to validate the code by a comparison with experimental data.

A wide study has been also performed on the strategies to estimate the biological damage. A new Monte Carlo method coupled to the LEM model has been proposed. In particular, it has been shown that a LEM-based and a parametrized approach coupled with Geant4 can ad-

equately reproduce experimentally derived survival curves from in-vitro cancer cell irradiations performed in a clinical proton beam. Unlike similar computational codes, the open-source nature of the employed MC code arguably represents a valuable asset that is much needed in the expanding field of cancer hadrontherapy. An interesting future application field will be certainly related with similar studies performed with high-LET incident particles that could be also interesting in the PBCT application. This preliminary work will be further extended with experimental data from other cancer cell lines irradiated at the CATANA beamline, in order to initiate a clinically relevant database and with the simulation. In this sense, a collaboration with several international institutes (GANIL, GSI, Vinca Institute and INFN) is already started. The last part of the work has been focused on a realization of a new Beam Profiler detector based on a plastic scintillator screen coupled to a high-resolution CCD camera. Its characterization with clinical proton beam as well as its comparison with such other detectors has lead to very promise results for its future application in clinical practice. A collaboration with the DE.TE.CTOR company for its placing on the market is already ongoing. In the next months is already planning to realize an upgrade of the system to clinical higher fields size (up to 20x20 cm^2).

Bibliography

[1] *GSI Helmholtzzentrum für Schwerionenforschung.* https://www.gsi.de/start/aktuelles.htm.

[2] *Official Geant4 website.* http://geant4.web.cern.ch.

[3] *Official IBA-dosimetry website.* https://www.iba-dosimetry.com.

[4] *Stopping Power and Ranges for Protons and Alpha Particles.* ICRU Report 49, 1993.

[5] *IAEA TRS 461 - Relative Biological Effectiveness in Ion Beam Therapy.* International Atomic Energy Agency, 2008.

[6] *Elemental Composition of the Human Body*, vol. MD Retrieved 17. Ed Uthman, 2017.

[7] Agostinelli, S., et al. Geant4 a simulation toolkit. *Nuclear Instruments and Methods in physics research Section A 506* (2003), 250–303.

[8] Akagi, T., et al. Ridge filter design for proton therapy at hyogo ion beam medical center. *Physics in Medicine and Biology 301* (2003), 48:22.

[9] Allen, B., Raja, C., Rizvi, S., Li, Y., Tsui, W., Zhang, D., and Thompson, J. Targeted alpha therapy for cancer. *Physics in Medicine and Biology* (2004), 3703–13.

[10] Allen, B., Raja, C., Rizvi, S., Song, E., and Graham, P. Tumour anti-vascular alpha therapy: a mechanism for the regression of solid tumours in metastatic cancer. *Physics in Medicine and Biology 52(13)* (2007), 15–9.

[11] Allison, J., et al. An application of the geant3 geometry package to the description of the opal detector. *Computer Physics Communications CERN-EP/87-80* (1987).

[12] Allison, J., et al. Geant4 developments and applications. *IEEE Transaction on Nuclear Science 53(1)* (2006), 270–8.

[13] Amadio, G., et al. The geantv project: preparing the future of simulation. *Journal of Physics - Conference Series 664* (2015).

[14] Apostolakis, J., et al. Progress in hadronic physics modelling in geant4. *Journal of Physics - Conference Series 160*, 012073 (2009).

[15] Aron, A., et al. Recognition- and reactivity-based fluorescent probes for studying transition metal signaling in living systems. *Accounts of chemical research 48* (2015), 2434:2442.

[16] Ballarini, F., et al. Chromosome aberration as biomarkers of radiation. *Radiation Protection and dosimetry 25* (2003).

[17] Becker, H., et al. Low-energy cross sections for 11b(p, 3a)*. *Zeitschrift für physik a hadrons and nuclei 327* (1987), 341–355.

[18] Bethe, H. Zur theorie des durchgangs shneller korpuskularstrahlen durch materie. *Annual Physics 5* (1930), 325.

[19] Biegun, A. Proton radiography with timepix based time projection chamber. *IEEE Transaction on Nuclear Science 35(4)* (2016), 1099–105.

[20] BijianJia, S., et al. Designing a range modulator wheel to spread-out the bragg peak for a passive proton therapy facility. *Nuclear Instruments and Methods in physics research Section A 806* (2015), 101–108.

[21] Bloch, F. Zur bremsung rasch bewegter teilchen beim drchgang durch die materie. *Annual Physics 16* (1933), 285.

[22] Bourhaleb, F., et al. Monte carlo simulations of ripple filters designed for proton and carbon ion beams in hadrontherapy with active scanning technique. *Journal of Physics - Conference Series 102(1)* (2008).

[23] Brun, R., Hansroul, M., and Lassalle, J. C. Geant user's guide. *CERN Report DD/EE/82* (1982).

[24] Caccia, B., et al. Medlinac2: a geant4 based software package for radiotherapy. *Annual Technical Report of Istituto Superiore di Sanità 46(2)* (2010).

[25] Carante, M., and Ballarini, F. Calculating variations in biological effectiveness for a 62 mev proton beam. *Frontiers in Oncology 6* (2016).

[26] Catalano, R., Petringa, G., et al. Scintillator-based system for transversal dose profile recostruction. *Nuclear Instruments and Methods in physics research Section A - submitted* (2018).

[27] Chadwick, K., and Leenhouts, H. A molecular theory of cell survival. *Physics in Medicine and Biology 13* (1973), 78–87.

[28] Chan, A., and Liebsch, N. Proton radiation therapy for head and neck cancer. *Journal of Surgery Oncology 97* (2008), 697–700.

[29] Charlton, D., and Allen, B. Dose sparing of capillary endothelial cells for bsh and bpa: a model for capillary truncation. *proceedings of the Sixth International Symposium on Neutron Capture Therapy for Cancer* (1996).

[30] Chaudary, P., et al. Relative biological effectiveness variation along monoenergetic and modulated bragg peaks of a 62-mev therapeutic proton beam: A preclinical assessment. *International Journal Radiation Oncology Biology Physics 90(1)* (2014), 27–35.

[31] Chen, A., Liu, Y., and Sheu, R. Radiation shielding evaluation of the bnct treatment room at thor: A tort- coupled mcnp monte carlo simulation study. *Applied Radiation and Isotopes 66*, 28–38 (2008).

[32] Chiari, M., et al. Proton elastic scattering cross-section on boron from 0.5 to 3.3 mev. *Nuclear Instruments and Methods in physics research Section B* (2001), 309:318.

[33] Chu, W., Ludewigt, B., and Renner, T. Instrumentetion for treatment of cancer using proton and light ions. *Review Scientific Instruments 64* (1993), 2055–2122.

[34] Cirrone, G., et al. Deep characterization of a fast monitoring system for radiotherapeutic proton beams based on scintillating screens and a ccd camera. *IEEE Transaction on Nuclear Science 51* (2004), 1752–1756.

[35] Cirrone, G., et al. A fast monitoring system for radiotherapeutic proton beams based on scintillating screens and a ccd camera. *IEEE Transaction on Nuclear Science 51* (2004), 1584–1587.

[36] Cirrone, G., et al. Implementation of a new monte carlo geant4 simulation tool for the development of a proton therapy beam line and verification of the related dose distributions. *IEEE Transaction on Nuclear Science 52*, 1756:58 (2005).

[37] Cirrone, G., et al. Hadrontherapy: A 4-based tool for proton/ion-therapy studies. *Progress in Nuclear Science Technology 2* (2011), 207–212.

[38] Cirrone, G., et al. Clinical and research activities at the catana facility of infn-lns: From the conventional hadrontherapy to the laser-driven approach. *Frontiers in Oncology* (2017).

[39] Cirrone, G., et al. First experimental proof of proton boron capture therapy (pbct) to enhance protontherapy effectiveness. *Scientific Reports 8(1)*, 1141 (2018).

[40] Coates, A., et al. On the receiving end—patient perception of the side-effects of cancer chemotherapy. *European Journal of Nuclear Medicine and Molecular Imaging 19(2)* (1983), 203–8.

[41] Comte de Buffon, G. Essai d'arithmétique morale. *Supplément à l'Histoire Naturelle 4* (1777).

[42] Cotes-Giraldo, M., et al. A critical study of different monte carlo scoring methods of dose average linear-energy-transfer maps calculated in voxelized geometries irradiated with clinical proton beams. *Physics in Medicine and Biology 60* (2015), 2645–69.

[43] Couturier, O., et al. Cancer radioimmunotherapy with alpha-emitting nuclides. *European Journal of Nuclear Medicine and Molecular Imaging 32(5)*, 601-14 (2005).

[44] Cuttone, G., et al. Catana protontherapy facility: The state of art of clinical and dosimetric experience. *The European Physical Journal Plus 126*, 65 (2011).

[45] Darby, S., Ewertz, M., et al. Risk of ischemic heart disease in women after radiotherapy for breast cancer. *The New England Journal of Medicine 368(11)* (2013), 987–98.

[46] Durante, M., and Loeffler, J. Charged particles in radiation oncology. *Nature Reviews in Clinical Oncology 7* (2010), 37–43.

[47] Elles, S. Geant4 and fano cavity test: where are we? *Journal of Physics: Conference Series 102* (2008).

[48] Elsasser, T., et al. Accuracy of the local effect model for the prediction of biologic effects of carbon ion beams in vitro and in vivo. *International Journal Radiation Oncology Biology Physics 71* (2008), 866–72.

[49] Fertil, B., Reydellet, I., and Deschavanne, P. A benchmark of cell survival models using survival curves for human cells after completion of repair of potentially lethal damage. *Radiation Research 138* (1994), 61–69.

[50] Giuffrida, L., et al. Prompt gamma ray diagnostics and enhanced hadron-therapy using neutron-free nuclear reactions. *AIP Advances 6* (2016), 105:204.

[51] Givehchi, N., et al. Online monitor detector for the proton-therapy beam at the infn laboratori nazionali del sud-catania. *Nuclear Instruments and Methods in physics research Section A 572(3)* (2006), 1094–1101.

[52] Gray, L. The distribution of ions resulting from the irradiation of living cells. *British Journal of Radiology 1* (1947), 7–15.

[53] Grussel, E., et al. A general solution to charged particle beam flattening using an optimized dual scattering foil technique with application to proton therapy beams. *Physics in Medicine and Biology 50(5)* (2005), 755–67.

[54] Guan, F., et al. Analysis of the track- and dose-averaged let and let spectra in proton therapy using the geant4 monte carlo code. *Medical Physics 42 (11)* (2015).

[55] Guatelli, S., et al. Review of geant4-dna applications for micro and nanoscale simulations. *Physica Medica 32(10)*, 1187-1200 (2016).

[56] Haume, K. Gold nanoparticles for cancer radiotherapy: a review. *Cancer Nanotechonology 7(1)*, 8 (2016).

[57] Hawkins, R. B. A microdosimetric-kinetic model of cell death from exposure to ionizing radiation of any let, with experimental and clinical applications. *International Journal Radiation Biology 69(6)* (2017), 739–755.

[58] Hewitt, H. Rationalizing radiotherapy: some historical aspects of the endeavour. *British Journal of Radiology 550* (1973), 917–926.

[59] Hollmark, M., Uhrdin, J., Belkic, D., et al. Influence of multiple scattering and energy loss straggling on the absorber dose distributions of therapeutic light ion beams: I. analytica pencil beam model. *Physics in Medicine and Biology 49* (2004), 3247–3265.

[60] Howard, M., et al. Investigating dependencies of relative biological effectiveness for proton therapy in cancer cells. *International Journal of Particle Therapy 4(3)* (2018), 12–22.

[61] http://www.ptcog.ch. *Particle Therapy Co-Operative Group.* Particle Therapy Centers, 2018.

[62] Hutcheson, A. *Neutron-Induced Partial Gamma-Rays Cross-Section Measurements of Uranio.* Department of Physics, Duke University, 2008.

[63] Hyvone-Dabek, M. Proton-induced prompt gamma ray emission for determination of light elements in human bone. *Journal of Radioanalytical Chemistry 63* (1981), 367:378.

[64] Incerti, S., et al. Monte carlo dosimetry for targeted irradiation of individual cells using a microbeam facility. *Radiation and Proton Dosimety 133(1)* (2009), 2–11.

[65] Incerti, S., et al. Comparison of geant4 very low energy cross section models with experimental data in water. *Medical Physics 37(9)* (2010), 4692–708.

[66] Incerti, S., et al. The geant4-dna project. *Internatiinal Journal of Modeling, Simulation and Scientific Computing*, 157–178 (2010).

[67] Jan, S., et al. Gate - geant4 application for tomographic emission: a simulation toolkit for pet and spect. *Physics in Medicine and Biology 49(19)* (2004), 4543–4561.

[68] Jones, B., Krishnan, S., and Cho, S. Estimation of microscopic dose enhancement factor around gold nanoparticles by monte carlo calculations. *Medical Physics 37*, 3809–3816 (2010).

[69] Kase, Y., et al. Biophysical calculation of cell survival probabilities using amorphous trackstructure models for heavy-ion irradiation. *Physics in Medicine and Biology 53* (2008), 37–59.

[70] Kellerer, A., and Chmelevsky, D. Criteria for the applicability of let. *Radiation Research 63* (1975), 226–234.

[71] Kellerer, A., Kase, K., Bjarngard, B., and Attix, F. *Fundamentals of microdosimetry. In Dosimetry of Ionizing Radiatio*, vol. I. Academic Press, Orlando, 1985.

[72] Kellerer, A., and Rossi, H. A generalized formulation of dual radiation action. *Radiation Research 75* (1978).

[73] Kempe, J., et al. Depth absorbed dose and let distributions of therapeutic 1h, 4he, 7 li and 12c beams. *Medical Physics 34*, 183-92 (2007).

[74] Kevitaa, N., et al. Boron neutron capture therapy: a literature review. *Journal Clinical and Diagnostic Research 10(12)* (2016).

[75] Kiefer, J. The physical basis for the biological action of heavy ion. *New Journal of Physics 10* (2008).

[76] Kimura, A., et al. Dicom interface and visualization tool for geant4-based dose calculation. *IEEE Transaction on Nuclear Science* (2005).

[77] Kjellberg, R. N., Hanamura, T., Davis, K., Lyons, S., and Adams, R. Bragg peak proton-beam therapy for arteriovenous malformations of the brain. *National England Journal of Medicine* (1983), 269–274.

[78] Kobayashi, T., et al. Microanalysis system of ppm-order ^{10}b concentrantions in tissue for neutron capture therapy by prompt gamma-ray spectrometry. *Nuclear Instruments and Methods in physics research Section A* (1983), 525:531.

[79] Koehlerm, A., and Preston, W. Protons in radiation therapy. *Radiology 104* (1972), 191–195.

[80] Koning, A., et al. Modern nuclear data evaluation with the talys code system. *Nuclear Data Sheets 113* (2012).

[81] Kraft, G. The radiobiological and physical basis of radiotherapy with protons and heavier ions. *Strahlenther Onkol 166* (1990), 10–13.

[82] Kraft, G., et al. Cellular and subcellular effect of heavy ions: a comparison of the induction of strand breaks and chromosomal aberration with the incidence of inactivation and mutation. *Advanced Space Research 9* (1989), 59–72.

[83] Kraft, G., Kramer, M., and Scholtz, M. Let, track structure and models. *Radiation and Environmental Biophysics 31* (1992), 161–180.

[84] Kramer, M., et al. Treatment planning for heavy-ion radiotherapy: physical beam model and dose optimization. *Physics in Medicine and Biology 45* (2000), 3299–17.

[85] Kramer, M., et al. Overview of recent advances in treatment planning for ion beam radiotherapy. *European Physics Journal 68*, 306 (2014).

[86] Kramer, M., and Scholz, M. Treatment planning for heavy-ion radiotherapy: calculation and optimization of biologically effective dose. *Physics in Medicine and Biology 45*, 3319-30 (2000).

[87] Kurosawa, S., et al. Prompt gamma detection for range verification in proton therapy. *Current Applied Physics 12* (2012), 364:368.

[88] Kyriakou, I., et al. Improvements in geant4 energy-loss model and effect on low-energy electron transport in liquid water. *Medical Physics 42* (2015), 3870–3876.

[89] Larsson, B., et al. Effect of high energy protons on the spinal cord. *Acta Radiology 51* (1959), 52–64.

[90] Lawrence, J. Proton irradiation of the pituitary. *Cancer 10* (1957), 795–798.

[91] Linz, U. *Ion beam therapy. Fundamentals, Technology, Clinical applications.* Springer, 2011.

[92] Liu, J., et al. Cross-sections of 11b(p,a)8be reaction for boron analysis. *Nuclear Instruments and Methods in physics research Section A 190* (2002), 107:111.

[93] Lodge, M., et al. A systematic literature review of the clinical and cost-effectiveness of hadrontherapy in cancer. *Radiotherapy and Oncology 83* (2007), 110–122.

[94] Mairani, A., et al. The fluka monte carlo code coupled with the local effect model for biological calculations in carbon ion therapy. *Physics in Medicine and Biology 55* (2010), 4273.4289.

[95] Manganaro, L., Russo, G., et al. Survival: a simulation toolkit introducing a modular approach for radiobiological evaluations in ion beam therapy. *Physics in Medicine and Biology 63(8)* (2018), 08–01.

[96] Manti, L., et al. Measurements of metaphase and interphase chromosome aberrations transmitted through early cell replication rounds in human lymphocytes exposed to low-let protons and high-let 12c ions. *Mutation Research 596* (2006), 151–165.

[97] Masunaga, et al. The dependency of compound biological effectiveness factors on the type and the concentration of administered neutron capture agents in boron neutron capture therapy. *Springer Plus 3*, 128 (2014).

[98] Mayu, I., Yukari, Y., et al. Carbon-ion beams effectively induce growth inhibition and apoptosis in human neural stem cells compared with glioblastoma a172 cells. *Journal of Radiation Research 56(5)* (2015), 856–61.

[99] McNamara, A. L., et al. A phenomenological relative biological effectiveness (rbe) model for proton therapy based on all published in vitro cell survival data. *Physics in Medicine and Biology 60(21)* (2015), 8399–8416.

[100] Metropolis, N. The beginning of the monte carlo method. *Los Alamos Science (Secial Issue)* (1987).

[101] Metropolis, N., and Ulam, S. Monte carlo method. *American Statistical Association* (1949).

[102] Metting, N., et al. Microdosimetry near the rajectory of high-energy heavy ions. *Radiation Research 116* (1988).

[103] Meyer, H. Symposium on monte carlo methods.

[104] Nahum, A. Condensed history monte carlo simulation for charged particles: what can it do for us? *Radiation and Environmental Biophysics 38(3)* (1999).

[105] Okada, S., et al. Gpu acceleration of monte carlo simulation at the cellular and dna levels. *Smart Innovation, Systems and Technologies* (2015), 323–332.

[106] Paganetti, H. *Proton therapy Physics*. Series in Medical Physics and Biomedical Engineering, 2012.

[107] Paganetti, H. Relative biological effectiveness (rbe) values for proton beam therapy. variations as a function of biological endpoint, dose, and linear energy transfer. *Physics in Medicine and Biology 59* (2014).

[108] Paganetti, H., Niemierko, A., et al. Relative biological effectiveness (rbe) values for proton beam therapy. *International Journal Radiation Oncology Biology Physics 53* (2002), 407–421.

[109] Pandola, L., et al. Validation of the geant4 simulation of bremsstrahlung from think targets below 3 mev. *Nuclear Instruments and Methods in physics research Section A*, 350 (2015), 41–48.

[110] Petringa, G. Study of gamma-ray emission by proton beam interaction with injected boron atoms for future medical imaging applications - oral presentation. In *IPRD16 (Siena, Italy)* (2016).

[111] Petringa, G. Hadrontherapy: an official advanced example of geant4 toolkit - oral presentation. In *103 Congresso Nazionale della SIF (Trento, Italy)* (2017).

[112] Petringa, G. The proton-boron fusion therapy: a new clinical treatment and a powerful online imaging techniques - oral presentation. In *RAD17 (Budva, Montenegro)* (2017).

[113] Petringa, G. Dosimetry and monte carlo related to the first experiment on pbct - invited talk. In *Towards Proton Boron Capture Therapy (Trento, Italy)* (2018).

[114] Petringa, G. Hadrontherapy: status, recent updates and new developments. In *23rd Geant4 Collaboration Meeting (Lund, Sweden) - Oral Presentation* (2018).

[115] Petringa, G. New methods for the linear energy transfer (let) and relative biological effectiveness (rbe) calculation by using geant4 monte carlo code. In *Third Geant4 International User Conference (Bordeaux, France) - Oral Presentation* (2018).

[116] Petringa, G. The proton boron capture therapy: a new protontherapy enanched techinque - oral presentation. In *ERR18 (Pecs, Hungary)* (2018).

[117] Petringa, G. Relative biological effectiveness (rbe) of a clinical eye proton therapy beam: experiments and monte carlo approach. In *Third Geant4 International User Conference (Bordeaux, France) - Oral Presentation* (2018).

[118] Petringa, G., et al. Development and analysis of the tracklet, dose-let and rbe calculations with a therapeutical proton and ion beams using geant4 monte carlo toolkit. *Physica Medica 42(1)* (2017), 9.

[119] Petringa, G., et al. Prompt gamma-ray emission for future imaging applications in proton-boron fusion therapy, journal of instrumentation. *Journal of Instrumentation C03059* (2017).

[120] Petringa, G., et al. Study of gamma-ray emission by proton beam interaction with injected boron atoms for future medical imaging applications. *Journal of Instrumentation 12(03)* (2017).

[121] Petringa, G., et al. Different approaches for track and absorbed-dose average let calculation for p, he, li, be, b, c, n and o beams using the open-source hadrontherapy geant4 application. *Physica Medica submitted* (2018).

[122] Petringa, G., et al. Proton boron fusion reaction increases proton radiobiology effectiveness - oral presentation. In *Particle Therapy Co-Operative Group 57 (Cincinnati, Ohio)* (2018).

[123] Petringa, G., et al. Radiobiological quantities in proton-therapy: estimation and validation using geant4-based monte carlo simulations. *Physica Medica submitted* (2018).

[124] Pinto, M., et al. Assessment of geant4 prompt-gamma emission yields in the context of proton therapy monitoring. *Frontiers in Oncology* (2016), 364–368.

[125] Polf, J., et al. Measurement and calculation of characteristic prompt gamma ray spectra emitted during proton irradiation. *Physics in Medicine and Biology* (2009).

[126] Pshenichnov, I., et al. Comparatice study of depth-dose distributions for beams of light and heavy nuclei in tissue-like media. *Nuclear Instruments and Methods in physics research Section B 266* (2008), 1094–8.

[127] Roentgen, W. On a new kind of rays. *Nature 53* (1896), 274–276.

[128] Rontgen, W. Uber eine neune art von strahlen. *Vorlaufige Mitteilung. In: Sitzungsberichte der physikalisch-medicineschen 30* (1895), 132–141.

[129] Russo, S., et al. Dosimetric characterization of a commercial 2-d scintillation detector for quality assurance tests in scanned proton and carbon ion beams. *Physica Medica* (2016).

[130] Russo, S., et al. "characterization of a commercial scintillation detector for 2-d dosimetry in scanned proton and carbon ion beams. *Physica Medica 34* (2017), 48–54.

[131] Schulz-Ertner, D., and Tsuji, H. Particle radiation therapy using proton and heavier ion beams. *Journal of clinical oncology 25* (2007), 953–964.

[132] Seco, J., and Verhaegen, F. Monte carlo techniques in radiation therapy. *Series: Imaging in Medical Diagnosis and Therapy* (2016).

[133] Segrè, E. *Nuclei and Particles.* New Yotk, Benjamin, 1964.

[134] Shin, H., et al. Prompt gamma ray imaging for verification of proton boron fusion therapy: A monte carlo study. *Physica Medica 32* (2016).

[135] Sholz, M. Track structure and the calculation of biological effects of heavy charged particles. *Advanced Space Research 18* (1996), 5–14.

[136] Sholz, M., et al. Computation of cell survival in heavy ion beams for therapy. the model and its approximation. *Radiation and Environmental Biophysics 36* (1997), 59–66.

[137] Smeets, J., et al. Prompt gamma imaging with a slit camera for real-time range control in proton therapy. *Physics in Medicine and Biology 57* (2012), 3371–3405.

[138] Sokol, O., et al. Towards the multi-ion treatment planning with 16o beams. *GSI Scientific Report* (2016).

[139] Spraker, M., et al. The ^{11}b(p,α)^{8}be $\alpha + \alpha$ and the ^{11}b(α,α)^{11} b reactions at energies below 5.4 mev. *Journal of Fusion energy 31* (2012), 357:367.

[140] Suit, H., Goitein, M., et al. Exploratory study of proton radiation therapy using large field techniques and fractionated dose schedules. *Cancer* (1975), 1647–1657.

[141] Takada, Y. Dual-ring double scattering method for proton beam spreading. *Journal of Applied Physics 33* (1994), 353–359.

[142] Tobias, C., Anger, H., and Lawrence, J. Radiological use of high energy deuterons and alpha particles. *The american journal of roentgenol radium therapy and nuclear medicine 67* (1952), 1–27.

[143] Tommasino, F., and Durante, M. Proton radiobiology. *Cancer 12* (2015), 7353–7381.

[144] Tommasino, F., et al. New ions for therapy. *International Journal of Particle Therapy* (2016).

[145] Tommasino, F., et al. Proton beam characterization in the experimental room of the trento proton therapy facility. *Nuclear Instruments and Methods in physics research Section A*, 869 (2017), 15–20.

[146] Tommasino, F., et al. A new facility for proton radiobiology at the trento proton therapy centre: design and implementation. *Submitted on Nuclear Instruments and Methods in physics research Section A* (2018).

[147] Trivillin, V. A., et al. Biodistribution of the boron carriers boron ophenylalanine (bpa) and/or decahydrodecaborate (gb-10) for boron neutron capture therapy (bnct) in an experimental model of lung metastases. *Applied Radiationand Isotopes 88* (2014), 94:98.

[148] Varma, M., et al. Radial dose, let and w for 16o ions in n2 and tissue equivalent gases. *Radiation Research 70* (1977), 511–518.

[149] Verburg, J. M., et al. Simulation of prompt gamma-ray emission during proton radiotherapy. *Physics in Medicine and Biology 57* (2012), 5459:5472.

[150] Vuosalo, C., et al. A tool to convert cad models for importation into geant4. *arXiv:170.04427* (2017).

[151] Weber, U., Becher, W., and Kraft, G. Depth scanning for a conformal ion beam treatment of deep seated tumours. *Physics in Medicine and Biology 45* (2000), 3627–3641.

[152] Wilkens, J., and Oelfke, U. Analytical linear energy transfer calculation for protontherapy. *Medical Physics 30*, 806 (2002).

[153] Wilson, R. Radiobiological use of fast protons. *Radiology 104* (1946), 487–491.

[154] Wilson, R. Monte carlo study of shower production. *Physical Review*, 261–269 (1952).

[155] Wright, H., and Kelsey, M. The geant4 bertini cascade. *Nuclear Instruments and Methods in physics research Section A 804* (2015), 175–188.

[156] Wulff, J. Topas/geant4 configuration for ionization chamber calculations in proton beams. *Physics in Medicine and Biology* (2018), 106989.

[157] Xuan, S., et al. Synthesis and in vitro studies of a series of carborane-containing boron dipyrromethenes (bodipys). *Journal of Medicine and Chemistry 59* (2016), 2109–2117.

[158] Yoon, D. K., et al. Application of proton-boron fusion reaction to radiation therapy: a monte carlo simulation study. *Applied Physics Letter 105* (2014).

[159] Zirkle, R. *The radiobiological importance of Linear Energy Transfert*, vol. 1. Radiation Biology, 1954.